Wind Turbine Generator Condition Monitoring via the Generator Control Loop

Mahmoud Nouh Zaggout

A thesis presented for the degree of

Doctor of Philosophy

School of Engineering and Computing Sciences

University of Durham

UK

2013

Dedicated to

my mother, my loving wife Amna and my wonderful children Abdulaziz and Areen.

Wind Turbine Generator Condition Monitoring via the Generator Control Loop

Mahmoud Nouh Zaggout

Submitted for the degree of Doctor of Philosophy

2013

Abstract

This thesis focuses on the development of condition monitoring techniques for application in wind turbines, particularly for offshore wind turbine driven doubly fed induction generators. The work describes the significant development of a physical condition monitoring Test Rig and its MATLAB Simulink model to represent modern variable speed wind turbine and the innovation and application of the rotor side control signals for the generator fault detection.

Work has been carried out to develop a physical condition monitoring Test Rig from open loop control, with a wound rotor induction generator, into closed loop control with a doubly fed induction generator. This included designing and building the rotor side converter, installing the back-to-back converter and other new instrumentation. Moreover, the MATLAB Simulink model of the Test Rig has been developed to represent the closed loop control, with more detailed information on the Rig components and instrumentation and has been validated against the physical system in the time and frequency domains.

A fault detection technique has been proposed by the author based on frequency analysis of the rotor-side control signals, namely; *d*-rotor current error, *q*-rotor current error and *q*-rotor current, for wind turbine generator fault detection. This technique has been investigated for rotor electrical asymmetry on the physical Test Rig and its MATLAB Simulink model at different fixed and variable speed conditions. The sensitivity of the each proposed signal has been studied under different operating conditions. Measured and simulated results are presented, a comparison with the results from using stator current and total power has been addressed and the improvement in condition monitoring detection performance has been demonstrated in comparison with previous methods, looking at current, power and vibration analysis.

Declaration

The work in this thesis is based on research carried out within the New and Renewable Energy Group, School of Engineering and Computing Sciences, University of Durham, United Kingdom. No part of this thesis has been submitted elsewhere for any other degree or qualification and it all my own work unless referenced to the contrary in the text.

Acknowledgments

I would like to express my sincere gratitude to my supervisors Prof. Peter Tavner and Dr. Christopher Crabtree for the continuous support and assistance of my PhD study, for their patience, motivation, enthusiasm, and immense knowledge. Their guidance helped me in all the time of research and writing of this thesis. I could not have imagined having a better supervisors and mentor for my PhD study.

Besides my supervisors, I would like to thank Prof. Li Ran for his assistance in designing and building the RSI controller in the physical Test Rig and its MATLAB model and sorting out the PLECS license problem.

My sincere thanks also go to David Jones, Paul Jarvis, Ian Garrett, Ian Hutchinson and Colin Wintrip and all the technicians in the mechanical and electronic workshops who helped me in developing the physical Test Rig.

Also I thank my colleagues at University of Durham: Terry Ho and Peter Wyllie for their assistance in developing the physical Test Rig and closing the generator control loop.

Thanks must also be extended to the Libyan government who funded and supported this work.

Last but not the least; I would like to thank my family: my parents for giving birth to me at the first place and supporting me spiritually throughout my life, my wife Amna Alberegli for always being there when I needed her.

List of Publications

1. M. N. Zaggout, P. J. Tavner and L. Ran, ”Wind Turbine Condition Monitoring Using Generator Control Loop,” IET International Power Electrical Machines & Drives Conference, Bristol, UK, 2012.
2. M. N. Zaggout, P. J. Tavner and L. Ran, ”Wind Turbine Doubly Fed Induction Generator Fault Detection Based on Control Loop Signals,” Scientific Track, European Wind Energy Association Conference, EWEA2012, Copenhagen, Denmark, 2012.
3. M. N. Zaggout, P. J. Tavner, C. Crabtree and L. Ran, ”Wind Turbine Doubly Fed Induction Generator Rotor Electrical Asymmetry Detection,” IET Renewable Power Generation, Awaiting peer review, 2013.

List of Contents

List of Figures

List of Tables

Abbreviations

A	Availability
AEP	Annual energy production
ARWS	Above rated wind speed
BRWS	Below rated wind speed
CBM	Condition-based maintenance
CCC	Committee on Climate Change
CM	Condition monitoring
CMS	Condition monitoring system
CoE	Cost of Energy
CSP	Concentrating solar power
DAQ	Data acquisition
DFIG	Doubly fed induction generator
DFT	Discrete Fourier transform
DTC	Direct Torque Control
EWEA	European Wind Energy Association
FCR	Fixed charge rate
FFT	Fast Fourier Transform
FOC	Field oriented control
GECOL	General Electrical Company of Libya
GS	Gating signal
GSI	Grid side inverter
ICC	Initial capital cost
IG	Induction generator
IGBT	Insulated-gate bipolar transistors
IM	Induction motor
LPF	Low pass filter
LRC	levelized replacement cost
MCSA	Motor current signature analysis
MMI	Man machine interface
MTBF	Mean Time between Failures
MTTF	Mean Time to Failures

MTTR	Mean Time To Repair
NAREC	National Renewable Energy Centre
NRGAP	National Renewable Energy Action Plan
O&M	operation and maintenance
OEM	Original equipment manufacturer
PM	Preventive or scheduled maintenance
PMSG	Permanent magnet synchronous generator
PSD	Power spectral density
PV	Photovoltaic
PWM	Pulse width modulation
REAOL	Renewable Energy Authority of Libya
RSI	Rotor side inverter
SCADA	Supervisory control alarm and data acquisition
SCIG	Squirrel cage induction generator
SCIM	Squirrel cage induction motor
SFOVC	Stator Flux-Oriented Vector Control
SHM	Structural Health Monitoring
SWH	Solar water heater
WECS	Wind energy conversion systems
WEI	Wind energy index
WRIG	Wound rotor induction generator
WT	Wind turbine

Nomenclature

b_1	Backlash in 1st pair gears
b_2	Backlash in 2nd pair gears
C_p	Wind turbine power coefficient
D_{g1}	Damping constant of 1st pair gears
D_{g2}	Damping constant of 2nd pair gears
D_{hs}	High speed shaft damping constant
D_{ls}	Low speed shaft damping constant
f	Frequency or stator frequency
f_{tri}	PWM carrier frequency
I_{dr}	Harmonic magnitude of d-rotor current
I_{qr}	Harmonic magnitude of q-rotor current
i_a	Actual DC motor armature current
$i_{a\,ref}$	Reference DC motor armature current
i_{dr}	d-component of rotor current
$i_{dr\,ref}$	d-rotor reference current
i_{ds}	d-component of stator current
i_f	DC motor field current
i_m	Total magnetizing current
i_{sm}	Stator magnetizing current
i_{qr}	q-component of rotor current
$i_{qr\,ref}$	q-rotor reference current
i_{qs}	q-component of stator current
$i_{\alpha s}$	α-component of stator current
$i_{\beta s}$	β-component of stator current
J_{DC}	Moment of inertia of DC motor
J_{DCm}	Moment of inertia of DC motor and mass plate
J_g	Moment of inertia of generator
J_{gm}	Moment of inertia of generator and mass plate
J_{g1}	Moment of inertia of 1st gear
J_{g2}	Moment of inertia of 2nd gear

J_{p1}	Moment of inertia of 1st pinion
J_{p2}	Moment of inertia of 2nd pinion
j	$\sqrt{-1}$
K_{fDC}	Friction loss coefficient of DC motor
K_{fg}	Friction loss coefficient of generator
K_{g1}	Stiffness constant of 1st pair gears
K_{g2}	Stiffness constant of 2nd pair gears
K_{hs}	High speed shaft stiffness constant
K_{ic}	Integral gain of the DC motor current control
K_{id}	Integral gain of d-rotor current control
K_{iq}	Integral gain of q-rotor current control
K_{is}	Integral gain of DC motor speed control
K_{ls}	Low speed shaft stiffness constant
K_{opt}	Optimal power tracking factor
K_{pc}	Proportional gain of the DC motor current control
K_{pd}	Proportional gain of d-rotor current control
K_{pq}	Proportional gain of q-rotor current control
K_{ps}	Proportional gain of the DC motor speed control
K_{wDC}	Windage loss coefficients of DC motor
K_{wg}	Windage loss coefficient of generator
$K_{\emptyset}$	DC motor constant
L_a	DC motor armature inductance
L_f	DC motor field inductance
L_G	Grid inductance
L_{lr}	Rotor leakage inductance
L_{ls}	Stator leakage inductance
L_m	Mutual inductance between stator and rotor
L_r	Rotor self-inductance
L_s	Stator self-inductance
n_{gb}	Gearbox ratio
n_{sr}	Stator-rotor turn ratio
P_r	Rotor active power
P_s	Stator active power
p	Pole pairs

Q_r	Rotor reactive power
Q_s	Stator reactive power
R	Wind turbine rotor radius
R_a	DC motor armature resistance
R_b	Brushgear rotor phase resistor
R_{ea}	External resistance in phase *a*
R_{eb}	External resistance in phase *b*
R_{ec}	External resistance in phase *c*
R_f	DC motor field resistance
R_G	Grid resistance
R_m	Magnetizing resistance
R_r	Rotor internal phase resistance
R_{ra}	Total rotor resistance in phase *a*
R_{rb}	Total rotor resistance in phase *b*
R_{rc}	Total rotor resistance in phase *c*
R_s	Stator phase resistance
r_{g1}	1st gear radius
r_{g2}	2nd gear radius
r_{p1}	1st pinion radius
r_{p2}	2nd pinion radius
s	Slip
T_{DC}	DC motor torque
T_g	Generator electromagnetic torque
$T_{g\,ref}$	Generator reference torque
T_{hs}	High speed shaft torque
T_{ic}	Integral time of the DC motor speed control
T_{is}	Integral time of the DC motor speed control
T_{ls}	low speed shaft torque
t	Time
V_a	DC motor armature voltage
$V_{ar\,ref}$	Rotor reference voltage in phase *a*
$V_{br\,ref}$	Rotor reference voltage in phase *b*
$V_{cr\,ref}$	Rotor reference voltage in phase *c*
V_{DC}	DC voltage link
V_{emf}	Back electromotive force

V_f	DC motor field supply voltage
V_G	Grid voltage
V_s	Magnitude of the stator phase voltage
v_{ar}	Rotor voltage in phase a
v_{br}	Rotor voltage in phase b
v_{cr}	Rotor voltage in phase c
v_{dr}	d-component of rotor voltage
$v_{dr\,ref}$	d-rotor reference voltage
v_{ds}	d-component of stator voltage
v_{qr}	q-component of rotor voltage
$v_{qr\,ref}$	q-rotor reference voltage
v_{qs}	q-component of stator voltage
$v_{\alpha s}$	α-component of stator voltage
$v_{\beta s}$	β-component of stator voltage
Z_G	Grid impedance
β	Pitch angle
ΔR	Rotor asymmetry percentage
δR	Increase of rotor resistance due to the fault existence
$\mathcal{E}_{i_a}$	DC motor armature current error
$\mathcal{E}_{i_{dr}}$	d-rotor error current
$\mathcal{E}_{i_{qr}}$	q-rotor error current
$\mathcal{E}_{\omega_{DC}}$	DC motor speed error
θ_{DC}	Angular displacement of DC motor
θ_{g1}	Angular displacement of 1st gear
θ_{g2}	Angular displacement of 2nd gear
θ_{hs}	Angular displacement of high speed shaft
θ_{ls}	Angular displacement of low speed shaft
θ_{p1}	Angular displacement of 1st pinion
θ_{p2}	Angular displacement of 2nd pinion
θ_{re}	Electrical angular displacement of generator rotor
θ_{rm}	Mechanical angular displacement of generator rotor
λ	Tip speed ratio
ρ	Air density
φ_{dr}	d-component of rotor flux
φ_{ds}	d-component of stator flux

φ_{qr}	q-component of rotor flux
φ_{qs}	q-component of stator flux
$\varphi_{\alpha s}$	α-component of stator flux
$\varphi_{\beta s}$	β-component of stator flux
ω_{DC}	DC motor angular speed
$\omega_{DC\ ref}$	Reference DC motor angular speed
ω_{g1}	1st gear angular speed
ω_{g2}	2nd gear angular speed
ω_{hs}	Angular speed of high speed shaft
ω_{ls}	Angular speed of low speed shaft
ω_{p1}	1st pinion angular speed
ω_{p2}	2nd opinion angular speed
ω_{re}	Electrical angular speed of the generator rotor
ω_{rm}	Mechanical angular speed of generator rotor
ω_s	Synchronous electrical angular speed
ω_T	Wind turbine speed

1 Overview of Wind Power

1.1 Introduction

The use of traditional fossil fuels for energy conversion has had a detrimental consequence on the environment as a result of mining effects, air and water pollution, acid rain and the consequent production of greenhouse gases and their effect on climate change. Driven by growing populations and expanding economies, global energy demand is currently increasing each year and is expected to rise by an average of 1.2% per year between 2005 and 2030 [1]. To balance these issues a reduction of carbon dioxide, CO_2, and other greenhouse gases emissions is needed to limit their contribution to global warming and potential climate change. Fig. 1.1 shows historical levels of CO_2 in the atmosphere over the last 1000 years, the early records before 1850 being taken from records of CO_2 dissolved in glacial ice and the recent records from air measurements. It is clear that the CO_2 concentration has increased considerably since 1769, the beginning of the Industrial Revolution and is probably caused by human activity.

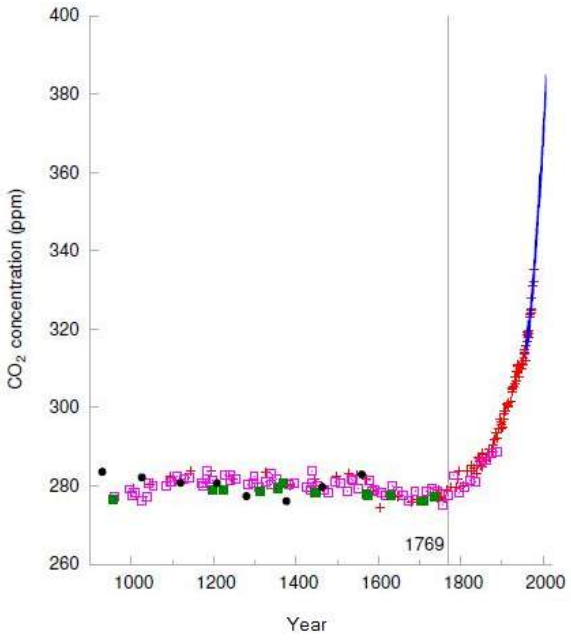

Fig. 1.1: Carbon dioxide concentration for the last 1000 year [2]

This has led to the encouragement of non-CO_2 producing energy sources, which are cleaner and hopefully safer, known as renewable sources. Therefore, renewable sources are becoming an important component of electricity generation in the world. Wind energy conversion systems (WECS) are the second most developed renewable technology, after hydroelectric production, and are set to play a significant role in the future energy supply around the world. Wind power has a number of advantages over conventional electricity generation methods:

- The fuel is free and not subject to fuel price variation, it does not have to be transported and it will not run out;
- It does not emit greenhouse gases into the atmosphere during generation, although greenhouse gases are produced during manufacture of WECS;
- Wind farms are quick to construct and easy to decommission, earning a positive income and encouraging development in rural areas.

Wind energy currently makes a significant contribution to the EU's energy and climate objectives, competitiveness and energy security. According to European Wind Energy Association (EWEA), a total of 93,957MW of wind power was installed in the EU by the end of 2011 with annual installations having increased steadily over the last 17 years from 814MW in 1995 to 9,616MW in 2011, an annual average market growth of 15.6% [3]. This was able to produce in 2011 204TWh of electrical energy, meeting 6.3% of the EU's total electricity demand [4]. Over the next 20 years, wind energy growth will continue and the EWEA expects 230GW of installed capacity in 2020 and 400GW by 2030. Wind power is gearing up to become the main renewable power technology in the EU. The National Renewable Energy Action Plan (NREAP) includes a target of 34% for renewable energy production of EU electricity consumption by 2020, with wind power producing 495TWh, meeting 14% of electrical energy consumption [5]. The remaining 20% of electrical energy consumption will be covered by other renewable energy sources, including hydro 10.5%, biomass 6.7%, solar photovoltaic (PV) 2.4%, concentrated solar power (CSP) 0.5%, geothermal 0.3%, tidal, wave and ocean 0.2%. Furthermore, the European Commission Energy Roadmap expects wind energy to be the key generation technology by 2050, supplying more electricity than any other technology and meeting 31.6-48.7% of Europe's electricity production [5].

Wind power will therefore consequently decrease the EU's total power production CO_2 emissions as a whole. For example in the EU, compared to thermal power stations wind power will avoid 0.696Mt of CO_2 emissions per TWh of production in 2010 [6]. Following the same approach and the European Commission's data for 2015, 2020, 2025

and 2030, the CO_2 emissions avoided can be calculated. As a result, it is calculated that wind energy will avoid 0.588Mt CO_2/TWh in 2020 and 0.560Mt CO_2/TWh in 2030. Wind energy will therefore have avoided 126Mt of CO_2 in 2010, equivalent to 28 % of the EU's Kyoto commitment. Following EWEA's base scenario, the installed wind power capacity in the EU will have avoided 35% of the Kyoto target. By 2020, wind should represent 31% of the EU's current target of 20% reduction [5], [7].

1.2 Offshore Wind Power

Offshore wind turbines (WTs) refer to those turbines which are built in water. Although the vast majority of current WTs have been sited onshore there is growing interest in installing them offshore because of higher wind speeds and less turbulent winds. Offshore WTs are currently built on fixed structures restricting them to shallow waters of maximum depth 30m less than 50km from shore. As the technology develops, valuable experience is being gained and a substantial proportion of future EU wind production will moving offshore and eventually into deeper waters, as suggested by Fig. 1.2, to benefit from greater wind resource further offshore and use larger WTs, possibly on floating platforms, which will harvest greater energy.

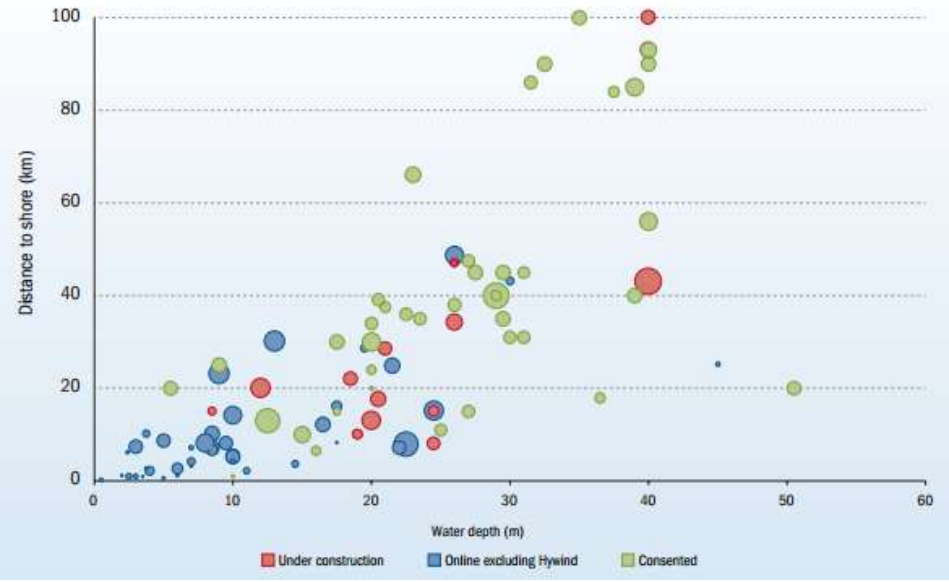

Fig. 1.2: Distance & depth of current & future offshore wind farms [7]

Offshore wind farms have higher construction costs compared to onshore wind farms because these projects need to withstand more extreme weather conditions.

However, the trend to place WTs offshore offers several advantages over onshore which are:

- Improved wind conditions, offshore wind speeds are potentially stronger, steadier and less turbulent than onshore. Some recent studies have showed that offshore winds blow 40% more often offshore than on land [8].
- Ability to build the larger WT due to transport issue and reduce concerns over visual impact or noise.
- Not subject to objections due to land-use disputes, limited land availability and restrictions associated with obstructions due to buildings, terrain and vegetation.

The first offshore wind farm was inaugurated in 1991, 2.5km off the Danish coast at Vindeby. It featured eleven 450kW turbines with a total capacity of 4.95MW. Until 2001, the growth of the offshore wind power sector was irregular and mainly depended on a handful of small near-shore projects in Danish and Swedish waters featuring WTs with a capacity of less than 1MW.

Since 2001, new offshore wind capacity has been installed every year and spread across twelve countries, ten in Europe and some lesser installations in China and Japan. Moreover, the share of new offshore wind capacity in total wind capacity additions has been increasing. Fig. 1.3 shows the increase in offshore WT capacity over the last 12 years in Europe as given by EWEA [9]. In 2001, only 50.5MW of installed offshore capacity represented 1% of total new European annual wind capacity. Meanwhile, 532MW was installed during the first six months of 2012.

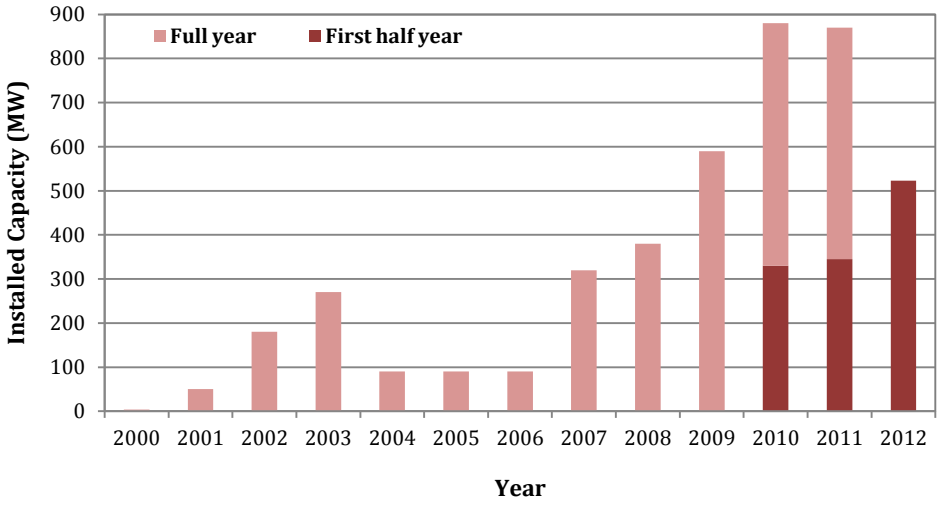

Fig. 1.3: Annual installed offshore wind capacity in Europe

Offshore WTs have historically been adapted from onshore designs, although some manufacturers are now developing new models designed specifically for the offshore environment. Offshore wind is typically less turbulent than onshore wind, due to the absence of hills, trees and buildings, but at the same time average and extreme wind speeds are higher than those onshore and the turbine is subject to the impact of waves and tides, leading to greater mechanical loading on structural and machine components. Combined with more challenging access conditions during installation and maintenance, this means that the design and manufacture of offshore WTs and foundations have unique requirements. These include corrosion protection, accessibility and safety procedures for service technicians and more sophisticated monitoring and control systems. To date, Vestas and Siemens have been the most prominent offshore WT suppliers. Consequently, Vestas's 3MW and Siemens's 2.3MW and 3.6MW models have been installed predominantly throughout Europe [10]. These turbines have rotor diameters of between 82 and 120m, which are significantly larger than the turbines deployed in the earliest projects.

In recent years, larger offshore turbines have been developed by Enercon and Vestas, the E-126 and V-164 respectively. The E-126 turbine, with a direct-drive, wound synchronous generator, stands at 135m hub height, with rotor diameter 127m and rated power 7.58MW. This turbine has not been deployed offshore because it has proved too heavy. The V-164, with a geared-drive 7MW permanent magnet synchronous generator, is designed with rotor diameter 164m. Building further on this, Vestas is developing a prototype of 8MW turbine for the offshore environment. In terms of rated power and rotor diameter, Fig. 1.4 illustrates the growth in offshore WT sizes [7]. It is clear that this trend of increasing capacity, up to 10MW, is set to continue into the future.

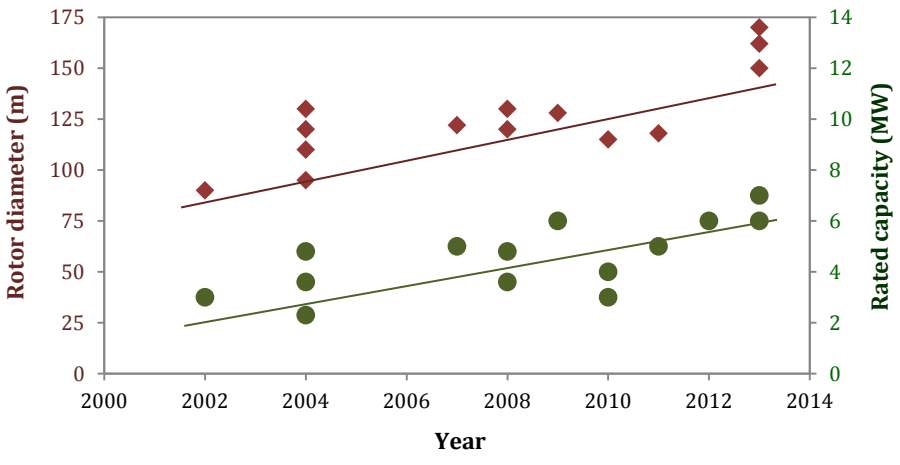

Fig. 1.4. Growth trends in offshore WT size

However, offshore technology is expensive due to installation, construction and grid connection costs. Coupled with this, is the extra cost of operation and maintenance (O&M) of offshore wind due to access issues. These factors contribute to raising the cost of offshore wind energy and slowing the payback time on that capital investment. Although offshore wind power is cheaper than other renewable technologies, such as hydropower, it is still more costly than onshore wind [11]. As offshore wind energy grows towards a major utility source, reducing the cost of energy (CoE) will become a critical issue in order to make this power competitive to conventional sources. However, as happened with onshore wind, these costs are expected to drop as technology improves and more experience is gained.

To improve the economics of offshore wind power, more emphasis is being placed on reducing the total life cycle costs as well as reducing the initial investment costs. So it is a prerequisite to control and reduce O&M costs so that the total offshore wind life-time energy costs can be reduced. In comparison with onshore, offshore WT O&M is more difficult and the cost was estimated by industrial collaborators at between 3 and 5 times the onshore cost [12]. This is because the access to turbines for maintenance and repair may be restricted during periods of high wind speed and significant wave height, particularly during the winter. Also, repair and maintenance require usage of cranes and lifting equipment creating a capital-intensive operation as well as delayed services due to lack of crane availability and need for optimal weather conditions. Combined with unpredictable component failures, these issues can result in poor reliability reducing the availability of the turbine due to the longer downtimes. For example, in Northern Europe [8] 10-50% of all offshore work-hours are lost due to bad weather. Moreover, small component failures offshore could incur higher personnel costs which can amount to €1000 per man-day [13]. All these factors increase O&M costs offshore by up to 30% of total income from a offshore wind farms with operating life over 20 years [14]. Larger turbines may reduce the O&M cost per unit power, but the cost per failure is likely increased. Therefore, there is a need for early warning when WT problems are about to occur. For such situations, condition monitoring systems (CMSs) have greater benefit for the offshore WT.

1.3 Growth of Offshore Wind Power in UK

The UK is a windy country, one of the windiest in Western Europe, which gives it one of the largest wind energy development potentials in the world, influencing the

growth of the wind power industry over recent years in the UK. This increase can be seen from the annual increases of offshore installation shown in Fig. 1.5, which was adopted from [15], and is expected to continue for 2013 and 2014.

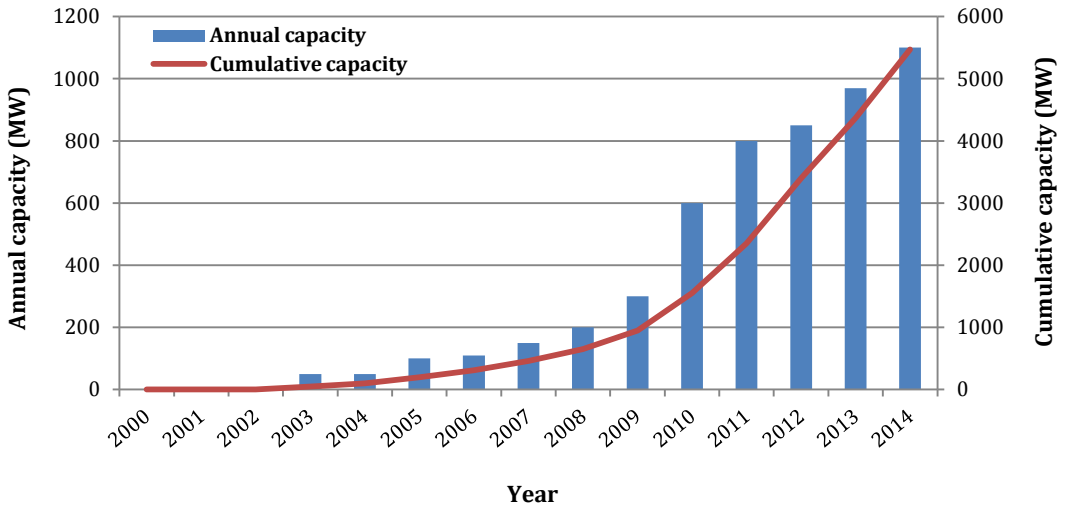

Fig. 1.5: UK offshore wind power annual & cumulative installations

Historically, the front-runner in offshore wind was Denmark. But by the end of 2010, with a total offshore installed capacity of more than 1GW, UK became the world leader of offshore wind power generation [5]. During the first six months of 2012, the UK installed and fully connected 114 offshore WTs, with a combined capacity of 422MW. Overall, 8 wind farms were under construction. This work carried out on these wind farms is summarized and illustrated in Fig. 1.6.

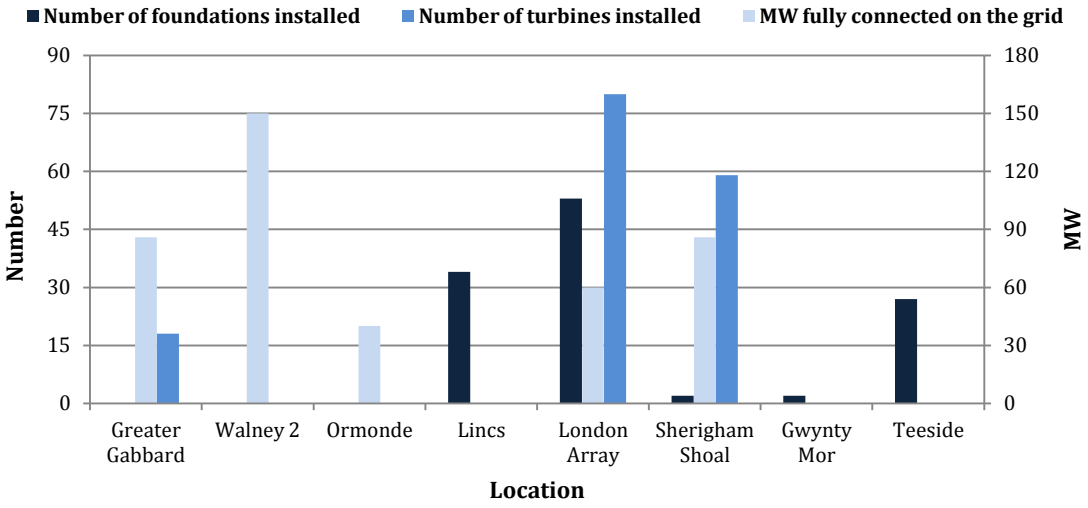

Fig. 1.6: Installation & grid connection of UK offshore WTs 1st Jan-30th Jun 2012 [9]

According to RenewableUK, UK currently has installed 568 offshore WTs exceeding 1,800MW, and a further 665 turbines are under construction totalling 2,359MW [16]. The UK also now has the largest offshore wind farm in the world, Walney rated at 367MW, located off the Cumbria coast which was opening in February 2012. Given the current construction and development, the UK has been estimated to have as much offshore capacity already installed as the rest of the world put together. Moreover, the latest study on wind power deployment trends carried out by RenewableUK, established that by the end of 2016 there will be 8GW of offshore wind capacity installed in the UK and by 2020 it will exceed 18GW.

1.4 Renewable Power in Libya

Although Libya is one of the world's largest oil and gas exporting countries it has identified the existence of potential renewable energy resources. Due to its good geographical location in the north of Africa, Libya is in the heart of the Sun Belt. With 3000-3500h/y sunshine and an average solar radiation of 2,470kWh/m^2/day, some studies have shown that Libya has one of the highest solar radiations in the world [17]. Moreover, due to this high solar intensity, Libya is expected to have a potential wind resource. That because the air becomes hot and rises, creating a low-pressure area in Libya. This low pressure will pull the air towards Libya from cold regions surrounding that have high pressure. The movement of air constitutes the wind flow in Libya. This was proven in 2004 when the measurement of wind speed statistics at different locations in Libya showed that the average wind speed at a 40m height is between 6-7.5m/sec [18], which makes Libya an attractive global location for wind farms. Fig. 1.7 illustrates the distribution of the average solar radiation and wind speed in Libya.

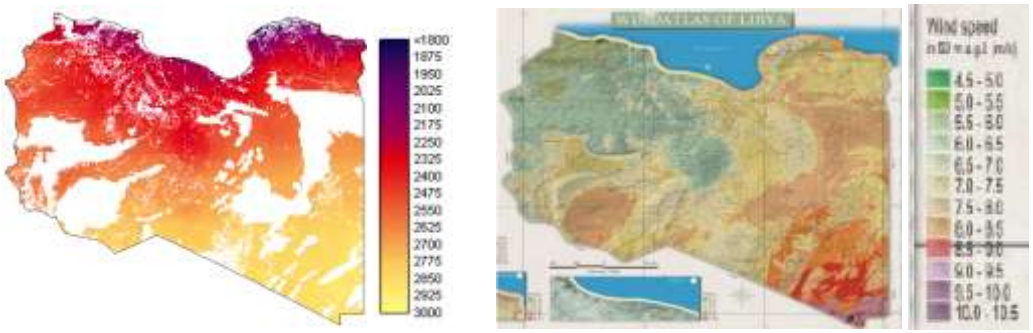

(a) (b)

Fig. 1.7: Average measurements in Libya of:
(a) solar radiation in kWh/m^2/day
(b) wind speed in m/sec [17]

According to General Electric Company of Libya (GECOL), the electrical energy produced has increased with annual growth rate 8-10% during the past few years as shown in Fig. 1.8 [17] to meet an increased electricity demand in Libya. However, the forecast assumes this growth will continue for the electricity demand over the next few years. In order to meet this future electricity demand in a sustainable manner and reduce the costs of the national electricity production, the government needs to put together a strategic long-term energy sector road map. Therefore, Libya's goal is to increase the share of renewable energy sources of the entire energy production within the near future.

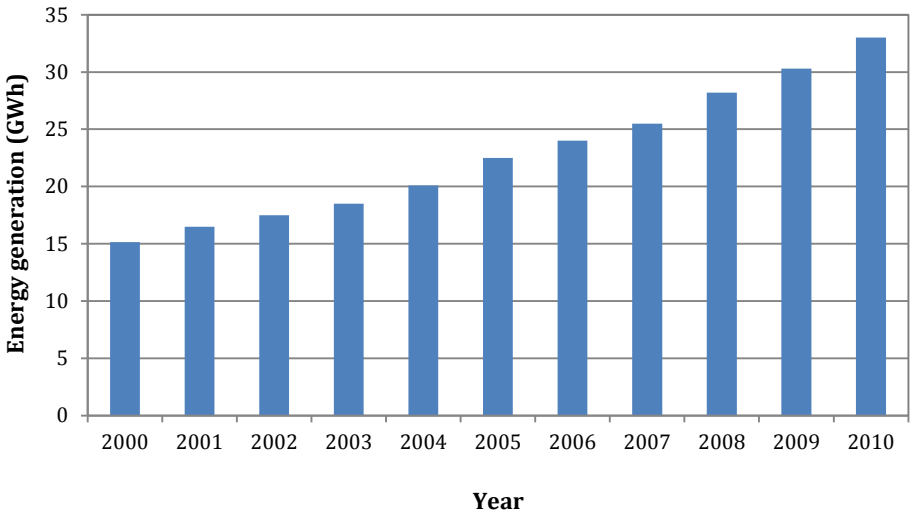

Fig. 1.8: Energy generation in Libya from 2000 to 2010

In 2000, GECOL began seeking professional engineering expertise to qualify the country's wind energy potential. Libya joined the wind energy field by awarding a contract for the installation of a 25MW pilot project wind farm in February 2001. This project aimed to build a commercial wind farm to generate electricity from a renewable energy source on economic terms and educate local engineers in the requirements and factors of wind farm development. The project included an evaluation of potential wind farm sites regarding profitability and feasibility, wind measurement equipment, turbine construction, and an accompanying scientific program with on-the-job software- and course-training for the Libyan partners. In addition to promoting the development of renewable energy in Libya, the Renewable Energy Authority of Libya (REAOL) was established in 2007 [17]. REAOL has set a target to cover 10% of Libya's energy supply from renewable energy resources by the year of 2020 and 25% by 2025 [17], [19]. In order to meet these objectives, REAOL has developed a roadmap for the expansion of renewable energy production capacity. Furthermore REAOL has prepared a mid-term

plan (2008-2012) and as well as a long-term plan to promote renewable energy and to meet these targets [20]. These plans address projects in solar and wind and the possibilities of stimulating local manufacture of equipment for renewable energy. REAOL handed the roadmap over to the Ministry of Electricity and Energy, which approved the roadmap. However, that Ministry has now been disbanded.

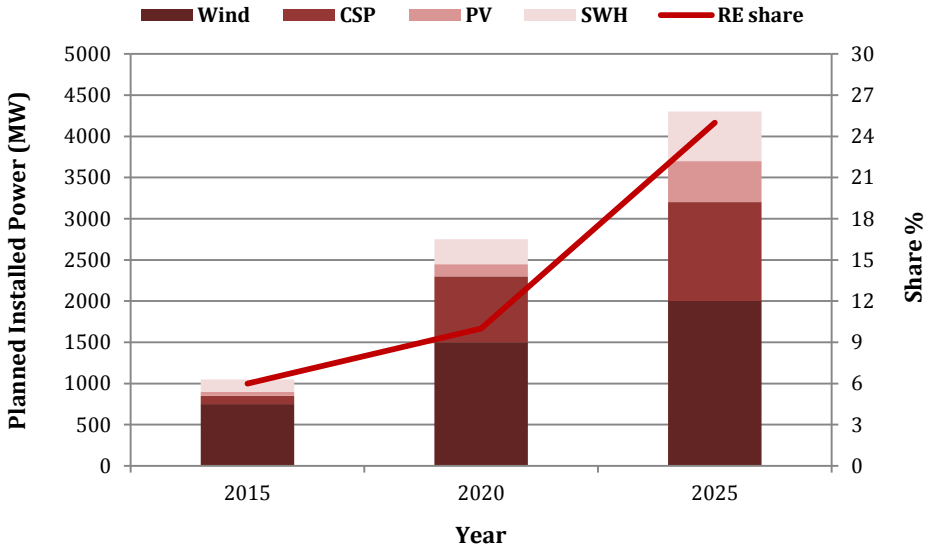

Fig. 1.9: REAOL roadmap for renewable energy expansion in Libya

However, according to a Libyan report released in December 2009, these goals might take longer to reach than REAOL's goal [19]. That report said, "Unfortunately, these targets and strategy for renewable energy in Libya do not seem to be fully shared among all participants, despite the approval of the target by the Cabinet. One reason seems to be that the targets and strategy have not been developed from any comprehensive analytical work. This lack of consensus means that the programs and targets of REAOL may not in fact be realized on the time-scale envisaged." [19]. This has resulted in delaying the start of building the first wind energy project until the beginning of 2011. This farm is sited in Al-Fetaih, near Darnah on the north east coast consisting of 37 WTs with a capacity of 61.75MW. The project would include the turbines, control equipments, electric transformers, operation and maintenance building, electric lines, service roads, control rooms and workshops. The cost of the project is about 180million LD (£ 90million) and planned to take a period of 20 months [21]. The Libyan scenario of wind energy development is continued with such projects include wind farms in Darnah (2nd stage with 60MW); Al Maqrun (240MW in two stages); western region farms at Meslata, Tarhuna, and Asaba (250MW); southeastern region wind farms at Gallo, Almasarra,

Alkofra, Tazrbo (120MW); and southwestern region wind farms at Aliofra, Sabha, Gatt, and Ashwairef (120MW) [17], [19], [20].

For the solar energy, by the end of 2010, Libya has installed a total 4MW PV with expanding 2MW from this technology to remote areas. The medium-term solar plan comprises the building of large scale 5-10MW PV plants and connecting to the Aljofra, Green Mountain and Sabha grid. Furthermore, it is proposed to develop a joint venture between local and foreign investors for the manufacture of solar water heaters (SWHs) and PV Modules to satisfy local needs and for export to international markets. Libya is also looking into adding 1,000 PV rooftop systems for residential areas (3MW) with a feasibility study for a CSP plant reportedly underway (100MW) [17], [19], [20].

In the wake of the Libyan revolution between15th February and 20th October 2011, after the war against the Al Gaddafi regime, the Libyan energy sector has been generally affected due to difficult situation and lack of security in some regions in the country. This has affected the renewable energy programme, where progress in the medium-term plan has been affected by delaying and stoppages in construction at some locations. The new Libyan Ministry of Electricity and Renewable Energy, founded in 2011 after the war, has upgraded the medium-term plan with consideration to the costs, locations and the work, which has restarted. Furthermore, due to high potential for renewable energy in Libya and its geographical location near to the European energy market, the Ministry is planning to generate electricity from renewable sources in the southern Libyan regions and to deliver it to Europe. This is known as the DESERTEC project [18]. However, even though Libya has an potential solar and wind energy sources and steps having been taken to develop that sector, the contribution of these resources in the electricity generation to date, has had a negligible effect in Libya, as shown in Fig. 1.10 [17].

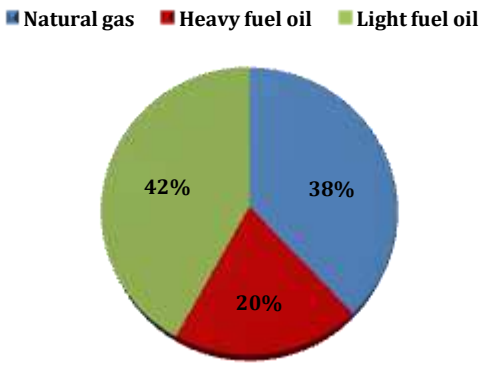

Fig. 1.10: Electricity generation in Libya by fuel type in 2010

1.5 Variable Speed WTs with Doubly-Fed Induction Generators

Various WT concepts have been developed over the last 30 years. Referring to the turbine rotational speed, these concepts can be classified as fixed speed, limited variable speed, and variable speed. For variable speed WTs, based on the generator type and the rating of power converter, they can be further classified into wind generator systems with partially-rated or fully-rated power electronic converters. When the turbine drive train is considered, these concepts can be classified into geared- or direct-drive systems. This research considers only the variable speed WT with doubly fed induction generator (DFIG). In Fig. 1.11(a), a basic layout of a DFIG WT system is shown.

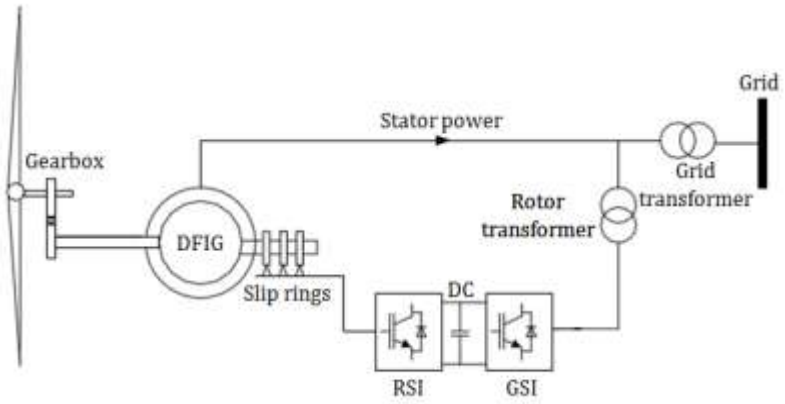

(a)

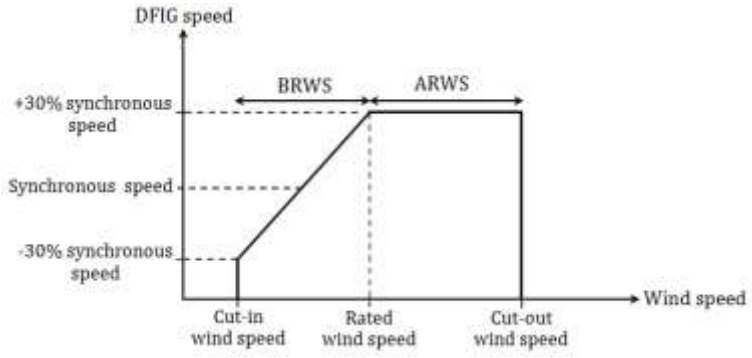

(b)

Fig. 1.11: (a) variable speed WT with DFIG (b) generator speed versus wind speed

It consists of wound rotor induction generator (WRIG) and a partially-rated power converter connected to the rotor circuit to recover or inject slip power. The term doubly-fed refers to the fact that the stator and rotor windings are separately connected to the grid and the back-to-back converter respectively. The gearbox has the role of matching

the speed between the blades and the rotor. The transformer couples the generator to the grid adjusts the voltage of the machine to that of the grid. The back-to-back converter consists of two voltage source inverters (ac-dc-ac) having a dc link capacitor connecting them. The rotor side inverter (RSI) takes the variable frequency voltage and converts it into dc voltage and vice versa. The grid side inverter (GSI) has the dc voltage from the dc link as input and ac voltage at grid parameters as output and vice versa. The application of power electronics provides control of rotor frequency and thus rotor speed. As shown in Fig. 1.11(b), this turbine operates under variable speed range (above and below 30% the synchronous speed) below rated wind speed (BRWS), while it operates at fixed speed (30% above the synchronous speed) above rated wind speed (ARWS). The rating of the power electronic converter is only 30% of the generator capacity, which makes this concept attractive and popular from an economic point of view. Moreover, the system has high energy efficiency, improved power quality and easy control of active and reactive power. Therefore, the DFIG concept is used in more and more in wind applications and it was reported by EWEA that it represented >55% of European market in 2010 [22]. Conversely, its drawbacks are the need for slip rings, a gearbox and a complex controller [23].

1.6 Thesis Outline & Original Contribution

1.6.1 Thesis Outline

After this background information on the wind power in Chapter 1, introducing the size of the offshore wind market in the UK its growth and the importance of condition monitoring (CM) to reduce O&M costs, introducing an overview of the current and future plans for renewable power in Libya, and finally introducing the DFIG concept used in the WTs, based on that this section sets out the work in this thesis commencing in Chapter 2.

Chapter 2 provides a discussion of WT reliability. Various reliability studies are presented and their results show the failure rate of the turbine components for different WT concepts and determine the sub-assemblies that are of most concern for O&M. Furthermore, WT CM is presented in this chapter with details of the monitoring structure for modern WTs. Some existing CM techniques and research are reviewed.

Chapter 3 describes WT drive train Test Rig for the development of CM. This includes a history of the development of the physical Test Rig and its MATLAB Simulink model with detailed information on the Test Rig components and instrumentation.

Moreover, this section validates the MATLAB Simulink model with the physical system in the time and frequency domains. The parameter values for the electrical, control and mechanical Rig components are provided.

Chapter 4 presents the design of a RSI controller for the Test Rig DFIG; namely active- and reactive-power control, based on the stator flux-oriented vector control (SFOVC) scheme. This includes developing the generator mathematical model and pre-defining the optimal power extraction-speed characteristics curve. In addition, the evaluation of the controller performance with MATLAB model and the physical Test Rig is also given in this chapter.

Chapter 5 contains the theory of electrical faults in the DFIG rotor, and the derivation of fundamental fault equations for various fault-like conditions inside the proposed CM signals. Also, the signal processing and fault detection algorithm, which has been applied to analyse the results, is proposed and introduced mathematically.

Chapter 6 presents the Test Rig simulated and measured results for different operating conditions. These results include the Fast Fourier transform (FFT) analysis of the proposed signals and their sensitivity to the fault severity. Then, the proposed fault detection algorithm is compared with other detection algorithms previously published to discuss advantages and drawbacks and shows the improvement in detection sensitivity achieved by monitoring within the control loop.

Chapter 7 presents the conclusions of this research. It also contains a discussion of future work, including investigation of potential new areas for WT-driven induction generator.

Finally, a list of references has been used in this research as well as a number of appendices comprise information and results for the Rig and the research are presented at the end of this thesis.

1.6.2 Thesis Original Contributions

The results of this work are expected to provide valuable development in WT CM for the lowering of offshore O&M costs and the key contributions can be briefly summarised as:

- Generator control signals of WTs are proposed for WT generator CM. Comprehensive simulation and experimental work for these signals, considering

operating condition of the turbine, with different fault severity has been achieved. Furthermore, the proposed signals are expected to be a significant step towards developing a reliable CMS for offshore WT generators.

- Comparisons between and evaluations of various generator control loop signals, stator current and stator total power for detecting electrical WT faults are made. The advantages and drawbacks of each signal alternative are addressed. The results of this investigation are expected to provide valuable knowledge for selecting the best signal for detecting WT faults.
- Developing the physical Test Rig at Durham University from open loop system into closed loop system to represent the variable speed WT-driven DFIG. This includes installation of back-to-back converter on the rotor side with designing RSI controller and building using MATLAB Simulink and then loading it into the physical system using xPC TargetBox.

In addition to these main contributions several minor contributions are as follows:

- Building a complete MATLAB models for the physical Test Rig with both WRIG and DIFG configurations including all mechanical, electrical and control subsystems. These models have been confirmed against the physical system in both the time and frequency domains.
- The effects of DFIG WT rotor electrical asymmetries on the control loop signals have been derived. Subsequently, the fault-related harmonic frequencies to be monitored have been identified.
- A simple FFT has been proposed in this research to analyze these signals and evaluate which gives the best fault indication and early detection.

2 WT Reliability & Condition Monitoring

2.1 Reliability

The previous chapter, made clear that the down-side of wind power is not only capital-intensive manufacturing and installation of the turbines, but also the relatively high cost of O&M, particularly offshore. Due to turbulent operating conditions from the wind and weather, WTs are subjected to various failures. Moreover, the logistical and practical difficulty of replacing major WT components due to unanticipated failure, especially serial failures, has a large impact on lowering turbine reliability. Poor reliability directly reduces power generation availability, due to turbine downtime, and increases O&M costs. These factors all raise the CoE. Therefore, the WT system reliability is a critical factor in the economic success of a wind energy project.

2.1.1 Reliability Definition

The reliability of a turbine can be defined as the probability that turbine will function at full capacity during appropriate wind conditions at a site with specified wind resources for the turbine life-time or a defined sub-set of that life-time. The reliability can be expressed as a percentage probability or as failures/yr. A widely accepted life-time for a turbine is 20 years [24], however, longer life-times may be practicable. One of the most graphical characteristics, usually used by reliability specialists is the Bathtub curve, shown in Fig. 2.1, which describes the failure intensity ($\lambda(t)$) of the turbine during the life cycle. At the bottom of the bath-tub the $\lambda(t)$ becomes a constant λ and can be called a failure rate in failures/yr. Reliability can also be expressed as the reciprocal of failures/yr, that is mean time between failures (MTBF), hrs. The MTBF for a WT or component can be calculated as the total operational hours divided by the number of failures for that component [24].

$$\text{MTBF} = \frac{Operational\ time\ (hr)}{Number of failures} \tag{2.1}$$

$$\lambda = \frac{1}{\text{MTBF}} \tag{2.2}$$

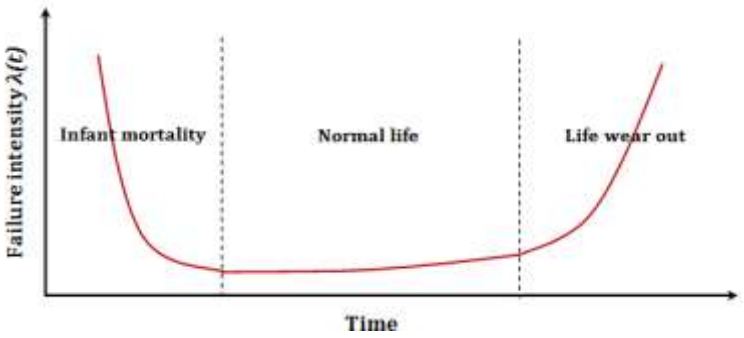

Fig. 2.1: Typical Bathtub curve or life cycle for a WT

Another principal system performance measure is the mean time to repair (MTTR), reciprocal of the repair rate (μ), repairs/yr, which is the average time for a repair or replacement to be made divided by the number of failures for a given component [24].

$$\text{MTTR} = \frac{Total\ repair\ time\ (hr)}{Numberof failures} \tag{2.3}$$

$$\mu = \frac{1}{\text{MTTR}} \tag{2.4}$$

However, the most significant reliability metric in the operation of wind plants is availability (A). This is expressed as a percentage and it is the amount of time that a system or component is available for use divided by that total amount of time in the period of operation. Another way to state this is the fraction of the "up-time" divided by total time. Up time can be expressed as the mean time to failure (MTTF), the period when a component is operational, and the total time is the MTBF.

$$A = \frac{\text{MTTF}}{\text{MTBF}} \tag{2.5}$$

Furthermore, reliability assessment not only focus on measuring the probability of failure, but also the costs of failure caused by system downtime, cost of spares, repair equipment, personnel and cost of warranty claims which directly affect on the O&M cost and thus the CoE. The turbine's reliability depends on:

- The particular machine model;
- That machine model's design;
- The quality of manufacture;
- The quality of maintenance;
- The operating environment, that is the wind resource and weather conditions at the site;

- The machine's reaction to that environment, which determines the loading imposed on its components.

2.1.2 Reliability & the Cost of Energy

The CoE is commonly used to evaluate the economic performance of the power plants. An approximate calculation equation has been adopted by the Department of Energy in the Low Speed Wind Turbine (LSWT) program, and accepted by the wind energy research community, to estimate the WT system CoE(£/kWh) [25]:

$$\text{CoE} = \frac{ICC \times FCR + LRC}{AEP_{NET}} + \text{O\&M} \tag{2.6}$$

$$AEP_{NET} = AEP_{GROSS} \times A \times (1 - Loss) \tag{2.7}$$

where *ICC* is initial capital cost (£), *FCR* is fixed charge rate (%yr^{-1}), *LRC* is levelized replacement cost (£/yr), O&M is operations and maintenance costs (£/kWh) and *AEP* is annual energy production (kWh/yr). This calculation includes component reliability in determining the *AEP*, O&M, and *LRC* terms. *AEP* is affected by component reliability through turbine downtime associated with both scheduled or preventive and unscheduled or repair maintenance. The O&M comprises of both scheduled and unscheduled maintenance costs, including expenditures for replacement parts, consumables, manpower and equipment. *LRC* is related to main overhauls and component replacements over the life of a turbine. Usually this category includes only major components and is based on components whose expected life is less than the WT's design life. Although the major component lives are commonly designed to be equal to the turbine's design life, there are numerous examples where the design life for major components is not realized in practice. This discrepancy has happened due to inappropriate design assumptions, inadequate knowledge about the true operating environment and manufacturing quality control issues.

According to the data from the Committee on Climate Change (CCC) [26], the levelized CoE for UK onshore wind was estimated between 6.6 and 9.3p/kWh while offshore ranged from 11 to 19.7p/kWh in 2011. These estimations take into account investment, fuel, and operation and maintenance costs, and relate them to total energy supply over the assumed economic life of a WT. Based on these data, an interesting comparison was made with the levelized CoE for the other technologies of relevance for the UK energy in 2011 and 2030 and illustrated in Fig. 2.2. Overall, it has been expected

that all renewable resources will be cheaper in 2030 and onshore wind appears likely to be one of the cheapest energy technology in future.

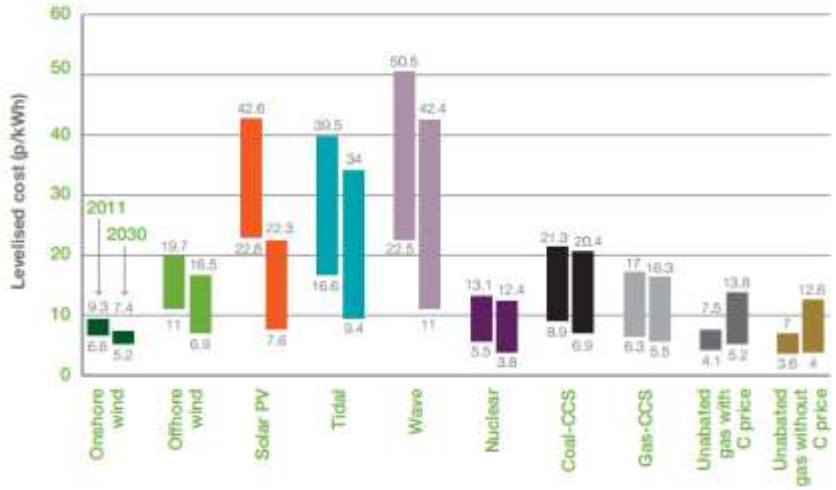

Fig. 2.2: Levelized CoE for different UK energy sources projected from 2011 to 2030 [27]

It is important to recognize that these estimates for 2030 were made on the basis of the evolving renewable technologies, with a potential impact on the reduction of the capital costs and extended the lifetime. For wind energy, cost reduction efforts in general will focus on improving component reliability and on reducing the cost to perform maintenance. To achieve that, it is necessary to have a clear understanding of the factors which drive reliability in the turbine, practically for offshore where the wind energy harvest is greater but the conditions are more inclement and the access to those turbine is more limited. Therefore, there are many efforts which have already been made by researchers and manufacturers in the sector. These researches included understanding failure rates, forestalling failures, managing efficient repairs and replacements, and having optimum spares inventory. The next section presents a brief synopsis of previous work done to enhance WT reliability.

2.1.3 WT Reliability Studies & Failure Statistics

Several surveys of WT reliability have been published over recent years based on analysis of real WT operational data. These data are regularly collected from wind power plants by the control unit inside the turbine. One source of these data source is WMEP which is available in the public domain. WMEP was established by the German Federal Government as the scientific measurement and evaluation programme

(Wissenschaftliches Mess- und Evaluierungs Programm), included in the German subsidy measure "250MW Wind", for monitoring 1500 WTs over the period from 1989 to 2006. The resulting data base contains a quantity of detailed information about reliability and availability of WTs. It provides the most comprehensive study of the long-term behaviour of WTs worldwide and the most reliable characteristic values concerning reliability. Nevertheless, besides this data base other publicly available sources of experiences do exist. Table 2.1 gives an overview of some existing failure statistics.

Table 2.1: WT failure statistics data adopted from [28] & [29]

Data source	Country	Time	Number of turbines	Turbine type
WMEP	Germany	1989-2006	15400	Fixed and variable speed with geared or direct drives
LWK	Germany	1993-2006	5800	Fixed and variable speed with geared or direct drives
Windstats	Germany Denmark	1995-2004 1994-2003	4285 904	Fixed and variable speed with geared or direct drives
ReliaWind	Europe	-	350	variable speed with geared or direct drives
VTT	Finnland	2000-2004	92	-
Elforsk	Sweden	1997-2004	723	-
Felanalys	Sweden	1989-2004	786	-
EPRI	USA	1986-1987	290	-
NEDO	Japan	2004-2005	924	-

The study of WT operational statistics gives knowledge of reliability performance, failures, and downtimes and verifies correctness of the predicted system lifetime. Tavner at al. [30] carried out a study on WT failure based on data recorded in the surveys a WindStats and LWK in Germany and Denmark. It is mainly focused on comparing the failure rates of fixed and variable speed, direct and indirect drive WTs. This study demonstrated that the direct drive turbines do not appear to have a lower failure rate than geared turbines. The failure rates of gearboxes in indirect drive WTs were also greater than indirect drive WT converter failure rates. However, the aggregate failure rates of converters and electronics in direct drive WTs were greater than the failure rate of gearboxes in indirect drive ones. For a larger direct drive WTs the failure rate for generators is at least double that of the indirect drive WTs.

Further analysis on the above data was conducted in [31]. It has been shown that an onshore average failure rate of 1-3 failures per turbine per year is common, it is unlikely to be acceptable offshore where access may be limited to one visit a year. Later, the

maximum failure rates of 0.5 failures per turbine per year would be necessary offshore, as suggested by Spinato at el. in [32], in order to planned maintenance visits need to be kept at or below once each year. The study also carried out analysis for the reliability of WT sub-assemblies and the results is demonstrated in Fig. 2.3.

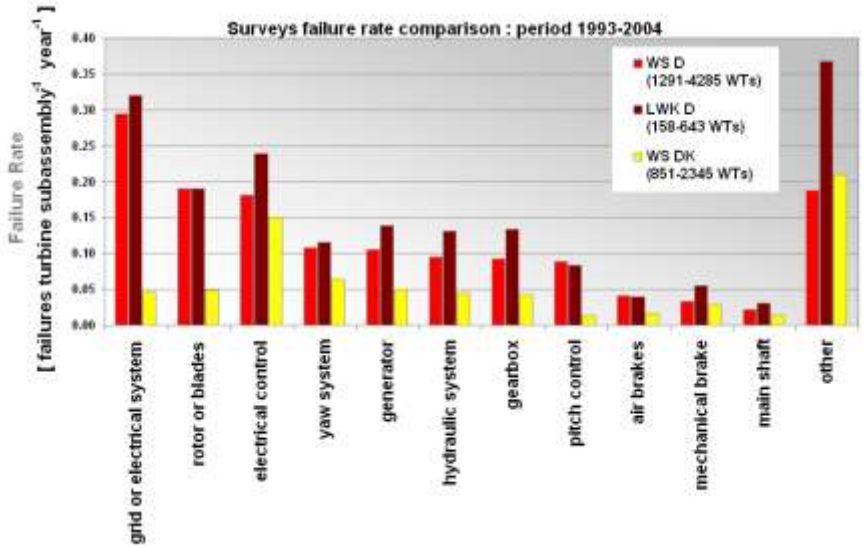

Fig. 2.3: Distribution of Failures within WT sub-assemblies from WSD, WSDK & LWK data [32]

Although the failure rates of mechanical sub-assemblies, such as the yaw system, blades and gearbox, are not the highest in the WT; their downtimes, particularly the blades and gearbox, are the highest among all the onshore WT sub-assemblies [33], as illustrated in Fig. 2.4. This is not due to their intrinsic design weakness but rather the complexity of changing them in the field, entailing the use of cranes and the need for prior planning [29]. Furthermore, Faulstich et al. [34] has shown that 75% onshore WT failures cause only 5% of the downtime while 25% of failures cause 95% of the downtime. According to Tavner [29], the 75% of failures, where downtime is normally short, are mostly associated with the electrical plant, the converter, electric pitch system, control equipment switch, whose defects are relatively easy to fix in onshore environment. These figures are likely to be dramatically changed as WTs go offshore, when the 75% short duration failures, which cannot be repaired quickly due to lack of access, will start to have a knock on effect in the downtime.

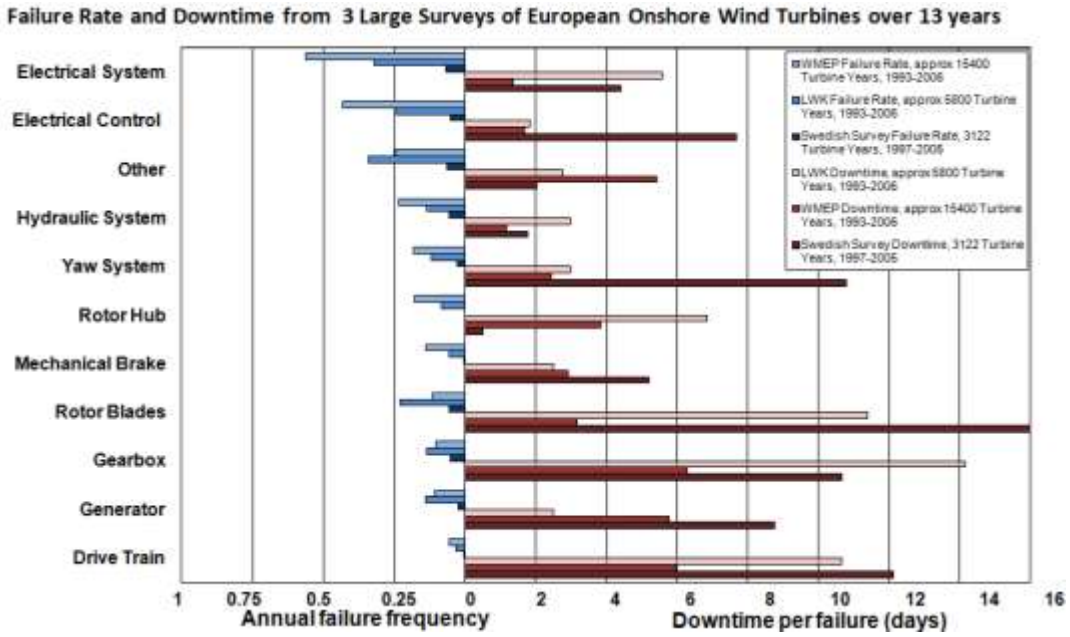

Fig. 2.4: WT failure rate & downtime per failure from results for onshore WTs from 3 surveys (WMEP, LWK & Scandinavian) including >24,000 turbine-years of operation [33]

A simple comparison of WT generator reliability against other electrical rotating machines has been done by Tavner, based on data reported in [35] and [36]. Fig. 2.5 shows the results, which have also been published in [37], including failure data from more than 3400 induction motors (IMs) and 990 WT induction generators (IGs). It can be seen that the main source of failures has root causes in; the bearings, the rotor and the stator. Among all the failures the bearings are dominant. Also, the rotor failures contribute significantly to total generator failures in WTs, particularly in small and medium WT generators.

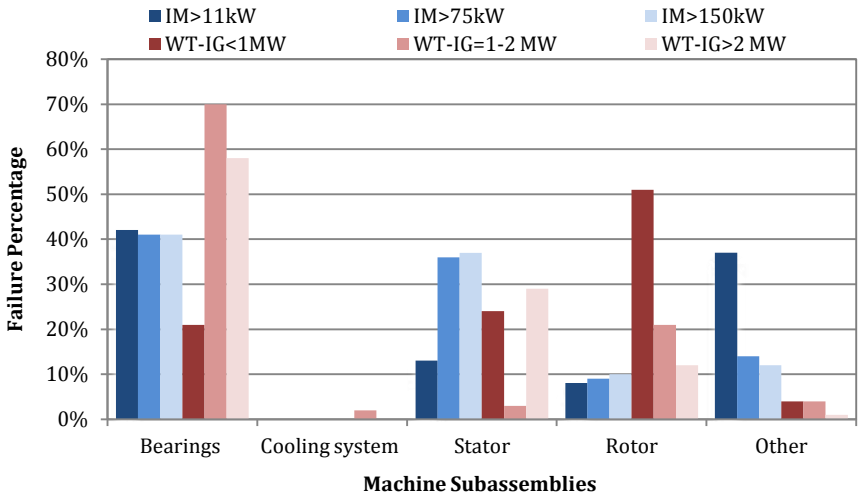

Fig. 2.5: Distribution of failed sub-assemblies in induction machines

The reliability of WTs is of course strongly dependent on the size of WT in use, as reported in [32]. The work utilised failure rates data over 11 years from 12 onshore WT models from the LWK survey. Fig. 2.6 summarises the results which shows the general trend of failure rate rising with WT rating. Based on this result, it seems that it may be difficult to decrease initial failure rate as turbines continue to grow in capacity, although reliability improvements are always being introduced. For offshore location, this causes concern where the turbine rating is being increased to raise energy production and reduce CoE. Besides the size of WT there are more parameters, which need to be considered in an appropriate reliability analysis. The influence of weather conditions has an important effect on the availability characteristics of WTs. An example of these parameters can be found in the wind speed, which was already analysed in [38] where the dependency of failure rate on wind speed was shown, but was significantly stronger for electrical than other sub-assemblies. Furthermore, a study by Tavner et al. [39] carried out a physical check on the variation of failure rate with wind energy index (WEI) based on analysis of Danish WT field data from Windstats. The results are given in Fig. 2.7, where the failures in a given month throughout the period have been summed up and compared with the summed WEI in that month. It is obvious that failure rates peak in the winter, at the same time of year as the WEI peaks, but a secondary peak in the WEI also occurs in the autumn. This confirms a relationship between WT failure rate and the WEI, which coincides with weather seasonality.

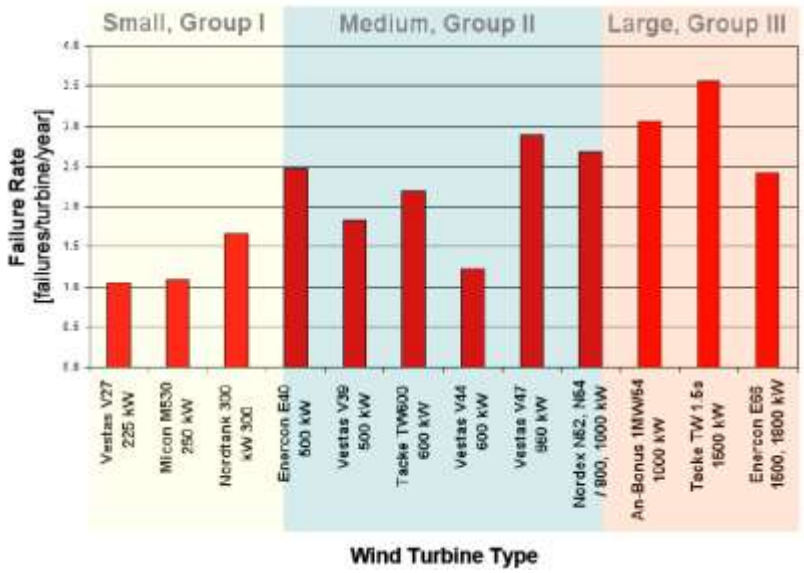

Fig. 2.6: Distribution of failure rates between different WT models [32]

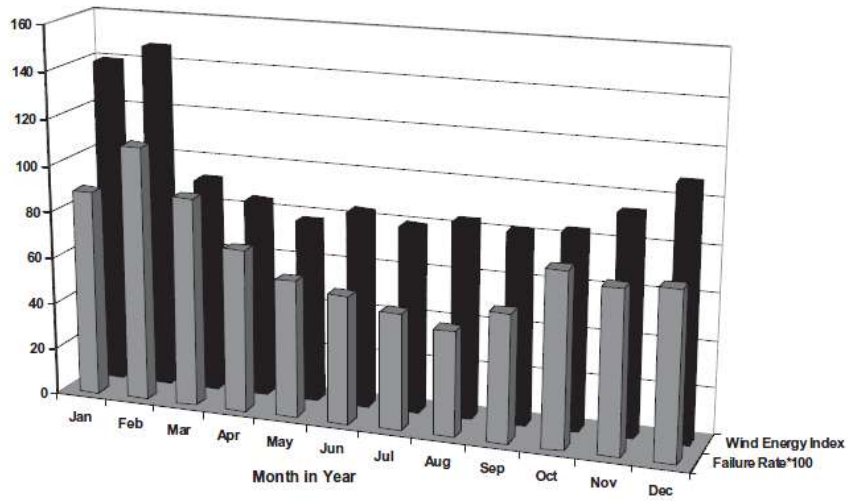

Fig. 2.7: Correlation between failure rate & WEI [39]

For offshore, with increasing turbine capacity and site access difficulties, WT and sub-assembly reliability needs to improve. Improvements have to be achieved in the design and the maintenance plan, otherwise availability will reduce and repair & maintenance costs increase. However, improvements will not be possible if failure rates remain high. In order to prevent failures, mitigate the consequential damage and reduce repair & maintenance costs there must be suitable techniques for detecting incipient WT failures in the early stage. This would allow the operator to incorporate maintenance actions into planned site visits negating the need for unplanned maintenance. For such situations, the CMS and faults diagnosis methods have potential benefits for the wind industry.

2.2 WT Monitoring

The CM is the process of monitoring and providing information on the condition of system components and prediction of incipient failures within those components at an early stage of failure. The use of CM allows maintenance to be scheduled, or other actions to be taken to avoid the consequences of failure, before the failure occurs. Furthermore, success in detecting and repairing such potential failures not only prevents failure, but also has other system benefits, such as maintenance cost reduction, personnel safety development, more efficient plant operation with consistent quality, plant availability and reliability improvement. The CM involves sensor measurements to determine the condition of the process, analysing measured signals, detecting a process anomaly and detecting faults are necessary factors of the monitoring process. Today, CM is becoming a

long-term service package for many rotating machine component applications, but in the wind power industry it is a relatively new approach.

In the early years of WT operation maintenance and repair practices were predominantly reactive, i.e. to operate the WTs until failure [40]. As WTs have grown in rating and size, preventive maintenance (PM) has become more accepted. Many WT owner operators utilize periodic inspections for condition assessment, based on empirical and subjective measures. Such inspections are generally expensive and require intrusive, unscheduled downtime. An additional drawback is that the condition assessment is only made in a periodic manner and WT condition between checks remains unknown. With the help of CM and fault diagnostic techniques, PM and condition-based maintenance (CBM) have become increasingly adopted. Most WT sub-systems fail during operation, as shown in Fig. 2.3 and Fig. 2.4, including rotors and blades, hydraulic systems, gearboxes, yaw systems, generators, brakes, electrical systems and electrical controls. Today, most WTs are now manufactured with some form of integrated CMS, sometimes interfaced to the operator via a Supervisory Control Alarm and Data Acquisition (SCADA) System. In figure below the results of having no proper pitch or gearbox CMS can be seen for the WT. When the gearbox fails, the rotor may still continue to run and all the power generated by the rotor is transferred to heat, the result of which can be a fire which destroys not only the gearbox but the whole turbine.

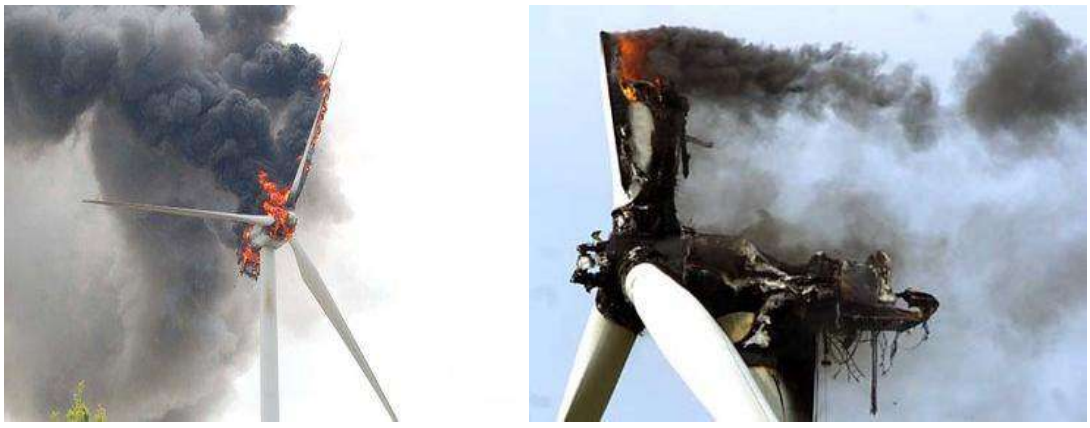

Fig. 2.8: Disastrous WT fires in Texas due to pitch or gearbox sub-assembly unreliability [41]

2.2.1 Monitoring WT Structure

2.2.1.1 Introduction

As the wind industry develops turbine CM techniques can improve to allow effective WT operation, safety, control and reporting. For a modern WT, a various CMSs are involved and integrated together for the monitoring to meet the needs of WT operators and owners. These systems are summarized in Fig. 2.9.

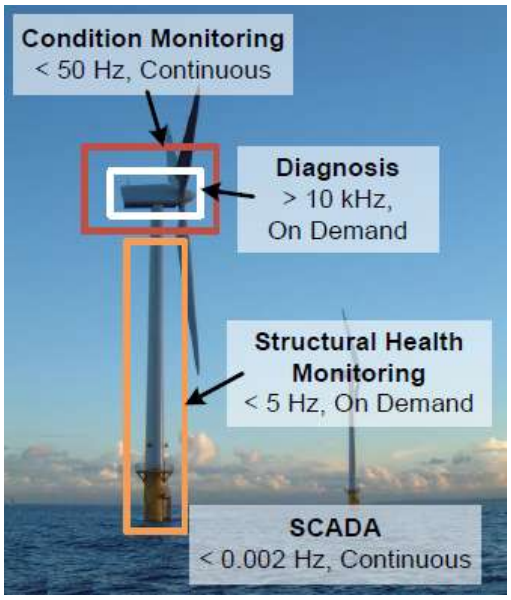

Fig. 2.9: Structure of WT monitoring [37]

2.2.1.2 Supervisory Control Alarm & Data Acquisition System

The SCADA system provides low time resolution monitoring to supervise the operation of the WT and gives online data to their operational base about the function and alarms of remote WTs. These data usually sample, at 10 minutes intervals, valuable signals, such as wind speed, output power and gearbox lubrication oil temperature [37], with ability to record and transmit maximum, mean, minimum and standard deviation of the signals. The data is also used by the WT OEM or the operator to generate graphical information to manage WTs during their warranty and optimise the operation and plan the maintenance as shown in Fig. 2.10. Moreover, with SCADA data the WT OEM is able to compare different wind farms performance and that of individual WTs against the whole populations of that type. However, SCADA systems also generate a huge amount of data that could reach 96MB per day for offshore farms with 100 WTs [29] which requires

careful organisation and considerable analysis for online interpretation. On the other hand, the low SCADA data rate does not allow the in-depth analysis usually associated with accurate diagnosis from CMS.

Fig. 2.10: Analysing WT SCADA data

In general, SCADA is a valuable low cost monitoring system with cheap high volume measurements, information and communication technology. The cost of SCADA depends on the wind farm size, number of units and design but typically can be between £5,000-10,000/WT [29]. Today, there is a wide variety of commercial SCADA systems available to the wind industry with ability to analyse time data using different analysis techniques.

2.2.1.3 Structural Health Monitoring System

A Structural health monitoring (SHM) system is for detecting deterioration of WT tower, structure and foundations before they can propagate to cause catastrophic damage to the turbine integrity [37]. The SHM signal is generally collected at low sampling frequencies below 5Hz [29]. This information could be used in a CBM program to minimize the time needed for component inspections, prevent unnecessary component replacements, reduce WT life-cycle costs and reduce the CoE. Another benefit of SHM is that it may allow to the use of lighter blades that would provide higher performance with less conservative margins of safety [42]. With lighter blades the WT can respond more rapidly to wind variations and so capture more energy[43]. The SHM is also a useful detection method for tackling the fatigue issue, because predicting the precise life of WT structural component is extremely difficult due to their long design life of 10–30 years [44]. In addition, it is difficult to ascertain the extent of fatigue damage that might have

occurred in a component, such as the blade or the tower. Thus, a SHM system is needed to continuously monitor the condition of the turbine system and warn of possible failure.

2.2.1.4 Condition Monitoring Systems

CMS for WT was considered important in the 1990s because of a history of costly drive train failures, primarily in gearboxes, and remains an important attribute for WTs, where the faults can be detected and identified at an early stage so that consequential damage can be mitigated. This technology was adopted initially from traditional rotating machine vibration CM experience and introduced to WT in 1990s [29]. However, the unique nature of the wind environment and the large modern WTs operating at continuously and rapidly changing power places constraints on WT CMS, as these conditions are not common in traditional rotating machines. This has encouraged the development of a monitoring technology suited to WTs based on their size, design and the location, employing not only vibration analysis, but also other diagnosis methods such as oil debris, acoustic , strain and electrical analyses. In general, CMS has proven successful for the detection of incipient faults in onshore WTs and is now installed as standard in most WTs≥1.5 MW. Furthermore, CMS is being fitted to almost all offshore WTs because of the importance in that environment of avoiding unexpected failures and the consequential downtime, damage and costs.

Based on the reliability data, the main WT sub-assemblies which may require CM and diagnosis are illustrated in Fig. 2.11. Among these three areas, the monitoring of the drive train is considered the most effective area due to the high failure potential in this sub-system. Once a failure is detected by CMS, an immediate alarm signal will be sent from CMS to the SCADA. Then, the exact nature and location of the failure can be determined by a monitoring engineering or automatically through a diagnosis system. It is essential for WT operators that this alarm signal is reliable, to enable them to take confident action with regards to maintenance. In fact, the operator's main interest is to know reliably the CMS alarm fault severity rather than to detect the exact fault nature [29]. Therefore, CM information does not require high sampling frequencies as this will reduce bandwidth and space for data transmission and storage.

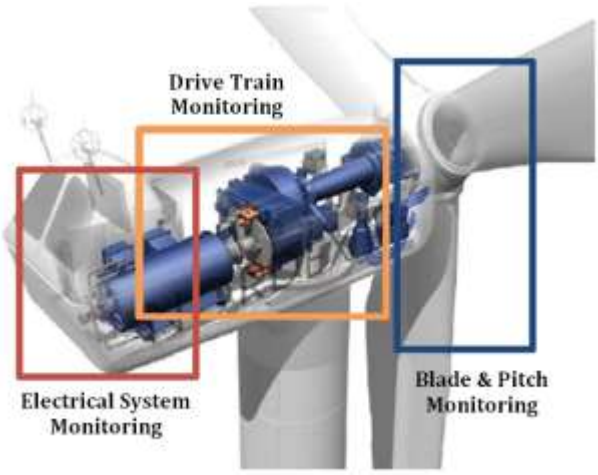

Fig. 2.11: Layout of main areas for WT condition monitoring within the nacelle

Due to the importance of CMS for wind industry, a number of different CMSs have been introduced to the WTs during the last two decades. Based on which main sub-assembly need to be monitored, these systems could use one parameter or multi-parameter monitoring, and also could use one monitoring technology or combine two, such as vibration and oil debris analysis. A summary of available and popular CMSs for WTs can be found in [45]. A typical CMS cost depends upon the system type as well as the turbine size and type but is approximately £7,000 for a mid-range WT CMS and other £7000 to retrofit to an existing WT [29], making it more expensive than SCADA. These costs will fall if the CMS were fitted by the OEM into a large number of WTs.

2.2.2 WT Induction Generator & Converter Fault Detection Literature

2.2.2.1 Introduction

As shown in Fig. 2.5, the WT generators are subject to incipient faults which decrease WT reliability and increase the O&M costs. To avoid all these, the generator should be monitored with advanced CMS during continuous operation. Therefore, there has been an increased interest in recent years in WT generator fault detection and diagnosis. However, as the wind technology has developed in the modern WT and the generator became part of a more complex control structure with a converter. Therefore attention is needed to focus on generator and converter monitoring through their control loop signals. Research on the CM via electrical machine control loop signals has previously focused on the variable speed IM. It has been recognized that techniques usually used for the diagnosis of faults in line-fed, open-loop machines may not be useful

when the machine is controlled, because the control action alters the response of voltages and currents to faults. However, a few papers have been published using control loop signals for monitoring and identifying closed-loop controlled WT generator faults. This section reviews some of these research in induction machine monitoring and fault diagnosis, with special focus on using the machine control loop signals.

2.2.2.2 Conventional Induction Machines

For over the last 20 to 30 years, intensive research has been published in the detection of IM failures. Work including [46], [47] and [48] focussed on the characteristics of rotor bar and end-ring failures in squirrel cage induction motors (SCIM) and the motor current signature analysis (MCSA)[47], [48]. The work also expanded into the detection of other induction motor faults using MCSA, including the stator winding shorted turn [47], stator asymmetrical fault [49], air-gap eccentricity [50], mixed eccentricity [51] and mechanical unbalance [52]. Although stator current monitoring has proved successful, reliable spectral interpretation is difficult, since distortions of the current waveform caused by the drive system abnormalities are usually present and disrupt the detection of fault frequencies. Therefore, it has been suggested that monitoring the instantaneous power signal may be an alternative to MCSA for detection of drive system mechanical abnormalities [53]. The instantaneous power was proven to be a suitable for IM fault detection in [48] where rotor breakage was successfully detected and quantified in a 1.5kW SCIM. Also, other monitoring techniques based on a stator frame vibration have been reported by [50], the stray flux [54], or the electromagnetic torque [55] for machine fault detection. These techniques are usually concerned with monitoring the open loop machines.

As for controlled machines, these techniques may not be effective, as the control itself modifies the behaviour of supply variables and may mask fault information. Therefore, the behaviour of other variables should be investigated and more sophisticated procedures adopted to find new indexes suitable for machine condition assessment. With the aim of extending the diagnostic procedures developed for open-loop faulted machines to the closed-loop operations, Bellini et al. have stated in [56] a systematic analysis of the behaviour of controlled SCIM (1.5kW, 400volt, 50Hz, 4 poles) with stator or rotor faults. The authors used field and torque control currents (i_d,i_q), terminal voltages and currents to diagnose stator and rotor asymmetries of a SCIM. Later, this work has been expanded in [57] to detect and identify SCIM stator winding shorts

and rotor bar breaks. A field-oriented controller (FOC) was implemented to control the machine. Simulation and experiments showed that typical spectral lines produced in the machine asymmetrical input current were present in the voltage as well as the current spectra. The amplitude of these lines depended on the control structure and its parameters; therefore conventional line current diagnostic indexes, e.g. from MCSA, could be ineffective on a controlled IM. However, it was observed that the i_d was independent of the control parameters and highly dependent on the degree of stator or rotor faults. So, the field control current can be used as an effective diagnostic index when an FOC scheme is adopted. On the other hand, the orthogonal component of i_q depended on control gain, load and frequency.

E. Serna, et al. [58] developed a new on-line method to diagnose rotor faults in time domain in IMs controlled by a rotor flux oriented control scheme based on the measured control currents and machine speed. A comprehensive analysis of the rotor fault mechanism in the drive was then described. The effect of a broken rotor bar on the control loop and terminal variables of an IM were evaluated through simulation and experiment (2.2kW, 230/400volt, 50Hz, 4pole SCIM), including the effect of varying the rotor resistance, inertia, load and speed on the magnitude of fault detected. The flux was determined from the stator currents and rotor angular position. From the results, the i_q proved to be the best rotor fault indicator, particularly in terms of sensitivity under incipient faults. The fault component amplitude in i_q depended only on the load level, remaining invariable to changes in speed and inertia. Further analysis was conducted by the authors in [59], mainly focused on limitations of this algorithm for detecting rotor faults. This study showed that speed loop faults could be attenuated in drives of very large inertia. However, the effect in the current loop could not be completely eliminated by the controller although it was reduced, especially in the low frequency range. For the resolution of the measured rotor angular position, that reduction did not modify the amplitude in the measured i_q of the characteristic fault harmonic and the proposed technique performed well online.

Using the d- and q-current error signals, current controller outputs and the estimated rotor flux, Cruze et al. [60] presented a study on the diagnosis of broken rotor bar faults in a SCIM. The aim of study was to identify rotor faults in drives using the following classic-structure controls:

- Indirect rotor field-oriented control (IRFOC);
- Indirect rotor field-oriented control with flux control (IRFOC-FC).

The ability of three different diagnostic approaches was investigated through an IM simulation (15kW, 690volt, 50Hz, 4-pole SCIM). From the IRFOC simulations the authors concluded that all techniques are capable of detecting the fault with the presence of time varying loads, but only the estimated rotor flux amplitude was robust against the drive speed reference variations. When dealing with IRFOC-FC drive, the q-axis rotor flux component, the d-axis error signal and the d-axis current controller output contained proved useful diagnostic fault indicators

Another attempt was presented by Concari et al. [61] to diagnose and assess the severity of broken rotor bar faults in a closed loop SCIM controlled with FOC architecture, with or without a speed loop. The robustness of the diagnostic procedure, based on spectral analysis of electric quantities, versus control regulator parameters and motor load were validated. The study reported that on a 1.5kW, 400volt, 50Hz, 4-pole SCIM, the fault component in i_d is independent of the speed control and seems attractive for fault detection. More recently, this research was developed to include SCIM controlled by direct torque control (DTC) in [62]. Both current and voltage sidebands could be used to detect the fault presence but as in the case of FOC the fault severity could not be assessed. The authors concluded that a diagnostic index based on the amplitude of the current components produced by high frequency voltages injection provides better results. This index was not affected by the control scheme or parameters, and allowed the detection of the fault presence and its severity with a good approximation, even at light load conditions.

2.2.2.3 Doubly-Fed Induction Machines

Djurovic et al. [63] have investigated the effect of unbalanced rotor windings on the stator line current and total instantaneous power signals spectra of WT-WRIGs and DFIGs, a development of MCSA techniques but backed up by theoretical simulation and experimental proof. The analysis was performed first for steady state, constant speed test operation and second for transient, variable speed conditions such as encountered in a WT. Measured data was collected from two WRIG Test Rigs where one of them operates as either a WRIG or DFIG, commonly used in WTs, and the other runs as WRIG at constant or variable speed conditions (30kW, 380volt, 50Hz, 4-pole WRIG or DFIG). A fault frequency tracking algorithm and a set of concise analytic expressions was developed to allow this fault to be detected reliably under variable speed conditions. The results show that both stator and total power spectra are valid for fault detection. The authors stated

the stator current spectrum has lower noise but the total power spectrum has lower fault frequencies.

An experimental investigation into DFIG fault detection using MCSA was presented by Popa et al. [64]. The machine was controlled through two back to back pulse-width modulated (PWM) converters (11kW, 690volt, 50Hz, 4-pole DFIG). The experimental results clearly demonstrated that MCSA could diagnose turn-to-turn faults and other DFIG problems, such as stator or rotor phase inductive or resistive unbalance, with a controlled machine. However, these methods were based upon experimental results alone, without a complete theoretical basis and failed to provide reliable detection when the DFIG operated under imbalanced-load conditions, the work also did not consider the effect on fault detection of the control system.

Another new technique for detecting stator inter-turn faults in a WT-DFIG, operating under imbalanced-load conditions, based on rotor current and search-coil voltage analysis was suggested by Shah et al. [65]. This machine was controlled by a Static Kramer converter system (2kW, 208volt, 60Hz, 4-pole DFIG). Various frequency components induced in the rotor circuit due to stator inter-turn faults were investigated. Simulation and experimental results illustrated the influence of machine load and slip on the fault results. By monitoring a rotor phase current component, the rotor-current vector and a rotor search-coil voltage, a definite stator winding inter-turn fault indication can be obtained, even for few winding turns. Moreover, the sensitivity of all three fault detection signals were examined, depending on the signal to noise ratio. Both the rotor–current vector and rotor search-coil voltage provided the best fault detection with a higher SNR than the rotor-phase-current. A prototype CMS digital-signal-processor measuring the search-coil voltage has been constructed to demonstrate the capability of timely on-line stator inter-turn fault detection. Despite the method having rapid detection, in approximately 2sec even during speed transients, the use of search coil voltage must be considered invasive since it would require an extra winding on the rotor. Moreover, slip-rings and brush-gear were required to acquire the detection signal.

However, understanding the influence of WT-IG failures on different generator control variables and using these signals for monitoring the WT-IGs has received little research attention and few papers have been published in this field. Yazidi et al. presented a simulation study in [66] to identify the best diagnostic procedure for DFIG unbalanced phase fault detection. The results confirmed that the rotor unbalance can be detected in the control system rotor voltages which are unbalanced if DFIG is current-

controlled. In case of stator unbalance, the stator currents are unbalanced while the rotor quantities contain ripple. Based on these results, Casadei et al. [67] expanded the work experimentally. It was confirmed that the current signature technique can be used, but a more interesting technique would be to use the rotor-modulating-signal spectral components. More recently, the effectiveness and sensitivity of rotor-modulating-signal spectra as a new and reliable diagnostic index in respect to different rotor or stator fault severity have been evaluated in [68] and to the variation of the bandwidth of the current loop in [69]. In contrast, in previous work, only simulation study was presented in [66] as well as only steady state machine operation was considered in [67], [68] and [69] and this is not the operating condition for WT generators.

2.2.2.4 Converter

Closed-loop IM monitoring has also attracted researchers focusing on improving converter reliability, which is of major importance in industrial, commercial, aerospace and military applications as well as the wind industry. A knowledge of converter system fault modes would be extremely useful from the standpoint of improving system design, protection and fault tolerant control and a review of converter reliability was done by Yang et al [70].

There have been a number of researches into closed-loop IM converter fault diagnostic methods, for example Kastha et al. [71] investigated the effect and diagnosis of different faults modes of a voltage-fed PWM inverter system for IM drives using open-loop speed control. After identifying the important fault types, a preliminary mathematical analysis was made for four selected fault types, namely input single phase ground fault, rectifier diode short circuit, inverter transistor base open-circuit and inverter transistor short-circuit. A simulation study was made to validate the analytical study using phase currents, torque, speed and DC link voltage used to determine power circuit component stresses and to evaluate satisfactory post-fault steady-state operating capability. The results are also useful for easy fault diagnosis and improving protection system design.

2.2.2.5 Conclusions

The CM and fault diagnostic research presented can be summarized using Table 2.2 as follows:

- Early CM work on IMs concentrated on MCSA but this has been demonstrated to be less reliable when applied to closed-loop controlled variable speed IMs;
- Previous research clearly demonstrates the potential for using control loop signals for monitoring and diagnosing IM faults;
- However, there have been few published papers using WT DFIGs with closed loop generator control, rotor-modulating-signals;
- Some work has been done to understand converters faults but there appear to have been no papers published on monitoring the converter of a closed loop IM using control loop signals;
- None of the previous work has been done on a DFIG with closed loop control under realistic varying wind speed conditions, as encountered in a real WT DFIG.

Table 2.2: Summary of induction machines investigated using machine control loop signals in the literature

Authors	Reference	Signal Analysis	Power (kW)	Voltage (volt)	Frequency (Hz)	Poles	Machine
A. Bellini et al.	[56] and [57]	FFT	1.5	400	50	4	SCIM
E. Serna et al.	[58] and [59]	Time domain	2.2	230/400	50	4	SCIM
S. M. A. Cruz et al.	[60]	Time domain Frequency domain	15	690	50	4	SCIM
C. Concari et al.	[61] and [62]	FFT	1.5	400	50	4	SCIM
A. Yazidi et al.	[66]	FFT	4	380	50	4	WT-DFIG
D. Casadei et al.	[67]	FFT	3.3	380	50	2	WT-DFIG
	[69]	FFT	5.5	380	50	4	
A. Stefani et al.	[68]	FFT	3.3	380	50	2	WT-DFIG

3 Physical & Simulated Test Rig

3.1 Physical Test Rig

3.1.1 History of the Test Rig

A Test Rig was established at Durham University in 2003 to experimentally represent a real WT drive train and investigate the various failure modes in order to develop an appropriate CMS. This Test Rig has the advantage of providing a more accessible, reliable, controllable and economical test facility than a full-scale WT, where the faults can be applied on demand and additional instruments can be used without the need for WT site access. Conversely in an operational WT site, researchers cannot control fault and failure conditions and have to wait for a fault to occur to investigate hypotheses. However, real WT fault features are more complex than those which can be applied on the Test Rig and an object of this research was to simplify those WT drive train faults and observe them on the Test Rig.

This Test Rig was initially built using funding from the National Renewable Energy Centre (NAREC) in Blyth, Northumberland, and then the instrumentation was developed by M. Wilkinson as part of his research in [72]. It consisted of variable speed drive and DC motor (54kW), which represent the WT blades and hub, controlled to emulate the torque-speed characterises of a WT. They are controlled by a man machine interface (MMI) incorporating a LabVIEW control environment. The desired WT rotational speed for the Test Rig can be modelled in the PC controller for either real or simulated wind data. The DC motor creates the low speed input and then transfers to high speed shaft through a Brook Hansen gearbox (5:1 or 11:1). A large diameter rectified Permanent magnet synchronous generator (PMSG) and an IG were tested as WT generators. After that, significant improvements were made to the Test Rig by C. Crabtree in [37]. These included signals conditioning, to generate signals with acceptable noise levels, an accurate speed signal, essential for CM frequency tracking techniques, were developed in his work. Furthermore, development and installation of experimental balance planes for both the high and low speed shafts to allow mass imbalance experiments to be carried out.

During the last few years, the Test Rig has been used successfully to monitor experimentally a number of electrical and mechanical drive train faults [37], [72], [73]. Because they did not necessarily replicate precise WT faults, they have been called "fault-like perturbations" but contain similarities with faults on real WTs. These "fault-like perturbations" were applied to two different generator configurations as follows:

1. A 10kW PMSG which represented a direct-drive WT. The various "fault-like perturbations" applied to this Test Rig were:
   - Shorted stator coils, representing the WT generator winding faults;
   - Generator rotor unbalance, representing the effect of mechanical fault in the WT drive train.
2. A 30kW IG which represented a geared-drive WT. The "fault-like perturbations" applied to this Test Rig were:
   - Rotor electrical asymmetry, representing the effect of a rotor winding fault or brush imbalance in the WT generator;
   - High speed shaft mass unbalance, representing the effect of mechanical fault in the WT drive train;
   - High speed pinion tooth damage, which represent the gearbox failure in the WT drive train.

In the previous work, the IG was only used as WRIG, meaning that there was no control on the generator-side and the whole generator part of the Test Rig was open loop, whilst the speed control of the Test Rig was closed loop. Therefore, the work has been extended by the author, during this research, to close the generator control loop. The work included:

- Installation of a back-to-back converter between the grid and the rotor side of the generator;
- Installation of an xPC TargetBox as an interface between the PC controller and the generator;
- Installation of new voltage and current cards;
- Installation of incremental encoder on the generator rotor;
- Designing and building a controller for RSI based on vector control strategy.

This work has been an important development of the Test Rig to represent a fully variable speed WT-driven DFIG. These developments will be described in more detail in this chapter. Moreover, due to the limitation in the torque at the generator side, because of the gearbox ratio and its effect on the generated power when the speed varies from

±30% around the synchronous speed, the author made additional modifications to the Test Rig. This work initially included the back-to-back converter having 48volt DC batteries as the DC link voltage. In this configuration, only the RSI was used. The peak stator phase voltage was reduced to 110volt as compared with the generator rating of 326volt, with the RSI operating at a modulation index of 0.7 at total rotor phase resistance 0.235Ω, to avoid problems with overmodulation and increase the system protection.

Finally, the Test Rig was modified to work at normal DC Link voltage, 550-600volt, by removing the gearbox and using the whole back-to-back converter to run over the whole range of speed. However, due to the small value of the modulation index of the RSI as well as the limitations of the xPC TargetBox hardware in synchronizing the generated phase PWM signals, which resulting in increasing the switching harmonics and producing high distortion in the control and generator variables, this configuration has not been used in this research for CM purposes. Therefore, only the Test Rig configuration using 48volt DC batteries and the RSI has been used in this research with the reduced stator voltage as compared to the generator and converter rating to provide lower distortion and increase the system protection. Currently, the Test Rig has been reconfigured to run as a variable speed WT-driven WRIG or DFIG depending on the user. The previous and current schematic diagrams of the WT drive train Test Rig are demonstrated in Fig. 3.1.

The torque-speed characteristic for the IG in both WRIG and DFIG configurations is shown in Fig. 3.2. Data was collected using a Magtrol 3410 Torque Display to give the shaft speed and torque. The graphs are plotted for the generator being driven up to the limit of the driving DC machine armature current of 131amp in case of the WRIG while it was driven using the RSI controller up to the limit of the DFIG maximum speed and DC battery currents. In previous research by M. Wilkinson and C. Crabtree, the generator did not allow for such a large torque range as the generator was driven using a 5:1 gearbox for which the DC motor delivered torque at a lower speed and the armature current limit was reached at lower generator torque. Currently, the generator is driven without a 5:1 gearbox and higher speed and torque range can be achieved.

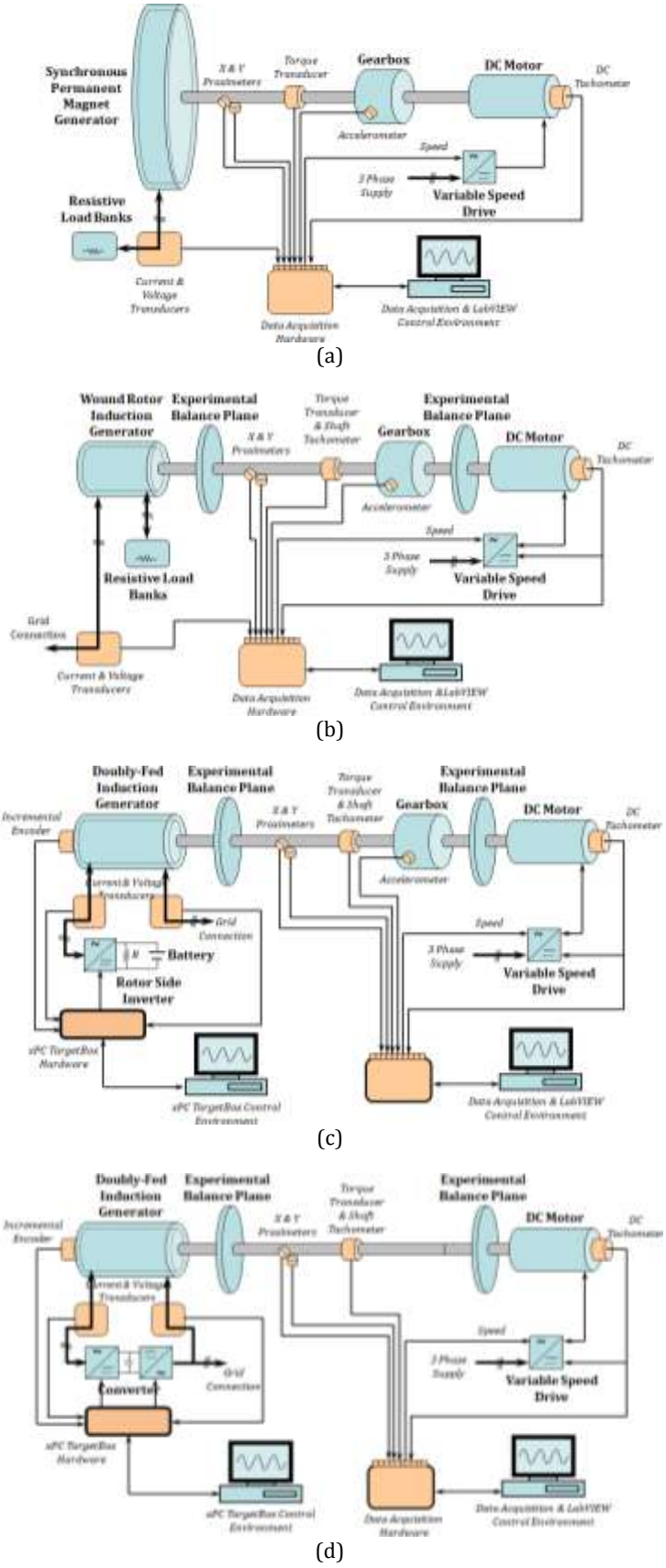

Fig. 3.1: Previous & current schematic diagrams of the WT drive train Test Rig
(a) with PMSG installed (b) with WRIG installed
(c) with DFIG closed loop generator control using a 48V battery DC Link & RSI
(d) with DFIG closed loop generator control & full converter

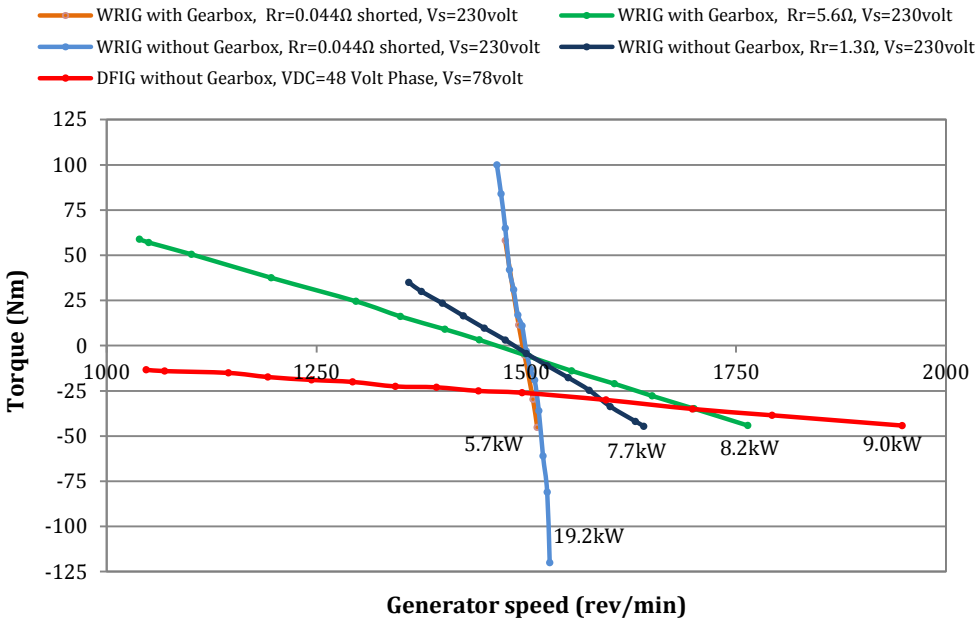

Fig. 3.2: 30kW generator torque-speed characteristics showing power output limits

3.1.2 Details of the Test Rig

As mentioned above, the Test Rig, as shown in Fig. 3.3, had already been developed to represent the power electronic drive train. It consists of a number of mechanical and electrical components, controllers and instrumentations, which are described here to give a complete view of the drive train configuration.

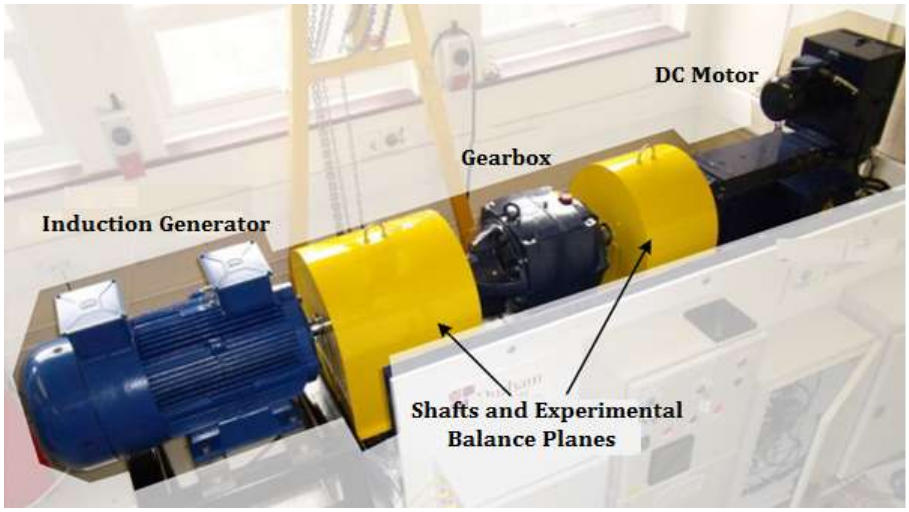

Fig. 3.3: Photograph of physical WT drive train Test Rig

3.1.2.1 Electrical & Mechanical Components

3.1.2.1.1 DC Motor

A Brook Crompton, separately excited DC machine rated about 54kW at 2120 rev/min, with mass 87kg.

3.1.2.1.2 DC Converter

A Eurotherm 590+ variable speed drive, with the capability of torque or speed control. For the work described here it was controlled with a torque feedback loop.

3.1.2.1.3 Gearbox

A Brook Hansen, two-stage helical gears parallel shaft gearbox. The first stage teeth 66/13 and second stage 57/58 provides overall gear ratio 4.9894:1 between input and output shafts, referred to as 5:1 for simplicity.

3.1.2.1.4 Generator

A Marelli Motori, WRIG, 4 poles machine, rated at 30kW, 380volt or 230volt, 50Hz and mass 95kg.

3.1.2.1.5 Back-to-Back Converter

ALSPA MV3000 frequency converter using two bi-directional inverters separated by a DC link voltage (capacitor). The GSI is a MV3071J5A1 AEM, 380-480volt, 30/37kW and the RSI is MV3058A4A1 BDM with 380-440volt, 22/30kW. The converter was manufactured by Converteam Ltd for use in marine and offshore applications. As a part of this research, the converter was refitted into a separate new cabinet, as illustrated in Fig. 3.4, to improve operator safety also; the cabinet was designed with other advantages including:

- Easy to use and move the converter;
- Ability to use the whole converter or just the RSI depending on the test;
- Ability to change the DC link voltage value from 550volt to 600volt through control board located in the cabinet's door;
- Ability to supply the stator from the grid and control the stator voltage value through a variac. The variac can be connected to the cabinet and removed simply between two plugs in the cabinet's side.

Fig. 3.4: Photographs of back-to-back converter cabinet

3.1.2.1.6 Experimental Balance Planes

Two balanced metal disks, a radius of 250mm and holes at 60° intervals and four pitch circle diameters, have been fitted to the Test Rig for mass unbalance faults to be simulated. One is located on the high speed shaft towards the generator drive end bearing and the other on the low speed shaft between the gearbox coupling and DC motor.

3.1.2.2 Instrumentation & Conditioning

The original Test Rig instrumentation, described in [37], was deemed suitable for use in this research however a further work was undertaken as part of this research to fit extra instrumentation to the Test Rig to be developed from open loop Test Rig (WRIG) into closed loop Test Rig (DFIG). This work, coordinated by the author, aimed to install a new current and voltage cards, incremental encoder and xPC TargetBox to achieve the control of the DFIG. In order to minimize experimental noise from the laboratory environment and improve the safety for the operator, all instrumentation is isolated from mains voltage electrical signals and power supplies by steel cabinets. After the new installation, the whole Test Rig became instrumented with a DC tachometer, torque transducer and pulse tachometer, accelerometer, displacement transducers, voltage and current cards, incremental encoder, xPC TargetBox and data acquisition. These various instrumentation components are illustrated in Fig. 3.5 and they are described briefly in this section.

3.1.2.2.1 DC Tachometer

Supplied by Radio-Energie and located at the end of the DC motor to give a low speed shaft speed reading (Fig. 3.5a). The output DC voltage was directly proportional to the speed, with an output of 0.06volt per revolution. The DC tachometer signal contains high frequency commutator noise which was removed by using a 20Hz low pass filter (LPF) [37].

3.1.2.2.2 Torque Transducer & Pulse Tachometer

As shown in Fig. 3.5b, a Magtrol 313/431 torque transducer was fitted between the generator and the gearbox and has a rated torque of 500Nm and sensitivity of 10^{-2}volt/Nm. It measures the high speed shaft torque directly. This transducer also could be used as a tachometer for speed measurements with 60 pulses per revolution. Both torque and speed signals can be combined together to give a measure of the power in the shaft.

(a) (b)

(c) (d)

(e) (f)

(g)

Fig. 3.5: Various instrumentation components:
(a) DC tachometer (b) torque transducer & pulse tachometer (c) displacement transducers (d) accelerometer (e) incremental encoder (f) xPC TargetBox (g) current & voltage cards

3.1.2.2.3 Displacement Transducers (X & Y Proximeters)

Two sensors, Fig. 3.5c, positioned at 90^o to each other on the high speed shaft to measure the Shaft displacement on the horizontal and vertical axes. Displacement transducers are suitable for measuring low frequency vibrations that would otherwise require a large mass accelerometer.

3.1.2.2.4 Accelerometers

The gearbox is instrumented with two Bruel and Kjaer accelerometers measuring the vibration relating to tooth faults and gearbox conditions as shown in Fig. 3.5d. These accelerometers can be placed on the generator as well.

3.1.2.2.5 Incremental Encoder

Fig. 3.5e shows a Sick-Stegmann DSR61 encoder fitted to the generator end to give the actual generator rotor position needed for control purpose. The encoder has a maximum angular acceleration 5×10^5rad/sec^2 and output up to 8192 line per revolution. Fig. 3.6 shows the measured signal for the rotor position. This signal is also utilised to obtain generator rotor speed by differentiation of the encoder signal. The observation and spectral analysis of the calculated speed signal gave rise to concern that large spikes were seen on the signal. These spikes were the result of differentiation of the noise of the encoder signal. As a result of this, a rate limiter and LPF with cut-off frequency 20Hz as shown in Fig. 3.7a, have been used. Fig. 3.7b illustrates the generator rotor speed signal before and after conditioning. It is clear that from the figure that the conditioned signal is much improved.

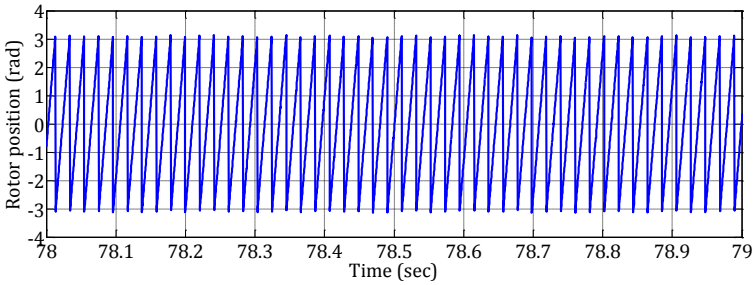

Fig. 3.6: Measured rotor position signal

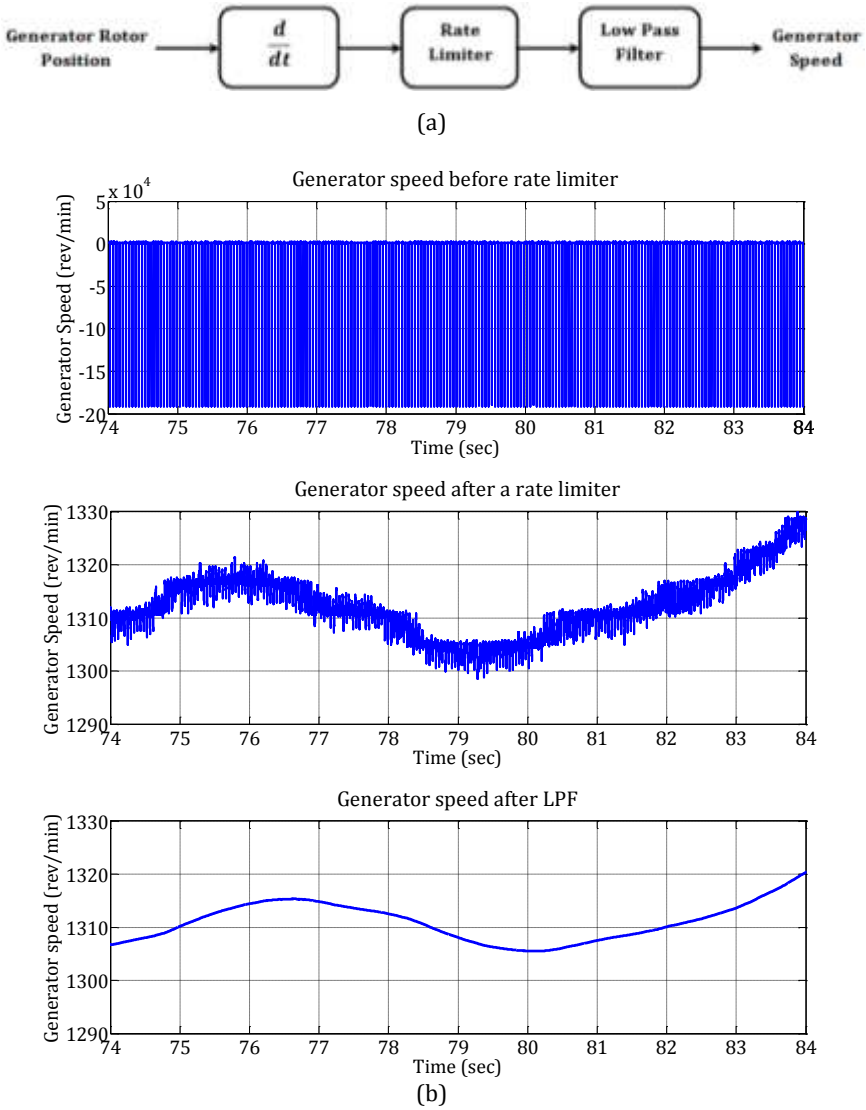

Fig. 3.7: Block diagram & resulted signals of generator speed improvement

3.1.2.2.6 xPC TargetBox

This is a powerful tool for rapidly implementing real-time control systems on a digital computer. In this research, it has been used to implement the RSI controller. A block diagram representing this control model was created on a desktop PC as a host in MATLAB Simulink. Then, when the operator is ready to run the controller, the model can be simply compiled to an executable file and then loaded onto xPC TargetBox. However, once the executable program has been uploaded from the host PC to the TargetBox, the TargetBox is essentially autonomous and need not even be connected to the host computer to run the controller.

The xPC TargetBox (Fig. 3.5f) is a small PC-compatible computer equipped with hardware for receiving and outputting both analog and digital voltages and for receiving

signals from incremental encoders. Through its I/O hardware, the TargetBox will interact with the Test Rig. During this research, the TargetBox was configured by the author to read 10 sensor signals through its input, namely stator and rotor phase currents, stator line voltages and mechanical rotor position and then output 3 control (PWM) signals for switching insulated-gate bipolar transistors (IGBT's) in the RSI. Additionally, the TargetBox can send data of the input signals, output signals and other calculated signal inside the controller back to the host PC after the controller execution has terminated. Fig. 3.8 shows the Target hardware block diagram for controlling the Test Rig.

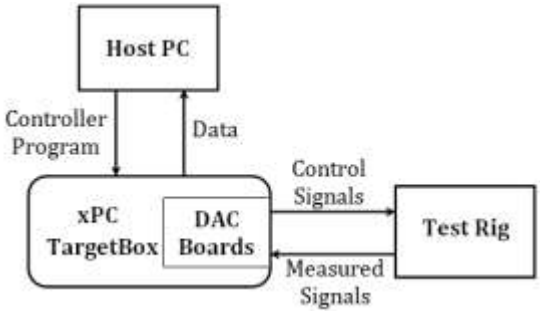

Fig. 3.8: xPC Target hardware configuration for controlling the Test Rig

Moreover, the xPC Target environment were configurable to run at sampling frequency 5kHz and record the data for the following signals:

- Time;
- Generator rotor position and speed;
- Generator torque reference;
- Stator and rotor phase currents;
- Stator phase voltages;
- Actual and reference *d*- and *q*-rotor currents;
- Error signals of *d*- and *q*-rotor currents;
- Total stator active and reactive powers;
- Outputs of current Controllers.

3.1.2.2.7 Current & Voltage Cards

Three boards with three transducers each were installed to measure the generator's terminals and they produced a voltage proportional to measured values as demonstrated in Fig. 3.5g. Two boards to measure the stator and rotor currents while one board for the stator voltages. The voltage transducer (VT) and current transducer (CT)

boards can be seen in the side of back-to-back converter cabinet. Three channels were available on each board and instantaneous values of the phase currents and line voltages were available to enable the measurement of the electrical signals for controlling the DFIG. To reduce noise and improve the quality of the signals, coaxial cables have been used to transfer the measurements from the cards to the xPC TargetBox.

3.1.2.2.8 Data Acquisition Cards

Two National Instruments 6015 data acquisition (DAQ) cards were used in the system. These cards allow up to 32 analogue inputs and 4 analogue outputs to be interfaced with a NI LabVIEW control environment of the Test Rig. The cards each contained one A/D converter, so the signals were multiplexed, with the maximum sample rate for each channel depending on how many channels were in use. In this research, the DAQ pads sample 500ms of data from each channel at 5kHz before transmitting via USB to the data acquisition environment where they can be saved immediately into files. Moreover, the DAQ pads were configured to read 14 data channels during running the Test Rig as listed below:

- DC motor speed and armature current;
- High speed shaft torque and speed;
- Three stator line currents;
- Three stator phase voltages;
- Vertical & horizontal displacement vibration;
- Two accelerometers.

3.1.2.3 Control

In previous research [37] and [72], the Test Rig was only controlled from the LabVIEW environment to drive the Eurotherm DC motor variable speed drive. With the development the Test Rig and closing of the generator loop, a new control was designed by the author and implemented to the system using the xPC Target environment. This is the RSI controller used to control the generator torque through the rotor current. With a combination of the LabVIEW and xPC Target environments, the Test Rig can be run as variable speed WT-DFIG. These environments allow the operator to run the generator to its synchronous speed before waiting for confirmation of grid connection with back-to-back connection and the RSI controller running. Once the operator confirms grid synchronisation the generator can run up or down from the test starting speed at whatever point the data acquisition requires.

The driving speed is read from a spreadsheet containing a time and speed vector defined by the operator. The LabVIEW environment then transmits a control signal, proportional to speed demand, to Eurotherm DC variable speed drive in real time. During the test, the xPC Target environment reads its measured signals from the Test Rig, and then generates control signals and sends them back to the RSI.

The Test Rig can be operated either at constant or variable speed depending on the operator's requirements. While a number of different constant speed and variable speed driving conditions were available, the operator can generate a new demand speed with different conditions. This can be using a Microsoft Office Excel and implement easily in the LabVIEW.

3.2 Mathematical Model of Test Rig

3.2.1 Development of the Mathematical Model

During the last few years, several researchers have been involved in the development of a mathematical model to describe the dynamic behaviour of the Test Rig with WRIG configuration. Initial work was carried out by an MSc student H. Wen-Ko in 2008 [74] to model and examine the Test Rig drive-train response based on a 3-degree-of-freedom torsional system. The model comprised an inertia representing the DC motor, connected with a torsionally elastic and damped shaft to an inertia representing the gearbox, which again was connected with a torsionally elastic and damped shaft to an inertia representing the generator. The inertia values were calculated based on shape and material while the other parameter values were calculated by analysing the dynamic response data to different input steps. Although Wen-Ko's work had some success providing an approximation of the Test Rig behaviour, there were some major limitations to the model because parameters had been ignored in the model, which were found to have a significant influence on the Test Rig dynamic response, particularly the Eurotherm DC motor variable speed drive controller. The mathematical model produced was also not compared to the Test Rig's time domain behaviour. Therefore, it became necessary to develop a more complex model to represent the Test Rig behaviour more accurately.

The Test Rig model was developed further by MEng student J. Emslie in 2010 [75]. With the addition of the DC motor controller, the development improved the modelling of the gearbox to represent the non-linear behaviour of tooth stiffness, damping, backlash and gear geometric parameters. In particular, the model complexity was increased to 6-

degrees-of-freedom. Moreover, it was discovered during this study that some parameters from the earlier model were inaccurate, so further investigation was required. The work was also advanced by importing the model into MATLAB Simulink. Results obtained from this model show that reasonable time domain behaviour for both torque and speed was being achieved. Fig. 3.9 illustrates a comparison of model and test rig time domain torque responses as reported in [75]. However, the frequency response of the model is not fully matched to the Test Rig's spectrum. Although the model had been improved by increasing its complexity, it was still not detailed enough. For example, Eurotherm DC motor controller was represented by a simple speed controller, while in the physical Test Rig it contains both speed and current controllers. These would have little effect on the overall step response, but are expected to be significant in the frequency spectrum.

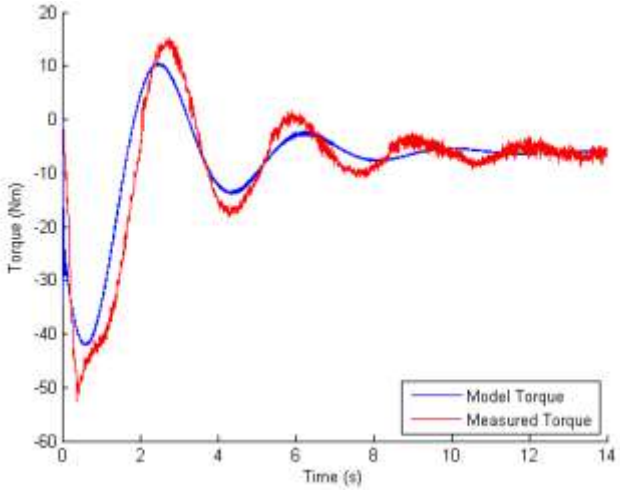

Fig. 3.9: Time domain torque response comparison [75]

Previous models described only the Test Rig mechanical components while electrical components were ignored. To effectively model the full dynamic behaviour of the Test Rig, further work was needed to represent the Test Rig more completely and accurately. Therefore, a new MATLAB Simulink model was developed by the author. This work focused on detailed modelling of all Test Rig components backed up by measurement of as many parameters as was required. The model comprises of:

- DC motor speed and current controller models;
- Electro-mechanical DC motor model;
- Low speed shaft model;
- Gearbox model;
- High speed shaft model;

- Electro-mechanical generator model;
- DC motor, gearbox and generator friction losses;
- DC motor and generator windage losses;
- Grid.

However, the model at this stage represented the Test Rig with WRIG configuration, which means that it cannot be able to be used in studying a CM for WT-driven DFIG. More recently, further work has been performed to develop this model by the author to represent the Test Rig with DFIG configuration. The development included closing the generator loop through a converter. This has been done with designing a generator torque controller for the converter and representing both of them in the model. To simplify the model and run it faster, the GSI and the DC link voltage in the back to back converter were ignored and replaced by DC voltage source. These simplifications are expected to have no effect on the overall response shape and the frequency spectrum. The developed model was used to obtain the simulated results which demonstrated in this thesis. The mathematical representations of the Rig components in the model are described in more details in the next section.

3.2.2 Details of the Mathematical Model

As mentioned above, the model had been updated to follow the changes in the physical Test Rig to represent WT-driven DIFG. In the same time, the physical Test Rig and the MATLAB model are still valid to represent open-loop Test Rig driven WRIG by disconnecting the RSI and its controller from the model as well as shorting the rotor circuit. However, the mathematical representation of the Test Rig can be divided into three fundamental models:

- DC motor and controller model used to create a torque into the system from step input voltage from the DC converter;
- Drive-train model, which represents the inertia of the DC motor, gearbox and generator, and also the damping, stiffness of gearbox and speed shafts, and friction and windage losses in case of the Test Rig configurations as demonstrated in Fig. 3.1b and 3.1c;
- Electrical model including the generator electrical part, RSI, DC link voltage, generator torque controller and grid.

3.2.2.1 DC Motor & Controller Model

This variable speed drive and DC Motor model comprised both speed and current control loops as described in Fig. 3.10.

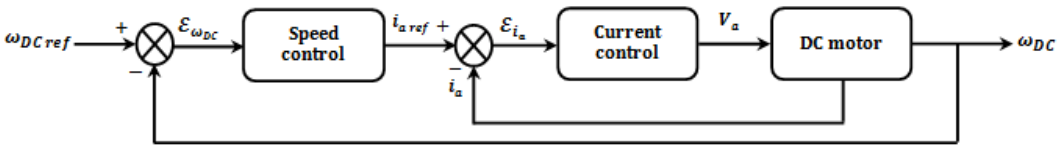

Fig. 3.10: DC motor & control loops

The Eurotherm controller manual indicated that the DC machine was operated by a PI controller for speed and current loops. The relationship between the speed error ($\mathcal{E}_{\omega_{DC}}$) and the reference armature current ($i_{a\,ref}$) of the speed control can be written as:

$$i_{a\,ref} = K_{ps}\mathcal{E}_{\omega_{DC}} - K_{is}\int_0^t \mathcal{E}_{\omega_{DC}}dt = K_{ps}(\mathcal{E}_{\omega_{DC}} - \frac{1}{T_{is}}\int_0^t \mathcal{E}_{\omega_{DC}}dt) \quad 3.1$$

and

$$\mathcal{E}_{\omega_{DC}} = \omega_{Dc\,ref} - \omega_{DC} \quad 3.2$$

In similar way, the armature voltage V_a is:

$$V_a = K_{pc}\mathcal{E}_{i_a} - K_{ic}\int_0^t \mathcal{E}_{i_a}dt = K_{pc}(\mathcal{E}_{i_a} - \frac{1}{T_{ic}}\int_0^t \mathcal{E}_{i_a}dt) \quad 3.3$$

and the armature current error is:

$$\mathcal{E}_{i_a} = i_{a\,ref} - i_a \quad 3.4$$

where ω_{ref} and ω_{DC} are the reference and actual angular speed of DC motor, K_{ps}, K_{pc}, K_{is} ,K_{ic}, T_{is} and T_{ic} are proportional gains, integral gains and integral time of the speed and current controls. These controllers can be modelled easily in MATLAB Simulink using Laplace operators. Then, the armature voltage supplies the armature circuit of the motor (armature inductance (L_a) and resistance (R_a)) as shown in Fig. 3.11, and generates the back electromotive force (V_{emf}).

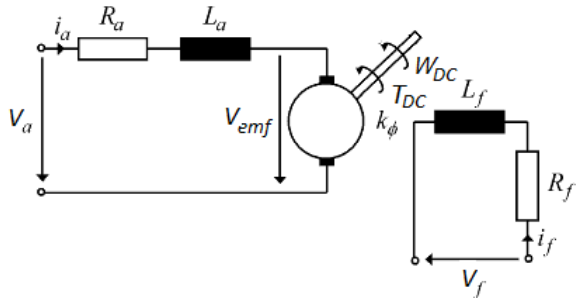

Fig. 3.11: Equivalent circuit of separately excited DC motor

The separately excited DC motor was characterized by the following mathematical model [76]:

$$V_a = V_{emf} + R_a i_a + L_a \frac{di_a}{dt} \quad 3.5$$

$$V_f = R_f i_f + L_f \frac{di_f}{dt} \quad 3.6$$

$$V_{emf} = K_{\emptyset} \omega_{DC} i_f \quad 3.7$$

$$T_{DC} = K_{\emptyset} i_a i_f \quad 3.8$$

where V_f is the field supply voltage, L_f and R_f are the field inductance and resistance, T_{DC} is the DC motor torque and $K_{\emptyset}$ is the motor constant.

3.2.2.2 Drive-Train Model

3.2.2.2.1 DC Motor Mechanical Model

The moment of inertia of DC motor and mass plate (J_{DCm}) dynamics is given by:

$$J_{DCm} \dot{\omega}_{DC} = T_{DC} - T_{ls} - K_{fDC} \omega_{DC} - K_{wDC} \omega_{DC}^2 \quad 3.9$$

T_{ls} is low speed shaft torque, K_{fDC} and K_{wDC} are the friction and windage loss coefficients of the DC motor.

3.2.2.2.2 Low Speed Shaft Model

The low speed shaft torque acts as breaking torque on the DC motor. The relationship between the speed (ω_{ls}) and the torque in this shaft can be written as:

$$T_{ls} = D_{ls}(\omega_{DC} - \omega_{ls}) + K_{ls}(\theta_{DC} - \theta_{ls}) \quad 3.10$$

where θ_{DC} and θ_{ls} are the angular displacement of the motor and shaft, D_{ls} and K_{ls} are damping and stiffness constants.

3.2.2.2.3 Gearbox Model

Fig. 3.12 displays the 4 wheel gearbox system and the interaction between each gear, respectively. The motion of these wheels is given by the following equations [75]:

$$J_{g1}\dot{\omega}_{g1} + r_{g1}D_{g1}(r_{g1}\omega_{g1} + r_{p1}\omega_{p1}) + r_{g1}K_{g1}x_1 = T_{ls} \tag{3.11}$$

$$\begin{aligned}(J_{p1} + J_{g2})\dot{\omega}_{p1} + r_{p1}D_{g1}(r_{g1}\omega_{g1} + r_{p1}\omega_{p1}) + r_{p1}K_{g1}x_1 \\ + r_{g2}D_{g2}(r_{g2}\omega_{g2} + r_{p2}\omega_{p2}) + r_{g2}K_{g2}x_2 = 0\end{aligned} \tag{3.12}$$

$$J_{p2}\dot{\omega}_{g2} + r_{p2}D_{g2}(r_{g2}\omega_{g2} + r_{p2}\omega_{p2}) + r_{p2}K_{g2}x_2 = T_{hs} \tag{3.13}$$

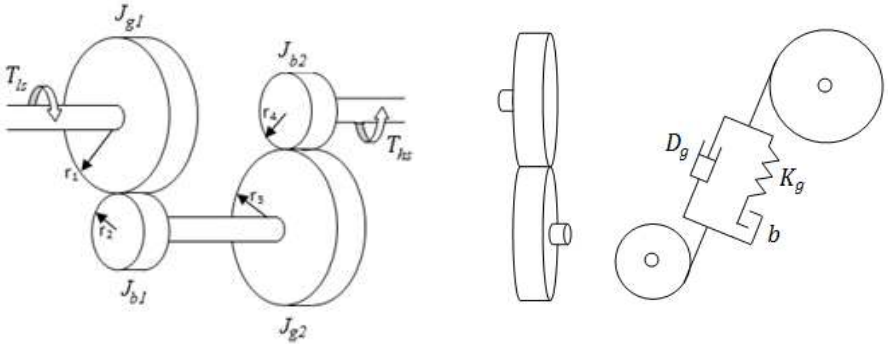

(a) (b)

Fig. 3.12: Gearbox system & its gear-pair models

T_{hs} is high speed shaft torque, $J_{g1}, J_{p1}, , J_{g2}$ and J_{p2} are the moment of inertia of gears and opinions, ω_{g1}, ω_{p1}, ω_{g2} and ω_{p2} are the angular speed, D_{g1}, D_{g2}, K_{g1} and K_{g2} are the damping and stiffness constants, r_{g1}, r_{p1}, r_{g2} and r_{p2} are the gear and pinion radiuses and x_1 and x_2 depend on the backlash b_1 and b_2 in each pair gears and they are described by:

$$x_1 = \begin{cases} (r_{g1}\theta_{g1} + r_{p1}\theta_{p1}) - b_1 & (r_{g1}\theta_{g1} + r_{p1}\theta_{p1}) > b_1 \\ 0 & (r_{g1}\theta_{g1} + r_{p1}\theta_{p1}) \le b_1 \\ (r_{g1}\theta_{g1} + r_{p1}\theta_{p1}) + b_1 & (r_{g1}\theta_{g1} + r_{p1}\theta_{p1}) < -b_1 \end{cases} \tag{3.14}$$

$$x_2 = \begin{cases} (r_{g2}\theta_{g2} + r_{p2}\theta_{p2}) - b_2 & (r_{g2}\theta_{g2} + r_{p2}\theta_{p2}) > b_2 \\ 0 & (r_{g2}\theta_{g2} + r_{p2}\theta_{p2}) \le b_2 \\ (r_{g2}\theta_{g2} + r_{p2}\theta_{p2}) + b_2 & (r_{g2}\theta_{g2} + r_{p2}\theta_{p2}) < -b_2 \end{cases} \tag{3.15}$$

Note that the speed of 1st pinion and 2nd gear are equal. In addition, the speed of gear1 and low speed shaft has the same value.

3.2.2.2.4 High Speed Shaft Model

The torsional equation of motion for this shaft is:

$$T_{hs} = D_{hs}(\omega_{hs} - \omega_{rm}) + K_{hs}(\theta_{hs} - \theta_{rm}) \quad 3.16$$

where θ_{hs}, θ_{rm}, ω_{hs} and ω_{rm} are the angular displacement and speed of the shaft and generator rotor, respectively, D_{hs} and K_{hs} are damping and stiffness constants.

3.2.2.2.5 Generator Mechanical Model

The moment of inertia of generator and mass plate (J_{gm}) is driven by the high speed shaft and braked by the electromagnetic torque (T_g) and friction and windage:

$$J_{gm}\dot{\omega}_{rm} = T_{hs} - T_g - K_{fg}\omega_{rm} - K_{wg}\omega_{rm}^2 \quad 3.17$$

where K_{fg} and K_{wg} are the friction and windage loss coefficients of the generator.

3.2.2.3 Electrical Model

3.2.2.3.1 Generator Electrical Model

For modelling the IG electrical system, standard transformations were used to map the 3-phase stator and rotor windings into direct and quadrature axis reference frame models with axes rotating at synchronous speed. When deriving the model, the *q*-axis was assumed to be 90" ahead of the *d*-axis in the direction of rotation. The *dq*-model is often used to reduce the *abc*-model complexity. A generalized 5th order mathematic model was used here for modelling the DFIG as shown in Fig. 3.13.

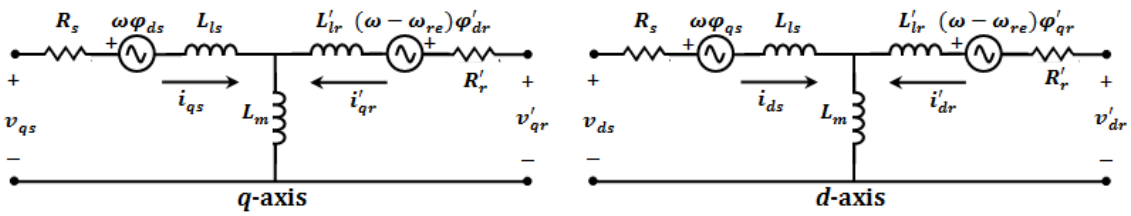

Fig. 3.13: *dq*-frame induction generator model

The equations describing an asynchronous machine in terms of phase variables were derived to develop the model with all rotor variables referred to the stator. Assume that the stator current is positive when flowing from the grid to the generator, and then the voltage expressions can be represented as [77]:

$$v_{ds} = R_s i_{ds} + \frac{d\varphi_{ds}}{dt} + \omega\varphi_{qs} \quad 3.18$$

$$v_{qs} = R_s i_{qs} + \frac{d\varphi_{qs}}{dt} + \omega\varphi_{ds} \quad 3.19$$

$$v'_{dr} = R'_r i'_{dr} + \frac{d\varphi'_{dr}}{dt} - (\omega - \omega_{re})\varphi'_{qr} \quad 3.20$$

$$v'_{qr} = R'_r i'_{qr} + \frac{d\varphi'_{qr}}{dt} + (\omega - \omega_{re})\varphi'_{dr} \quad 3.21$$

where v_{ds}, v_{qs}, v'_{dr} and v'_{qr} are the dq stator and rotor voltages, i_{ds}, i_{qs}, i'_{dr} and i'_{qr} are the dq- stator and rotor currents, φ_{ds}, φ_{qs}, φ'_{dr}, φ'_{qr} are the dq-stator and rotor fluxes, R_s, R'_r are the stator and rotor resistance, ω is the synchronous electrical angular speed and ω_{re} is the generator electrical angular speed. Sign (′) to indicate these parameters are in stator side. The terms of the stator and rotor flux can be expressed in the stator and rotor currents as:

$$\varphi_{ds} = L_s i_{ds} + L_m i'_{dr} \quad 3.22$$

$$\varphi_{qs} = L_s i_{qs} + L_m i'_{qr} \quad 3.23$$

$$\varphi'_{dr} = L'_r i'_{dr} + L_m i_{ds} \quad 3.24$$

$$\varphi'_{qr} = L'_r i'_{qr} + L_m i_{qs} \quad 3.25$$

where L_s and L'_r represent the stator and rotor self-inductances, respectively, and L_m is the mutual inductance between the stator and the rotor. Both of the stator and rotor self-inductances can be defined as:

$$L_s = L_{ls} + L_m \quad 3.26$$

$$L'_r = L'_{lr} + L_m \quad 3.27$$

with L_{ls} and L'_{lr} are the stator and rotor leakage inductances. The electromagnetic torque (T_g) expression of the induction machine is given by:

$$T_g = \frac{3}{2} p\ (\varphi_{ds} i_{qs} - \varphi_{qs} i_{ds}) \quad 3.28$$

where p is the number of pole pairs. The stator and rotor active and reactive powers are:

$$P_s = v_{ds} i_{ds} + v_{qs} i_{qs} \quad 3.29$$

$$P_r = v_{dr} i_{dr} + v_{qr} i_{qr} \quad 3.30$$

$$Q_s = v_{qs} i_{ds} - v_{ds} i_{qs} \quad 3.31$$

$$Q_r = v_{qr} i_{dr} - v_{dr} i_{qr} \quad 3.32$$

where P_s and P_r represent the stator and rotor active powers while Q_s and Q_r represent the stator and rotor reactive powers.

3.2.2.3.2 Converter Model

In order to be able to feed and control a DFIG from a variable frequency and voltage source, the DFIG was connected to a back-to-back converter consisting of two voltage source inverters separated by a DC link. The DC link separates the two inverters and therefore can be controlled independently of each other. Therefore, only the RSI has been considered in the model while the GSI and DC link have been replaced by a DC voltage source. In a real WT the GSI controls the reactive power exchange with the grid and the DC Link voltage. An ideal lossless representation of the RSI as depicted in Fig. 3.14 was assumed. It has six IGBTs (T1 to T6) where each one is equipped with anti-parallel diode. A PWM signals or gating signals (GS_1 to GS_3), are generated in the controller, switch on and off the transistors. The duty cycle of the transistor and the diode determines whether the transistor or a diode is conducting in a transistor leg (e.g., T1 and T4).

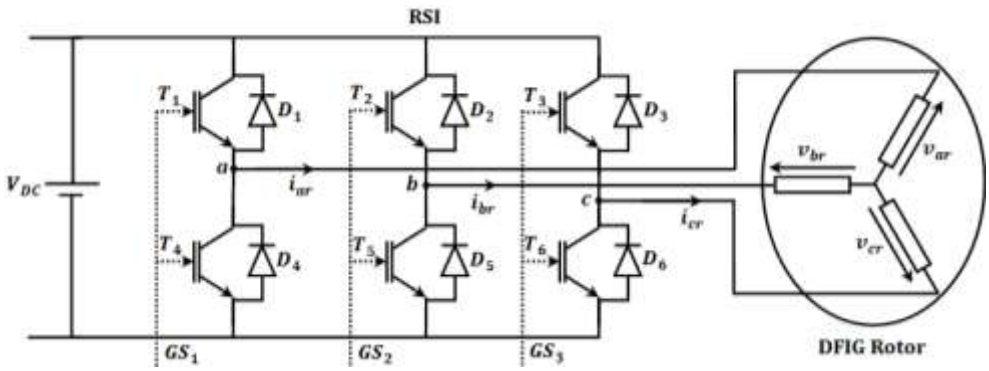

Fig. 3.14: Equivalent circuit of the RSI & DC Link voltage

3.2.2.3.3 The RSI Controller Model

The RSI is used to regulate the active and reactive power exchanged between the generator and the grid. In a real WT, the active power is controlled in order to be adapted to the wind speed and the reactive power control allows obtaining a unitary power factor between the stator and the grid. Based on the SFOVC, the controller has been designed and modelled in the system as shown in Fig. 3.15, where the torque and consequently active power can be regulated only through the q-rotor current component and the reactive power can be regulated by the d-rotor current component.

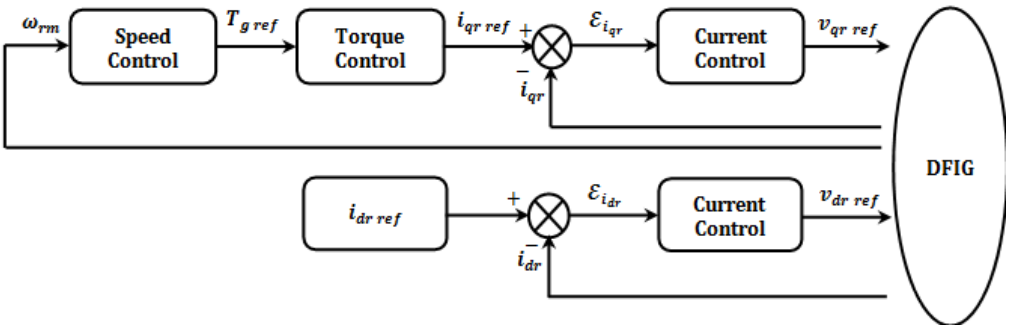

Fig. 3.15: Schematic diagram of the active & reactive power control of DFIG

The active power comprises 3 cascaded loops; q-rotor current control (PI), torque control and speed control while the reactive power has only d-rotor current control (PI). The relationship between the variables in this model can be expressed in the following forms as:

$$T_{g\,ref} = K_{opt}\omega_{rm}^2 \tag{3.33}$$

$$i_{dr\,ref} = 0 \tag{3.34}$$

$$i_{qr\,ref} = -\frac{2}{3}\cdot\frac{L_{ls}+L_m}{pL_m}\cdot\frac{\omega n_{sr}}{|V_s|}\cdot T_{ref} \tag{3.35}$$

$$v_{dr\,ref} = K_{pd}\varepsilon_{i_{dr}} + K_{id}\int_0^t \varepsilon_{i_{dr}}dt \tag{3.36}$$

$$v_{qr\,ref} = K_{pq}\varepsilon_{i_{qr}} + K_{iq}\int_0^t \varepsilon_{i_{qr}}dt \tag{3.37}$$

where $T_{g\,ref}$ is the generator reference torque, K_{opt} is the optimal power tracking factor, V_s is the magnitude of the stator phase voltage, n_{sr} is the turn ratio between stator and the rotor, $i_{dr\,ref}$ and $i_{qr\,ref}$ are the d- and q-rotor reference currents, $\varepsilon_{i_{dr}}$ and $\varepsilon_{i_{qr}}$ are

the d- and q-rotor error currents, $v_{dr\,ref}$ and $v_{qr\,ref}$ are the d- and q-rotor reference voltage, K_{pd} , K_{pq} , K_{id} and K_{iq} are the d- and q-current control parameters. The design of this controller and the derivative of the above equations will be described in details in the next chapter.

3.2.2.3.4 Grid Model

A simple model has been used to simulate the grid in the MATLAB model. The main components of this model is the grid voltage (V_G) and the grid impedance (Z_G), as shown in Fig. 3.16.

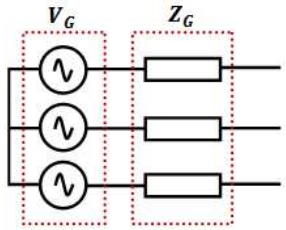

Fig. 3.16: Grid model

The grid voltage comprises three phase voltages (V_a, V_b and V_c) with same magnitude (V_s) and shifted by 120^o from each other as given by:

$$V_G = \begin{cases} V_a = V_s sin(2\pi ft) \\ V_b = V_s sin(2\pi ft + 120^o) \\ V_c = V_s sin(2\pi ft + 240^o) \end{cases} \quad 3.38$$

where f is the grid or supply frequency. Meanwhile, the grid impedance Z_G has been modelled with using 3-pahse RL impedance. The grid impedance for each phase can be written as:

$$Z_G = R_G + j2\pi f L_G \quad 3.39$$

where R_G and L_G are resistance and inductance of the grid. The impedance parameters have been estimated to have small values in order to generate some harmonics in the generator variables.

3.2.3 Parameters Values

3.2.3.1 Mechanical Parameters

These parameter values were initially measured by H. Wen-Ko [74]. Further work was performed to measure and calculate new mechanical parameters by J. Emslie in [75] including updating some of Wen-Ko's parameters. Finally, new measurements were carried out by the author for determining motor and generator friction and windage losses. This was done by running the Test Rig mechanically without connecting to the grid and measuring the torque and speed at generator side to calculate the mechanical power. Plotting the calculated power vs. measured speed in Microsoft Excel and using the fundamental mathematical relationships between speed, torque and power, the friction and windage loss coefficients of the generator were calculated. For calculating the friction and windage loss coefficients in the DC motor side, the generator was used to drive the motor. The same measurement procedures were repeated on the DC motor side. Details of the calculations can be found in Appendix A. In addition, Appendix A shows the motor constant calculation based on the manufacturer's data for the motor. A summary of the mechanical parameter values for each component is shown in Table 3.1.

3.2.3.2 Control & Electrical Parameters

The control loop parameters in the DC Motor Eurotherm Controller were measured directly from menu in the MMI. Implementing these values in the model gave a reasonable approximation to the Test time and frequency responses. However, to improve the accuracy of the time period and amplitude of the oscillations of the speed response so that they are more representative of those found from the Test Rig, the integral time values of the speed control parameter value was modified from 0.5sec to 0.166sec. This was found to produce a more accurate response. Furthermore, the generator parameters were determined experimentally, where the stator and rotor resistance were obtained using BS407 Precision Milli/Micro Ohmmeter. Then, the no-load test was carried out to calculate the magnetizing resistance and inductance. After that, the stator and rotor winding inductance were measured from the locked rotor test. For more details, see Appendix A. On the other hand, the grid impedance was not measured but a small value has been estimated and used. Finally, the PI control parameters of the RSI controller was designed and chosen by the author. The electrical parameters for DC motor, generator and grid as well as the control loops parameters of DC motor and RSI are shown in Table 3.2.

Table 3.1: Mechanical parameters

Characteristic	Symbol	Value		Unit	How obtained
		Data or measured	Modified in model		
1. DC motor					
Moment of inertia of DC motor	J_{DC}	0.226	-	kg.m^2	Given by [74]
Moment of inertia of DC motor & mass plate	J_{DCm}	0.7594	-	kg.m^2	Given by [75]
Motor constant	$K_{ø}$	0.57	-	Nm/amp^2	Calculated by author
Friction loss coefficient	K_{fDC}	1.222	-	Nm.sec/rad	Measured by author
Windage loss coefficient	K_{wDC}	0.001	-	Nm.sec^2/rad^2	Measured by author
Stiction torque	T_{DCs}	7.159	-	Nm	Measured by author
Maximum motor speed	ω_{DCmax}	2120	-	rev/min	Given by manufacture
2. Low speed shaft					
Stiffness	K_{ls}	4,119	14,000	Nm/rad	Given by [75]
Damping	D_{ls}	8.46	10	Nm.sec/rad	Given by [75]
3. Gearbox					
Moment of inertia of gear 1	J_{g1}	0.06630	-	kg.m^2	Given by [75]
Moment of inertia of pinion 1	J_{p1}	0.00013	-	kg.m^2	Given by [75]
Moment of inertia of gear 2	J_{g2}	0.03839	-	kg.m^2	Given by [75]
Moment of inertia of pinion 2	J_{p2}	0.05022	-	kg.m^2	Given by [75]
Radius of gear 1	r_{g1}	0.198	-	m	Given by manufacture
Radius of pinion 1	r_{p1}	0.039	-	m	Given by manufacture
Radius of gear 2	r_{g2}	0.228	-	m	Given by manufacture
Radius of pinion 2	r_{p2}	0.232	-	m	Given by manufacture
Stiffness of gear pairs 1	K_{g1}	5,000,000	-	Nm/rad	Given by [75]
Stiffness of gear pairs 2	K_{g2}	5,000,000	-	Nm/rad	Given by [75]
Damping of gear pairs 1	D_{g1}	500,000	-	Nm.sec/rad	Given by [75]
Damping of gear pairs 2	D_{g2}	500,000	-	Nm.sec/rad	Given by [75]
Backlash 1	b_1	0.0625	-	mm	Given by [75]
Backlash 2	b_2	0.2825	-	mm	Given by [75]
Gearbox ratio	n_{gb}	4.9893	-	-	Calculated by author
4. High speed shaft					
Stiffness	K_{hs}	1,711	50,000	Nm/rad	Given by [75]
Damping	D_{hs}	12.74	10	Nm.sec/rad	Given by [75]
5. Generator					
Moment of inertia of generator	J_g	0.414	-	kg.m^2	Given by [74]
Moment of inertia of generator & mass plate	J_{gm}	1.0198	-	kg.m^2	Given by [75]
Friction loss coefficient	K_{fg}	0.001	-	Nm.sec/rad	Measured by author
Windage loss coefficient	K_{wg}	0.00006	-	Nm.sec^2/rad^2	Measured by author
Stiction torque	T_{gs}	0.298	-	Nm	Measured by author
Mechanical synchronous speed	–	1500	-	rev/min	Calculated by author

Table 3.2: Control & electrical parameters

Characteristic	Symbol	Value		Unit	How obtained
		Data or measured	Modified in model		
1. DC motor control					
i. Speed control					
Proportional gain	K_{ps}	10	-	amp.sec/rad	Measured by author
Integral gain	K_{is}	20	60	amp/rad	Calculated and modified by author
Integral time	T_{is}	0.5	0.166	sec	Measured and modified by author
ii. Current control					
Proportional gain	K_{pc}	22.28	-	volt/amp	Measured by author
Integral	K_{ic}	4.28	-	volt/amp.sec	Measured by author
Integral time	T_{ic}	5.28	-	sec	Calculated by author
2. DC motor					
Armature resistance	R_a	0.117	-	Ω	Given by manufacture
Armature inductance	L_a	0.00264	-	H	Given by manufacture
Field winding resistance	R_f	112	-	Ω	Given by manufacture
Field winding inductance	L_f	17.8	-	H	Given by manufacture
Field voltage	V_f	360	-	volt	Given by manufacture
3. Generator					
Rated power	-	30	30	kW	Given by manufacture
Stator resistance	R_s	0.079	-	Ω	Measured by author
Stator leakage inductance	L_{ls}	0.802	-	mH	Measured by author
Magnetizing resistance	R_m	131.9	-	Ω	Measured by author
Mutual inductance	L_m	29.934	-	mH	Measured by author
Rotor resistance	R_r	0.044	-	Ω	Measured by author
	R'_r	0.072			
Rotor leakage inductance	L_{lr}	0.802	-	mH	Measured by author
	L'_{lr}	1.298			
Turn ratio	n_{sr}	1.272	-	-	Measured by author
4. Grid					
Phase voltage magnitude	V_s	110	-	volt	Measured by author
		326	-	volt	Measured by author
Frequency	f	50	-	Hz	
Grid resistance	R_G	-	0. 01	mΩ	Estimated by author
Grid inductance	L_G	-	0.5	μH	Estimated by author
5. RSI					
DC link voltage	V_{DC}	48	-	volt	Designed by author
		550	-	volt	Given by manufacture
PWM carrier frequency	f_{tri}	2.5	-	kHz	Given by manufacture
6. RSI controller					
i. Active power control					
Proportional gain	K_{pq}	3	10	volt/amp	Designed and modified by author
Integral gain	K_{iq}	3	10	volt/amp.sec	Designed and modified by author
Optimal power tracking factor	K_{opt}	0.001	-	$Nm.sec^2/rad^2$	Designed by author
		0.00458	-	$Nm.sec^2/rad^2$	Designed by author
ii. Reactive power control					
Proportional gain	K_{pd}	3	10	volt/amp	Designed and modified by author
Integral gain	K_{id}	3	10	volt/amp.sec	Designed and modified by author

3.2.4 Verification of the Mathematical Model

Various tests were carried out to verify the model against the physical system in time and frequency domains. The results demonstrate the good agreement between simulated and measured signals from the model and physical Test Rig in both domains. The time response of the generator speed and high speed shaft torque of the physical system and its model, in WRIG configuration, under different stages of speed demand are illustrated in Fig. 3.17. The speed was rapidly increased from 0.00sec up to synchronous speed, followed by a settling time before the grid synchronisation at 51.25sec. Step speed changes were made to the grid-connected generator at time 80.00sec and continued for the next 60.00sec before the grid was disconnected and the machine run down. It was difficult to disconnect the grid in the simulation because the MATLAB software will stop immediately after running the model. Therefore, the whole speed demand was applied in the physical Test Rig and only the first 140sec was applied to the model. These results demonstrate the good agreement between simulated and measured signals, where differences between values are small except at grid synchronisation. This is believed to be caused by a limit on the armature current rate of change, imposed by the DC controller to protect the DC controller and motor so that they do not absorb rapid torque transients and also as a means of limiting current overshoot for large current. However, further results illustrate the good agreement between the physical Test Rig and its MATLAB model with DFIG configuration in the time domain can be found in Chapter 5.

Another test was carried out to investigate this model with the Test Rig in the frequency domain. The PSD analysis of the resulted torque signals for a linear run up and run down condition is shown in Fig. 3.18. Several natural frequencies were observed, specifically 0.30Hz, 22.90Hz and 121.62Hz, corresponding closely to results from the physical Test Rig. It is clear that the model has now achieved good accuracy in frequency domain. Further study was achieved by the author in the model to analyse and relate the sensitivity of these frequencies to system components, and the obtained results show that:

- 0.30Hz component depends on the DC drive controller and the inertia of generator and mass plate;
- 22.90Hz component depends on the stiffness of low speed shaft and the inertia of DC motor and mass plate;
- 121.62Hz depends on the stiffness of low speed shaft, the inertia of the gearbox and the inertia of generator and mass plate.

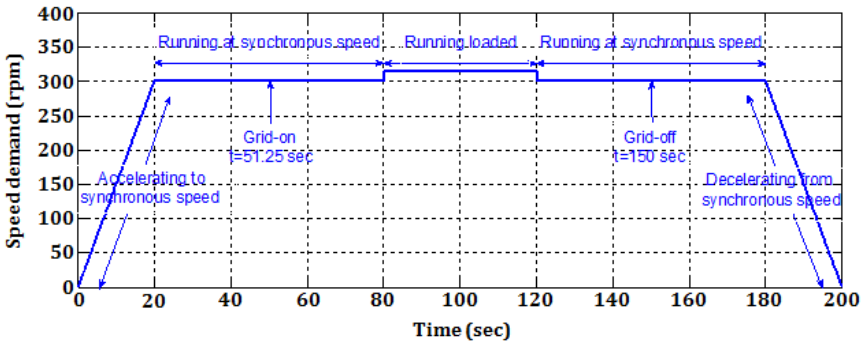

(a)

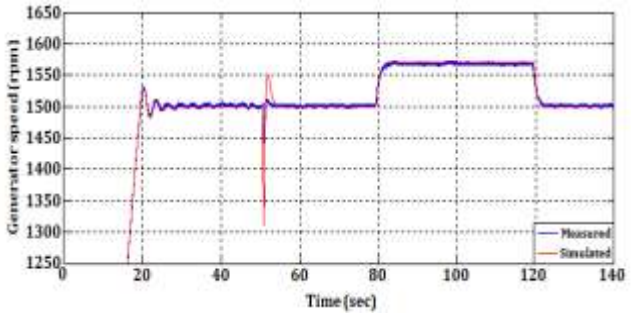

(b)

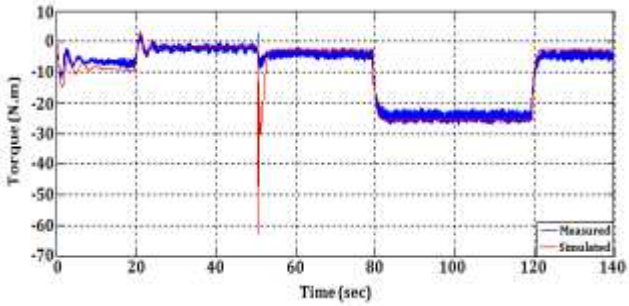

(c)

Fig. 3.17: Measured & simulated speed demand and time domain response of the Test Rig

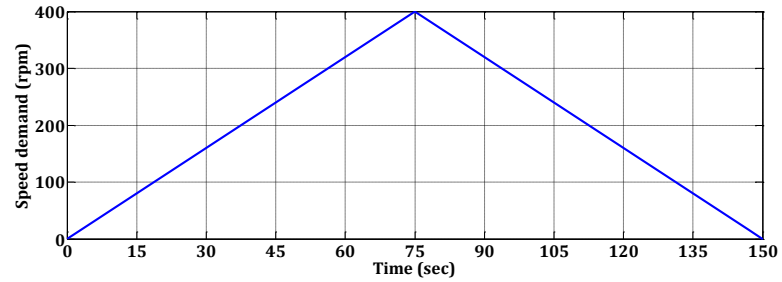

(a)

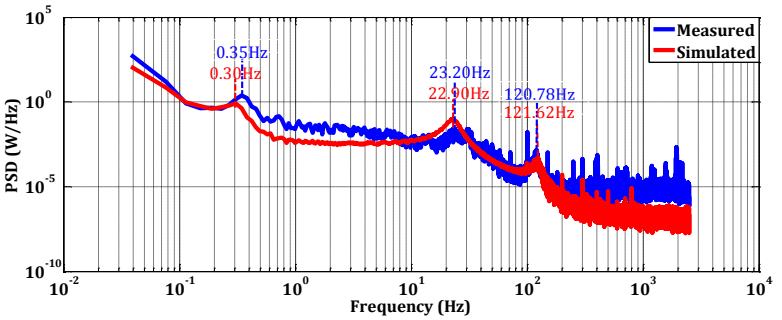

(b)

Fig. 3.18: Measured and simulated speed & torque PSD for the Test Rig

3.3 Conclusions

The Test Rig has been modified to represent a full variable speed drive train DFIG with back-to-back converter capable of operating at synchronous speed 1500rev/min ±30%. Furthermore, the Test Rig has been reconfigured to run as a variable speed WT-driven WRIG or DFIG depends on the user. A more detailed mathematical model of the Test Rig has been built and that model verified against the real Test Rig using a defined operational cycle including synchronisation in both time- and frequency-domain.

4 Control Scheme Model for Rotor Side Inverter

4.1 Introduction

For controlling the WT-driven DFIG, different strategies have been proposed over the last decade in the literature [78], [79], [80] and [81], including DTC, vector control and variable structure control. These strategies are based on the fact that BRWS, the WT will trace the maximum power-torque or power-speed curve whilst ARWS, the output power was limited to its rated value until the shutdown wind speed limit was reached. To trace the maximum power-torque or speed curve there are two methods of achieving it which are termed 'current-mode control' or 'speed-mode control' [82] while pitch regulation ensures rated power for the WT ARWS.

The vector control scheme, however, has become the favoured and the most adopted control technique in many induction machine applications [83], [84] due to its ability to obtain a fast dynamic response and accurate torque control [85]. In a variable speed WT, the DFIG was controlled via the rotor converter. The GSI was controlled to maintain a constant DC link voltage regardless of the magnitude and the direction of rotor power and to guarantee the operation of the inverter at unity power factor, i.e., zero reactive power [86], [87]. This means that the GSI exchanges only active power with the grid, and therefore the transmission of reactive power from DFIG to the grid was performed only through the stator winding [88]. The RSI independently controls the generator active power [86]. To some degree, the RSI can be considered as a current-controlled voltage source. Typically, there are two topologies can be used for applying a vector control scheme to control DFIG based on *dq*-transformation, which are:

- Stator flux-oriented vector control (SFOVC) in [80], [82] and [89] ;
- Rotor flux-oriented vector control (RFOVC) in [90].

With the SFOVC scheme, stator windings are directly connected to the grid, so the resulting stator voltage equations will be simpler than the rotor flux oriented ones [83] and easier to implement [91]. Moreover, the stator active and reactive power are controlled directly through the *q*-axis rotor current and *d*-axis rotor current, respectively, [80], [82]. However, the conventional approach for this is SFOVC using rotor position sensors whose performance depends on the rotor positional information accuracy,

derived from the position encoder or speed sensor [80], [92]. In general, the encoder increases system costs and is subject to failure, especially in stormy weather where the DFIG is used [92]. The SFOVC was adopted in this research to control the RSI. Considering that stator and grid resistances are comparatively small, the grid flux orientation aligns with the stator flux orientation without significant error [93].

The present work was limited to BRWS operational control strategy. The proposed maximum power extraction control strategy for the DFIG-based grid-connected WT employs the production torque as a dynamic reference to be imposed on the DFIG in BRWS mode. This methodology is known as current-mode control [82], [89]. The DFIG is controlled in a synchronously rotating *dq*-axis frame, with the *d*-axis oriented along the stator flux vector. In this way, a decoupled control between the electromagnetic torque and the rotor excitation current is obtained. The control of the GSI is not of primary concern for this study as the focus of this research detects the WT faults by observing the signals inside the RSI controller of the turbine.

Based on the current-mode control strategy, the RSI controller was designed and built for developing the MATLAB model and the physical Test Rig. This controller mainly consists of an active power optimization controller and a reactive power controller. Firstly, the optimal power extraction- generator speed characteristic for the Rig was extracted and used to define the optimal torque. Secondly, this torque was developed to define a reference torque and rotor reference current, which was imposed to the DFIG, after compensating for friction and windage. Finally, the reference currents were compared to the actual machine currents and passed through a standard PI controller and the rotor voltage required to control the speed of the machine was obtained.

4.2 DFIG Model Development & Current Control Scheme

As mention above, the SFOVC scheme was adopted to control the DFIG. Therefore, the following assumptions must be considered [94]:

- The stator flux vector is aligned with the d-axis of the stator;
- Stator voltage drop across resistance has been neglected as the influence of stator resistance is small compared to the grid voltage;
- Since the stator is connected to the grid, the magnetizing current of the stator is assumed to be determined by the grid.

Under these assumptions introducing the total magnetizing current (i_m) and neglecting the stator resistance ($R_s \simeq 0$), the relationship between the *dq*-axis stator

voltages, currents and fluxes which have previously been given in Chapter 3 can be rewritten in steady state as following:

$$v_{ds} = 0 \tag{4.1}$$

$$v_{qs} = |V_s| \tag{4.2}$$

$$i_{ds} = \frac{L_m}{L_s}(i_m - i'_{dr}) \tag{4.3}$$

$$i_{qs} = -\frac{L_m}{L_s} i'_{qr} \tag{4.4}$$

$$\varphi_{ds} = \frac{|V_s|}{\omega} \tag{4.5}$$

$$\varphi_{qs} = 0 \tag{4.6}$$

Substitute Eqs. 4.3 and 4.4 into Eqs. 3.24 and 3.25 the rotor fluxes can be formulated as:

$$\varphi'_{dr} = (L'_r - \frac{L_m^2}{L_s}) i'_{dr} + \frac{L_m^2}{L_s} i_m \tag{4.7}$$

$$\varphi'_{qr} = (L'_r - \frac{L_m^2}{L_s}) i'_{qr} \tag{4.8}$$

Consequently, the rotor voltage components can be developed by substitution of the rotor fluxes in current component form into Eqs. 3.20 and 3.21, then

$$v'_{dr} = R'_r i'_{dr} + L'_r \frac{di'_{dr}}{dt} - (\omega - \omega_{re})(L'_r - \frac{L_m^2}{L_s}) i'_{qr} \tag{4.9}$$

$$v'_{qr} = R'_r i'_{qr} + L'_r \frac{di'_{qr}}{dt} + (\omega - \omega_{re})((L'_r - \frac{L_m^2}{L_s}) i'_{dr} + \frac{L_m^2}{L_s} i_m) \tag{4.10}$$

Note that, both Eqs. 4.9 and 4.10 describe the rotor voltage in stator side. These equations can be rewritten in the rotor-side as:

$$v_{dr} = R_r i_{dr} + L_r \frac{di_{dr}}{dt} - (\omega - \omega_{re})(L_r - \frac{L_m^2}{n_{sr}^2 L_s}) i_{qr} \tag{4.11}$$

$$v_{qr} = R_r i_{qr} + L_r \frac{di_{qr}}{dt} + (\omega - \omega_{re})((L_r - \frac{L_m^2}{n_{sr}^2 L_s}) i_{dr} + \frac{L_m^2}{n_{sr} L_s} i_m) \tag{4.12}$$

where n_{sr} is the turn ratio between stator and rotor. The last terms in both equations causes a cross-relation between the two rotor current components. Also, it is possible to write the electromagnetic torque, the stator active and reactive power as a function of stator voltage and *dq*-rotor current components as following:

$$T_{em} = -1.5p\frac{L_m}{L_s}\frac{|V_s|}{\omega}i'_{qr} = -1.5p\frac{L_m}{L_s}\frac{|V_s|}{\omega}\frac{i_{qr}}{n_{sr}} \quad 4.13$$

$$P_s \cong -1.5\frac{L_m}{n_{sr}L_s}|V_s|i_{qr} \quad 4.14$$

$$Q_s \cong 1.5 \cdot \frac{L_m}{L_s} \cdot |V_s|\left(\frac{|V_s|}{\omega L_m} - \frac{i_{dr}}{n_{sr}}\right) \quad 4.15$$

By assuming the stator voltage magnitude and frequency are constant, the torque and active power can be considered proportional to the q-axis rotor current component and the reactive power related to the d-axis rotor current component.

4.3 Maximum Power Extraction & Speed Control Strategy

For a given WT, the maximum mechanical power extracted from the air stream depends upon the wind speed and the turbine rotational speed, which is generally expressed as:

$$P_T = 0.5\rho\pi C_p(\lambda,\beta)R^2u^3 = 0.5\rho\pi C_p(\lambda,\beta)\frac{R^3}{\lambda^3}\omega_T^3 \quad 4.16$$

where ρ is the air density, C_p is the power coefficient, λ is the tip speed ratio, β is the pitch angle, R is the turbine radius and ω_T is the turbine rotational speed. From the above equation, the turbine blade is characterised by particular $C_p - \lambda, \beta$ curves, and from them the optimal power extraction-speed characteristics can be derived for various wind velocity values u. With neglecting the loss in the gearbox, the above equation can be written as function of rotor generator speed (ω_{rm}) as:

$$P_T = 0.5\rho\pi C_p(\lambda,\beta)\frac{R^3}{n_{gb}^3\lambda^3}\omega_{rm}^3 \quad 4.17$$

where n_{gb} is the gearbox ratio, and the power is proportional to the generator rotational speed. In a variable speed WT below rated wind speed, the term of

$$0.5\rho\pi C_p(\lambda,\beta)\frac{R^3}{n_{gb}^3\lambda^3} \approx constant \approx K \quad 4.18$$

and the relationship between power and generator speed can be formulated as:

$$P_T = K\omega_{rm}^3 \quad 4.19$$

Fig. 4.1 demonstrates the typical characteristic with fixed β for the 30kW WT emulated in the physical Test Rig BRWS.

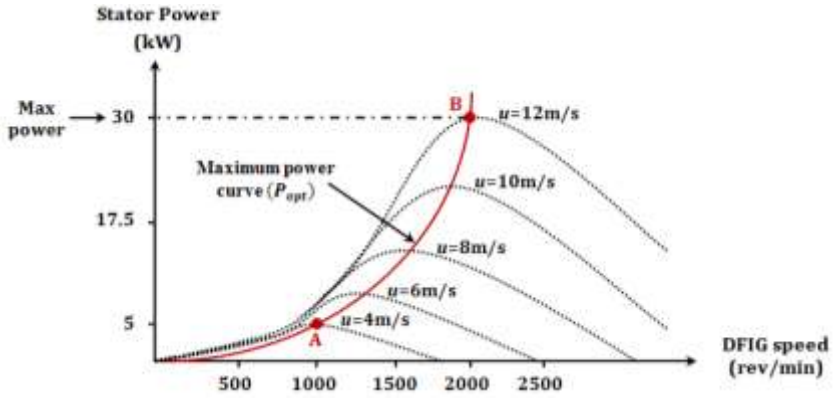

Fig. 4.1: WT characteristics with the optimal power extraction speed curve

Since the wind cannot be controlled, the turbine rotational speed is then controlled to optimize the WT's power extraction. In order to obtain the maximum possible energy from the turbine, the controller should regulate the turbine speed to operate between points (A-B) on the optimal power extraction-speed characteristics curve, defined by:

$$P_{Topt} = K_{opt}\omega_{rm}^3 \tag{4.20}$$

At point B in the characteristic curve in Fig. 4.1 for the Test Rig, the rated stator power is 30kW when the generator speed (4-pole DFIG) is 1950rev/min or 204rad/sec. Recalling Eq. 4.20, the parameter K_{opt} is computed as:

$$K_{opt} = \frac{P_{Topt}}{\omega_{rm}^3} = \frac{P_S}{\omega_{rm}^3} = \frac{30{,}000}{(204)^3} \approx 0.0036\ \text{W.sec}^3/\text{rad}^3 \tag{4.21}$$

and the corresponding torque produced by the turbine in this case is defined by:

$$T_{opt} = K_{opt}\omega_{rm}^2 \tag{4.22}$$

with K_{opt} value and Eq. 4.22, the optimal torque-speed characteristic derived, which was then applied to the controller model, as shown in Fig. 4.2.

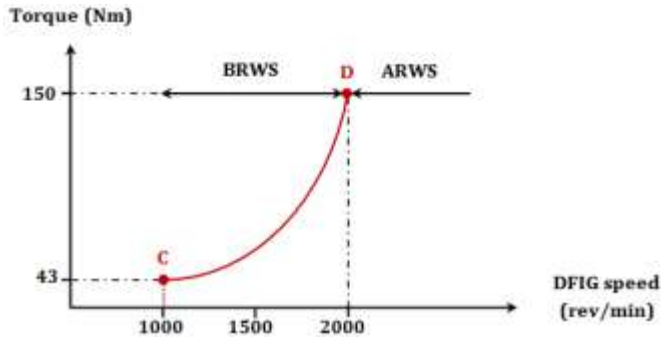

Fig. 4.2: Torque-speed characteristic for control strategy

However, this torque-speed characteristic curve cannot be used in the physical Test Rig with a gearbox installed because of the generator torque limitation. From its specification the maximum torque the DC motor can produce is 248Nm and, with the gearbox, the maximum resultant generator torque would be 50Nm, which is about the minimum torque required by the control strategy. Therefore, the author modified the characteristic curve by setting K_{opt} value to $0.001\text{Nm.sec}^2/\text{rad}^2$ to give a generator torque variation from 12Nm to 42Nm, that is from sub- to super-synchronous speeds. This modified curve was applied in both the physical Test Rig and MATLAB model to control the RSI connected to the 48volt DC link batteries, reducing the generator stator phase voltage magnitude to 110volt.

4.4 Active Power Optimization Control

The DFIG was controlled according to a pre-defined power-speed characteristic to optimize wind power extraction. Thus, active power optimization control is actually generator speed control. According to the decoupled *dq*-axis mapping, *q*-axis and *d*-axis rotor current components are controlled for torque and active power respectively. Due to its reliability and robust performance in the field, a proportional integral (PI) controller was used.

The electrical and mechanical dynamics of the induction machine has different time scales and the electrical dynamics are fast. Therefore, it was necessary to control the machine in a cascade structure [95], shown in Fig. 4.3. By using current control loop methodology, Active Power Control comprises 3 cascaded loops: *q*-axis rotor current, torque and speed control. Considering that torque is difficult to measure, it is most often controlled in open-loop.

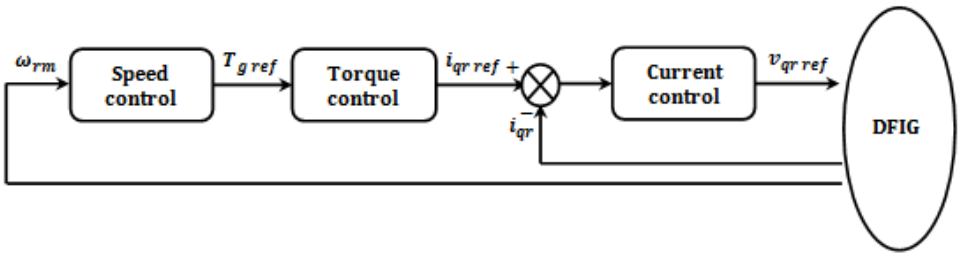

Fig. 4.3. Active power control of DFIG

4.4.1 Speed Control

The characteristic curve in Fig. 4.2 was used as a dynamic reference for the generator torque demand as a function of measured generator speed. The speed control scheme operates by modifying the electromagnetic generator torque to react to variations in turbine rotational speed. The speed control scheme imposes a reference torque on the DFIG rotor for given generator speed according to Eq. 4.23 after compensating for the friction and windage losses.

$$T_{ref} = K_{opt}\omega_{rm}^2 - K_{fg}\omega_{rm} - K_{wg}\omega_{rm}^2 \tag{4.23}$$

Later this reference torque will be used in the next stage to calculate the reference value of q-rotor current ($i_{qr\,ref}$) in the torque control.

4.4.2 Torque Control

From Eq. 4.12, the decoupling between the electromagnetic torque and the q-rotor current was obtained. The objective of this controller is to develop this relationship and use it to calculate the reference value of q-axis rotor current as:

$$i_{qr\,ref} = -1.5\,\frac{L_s}{pL_m}\cdot\frac{\omega}{|V_s|}n_{sr}T_{ref} \tag{4.24}$$

which will be used as an input for q-axis rotor current control.

4.4.3 q-Axis Rotor Current Control

Although the q-rotor reference current imposes the effect of torque control, the RSI is a controlled rotor voltage source. Hence, a final stage of the active power controller was implemented using the current error resulting from the reference torque. To determine the required rotor voltage v_{qr}^*, a standard PI controller was implemented. With comparing the reference current to the actual generator current and the error signal was processed by the controller, the rotor voltage for controlling the DFIG was generated.

$$v_{qr}^* = K_{pq}\mathcal{E}_{i_{qr}} + K_{iq}\int \mathcal{E}_{i_{qr}}\,dt \tag{4.25}$$

where

$$\mathcal{E}_{i_{qr}} = i_{qr\,ref} - i_{qr} \tag{4.26}$$

This control scheme is shown in Fig. 4.4. To ensure good tracking of these currents, the cross-magnetisation compensation terms are added to the controller output (v_{qr}^{*}) and obtained the reference value of the rotor voltages $v_{qr\,ref}$ which can be formulated as:

$$v_{qr\,ref} = K_{pq}\mathcal{E}_{i_{qr}} + K_{iq}\int \mathcal{E}_{i_{qr}}\,dt + (\omega - \omega_{re})((L_r - \frac{L_m^2}{n_{sr}^2 L_s})i_{dr} + \frac{L_m^2}{n_{sr}L_s}i_m) \qquad 4.27$$

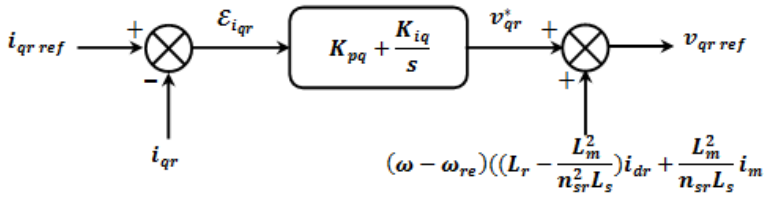

Fig. 4.4: Block diagram of *q*-axis rotor current control

This signal will modify the switching sequence to produce the required voltages at the output of the converter. So, the proper estimation of current controller parameters is essential for enhancing the performance of the system.

4.5 Reactive Power Control

The reactive power delivered by the WT generator stator directly depends on the rotor *d*-axis current. Therefore, reactive power control was performed through *d*-axis rotor current, the principle of this control. A similar analysis to the rotor current *d*-axis control was carried out for the rotor current *q*-axis control can likewise be done. A standard PI controller and summation of the direct rotor current compensation term, derived from Eq. 4.11, was implemented to obtain the reference rotor voltage $v_{dr\,ref}$ as shown in the figure below.

$$v_{dr\,ref} = K_{pd}\mathcal{E}_{i_{dr}} + K_{id}\int \mathcal{E}_{i_{dr}}\,dt - (\omega - \omega_{re})(L_r - \frac{L_m^2}{n_{sr}^2 L_s})i_{qr} \qquad 4.28$$

where

$$\mathcal{E}_{i_{dr}} = i_{dr\,ref} - i_{dr} \qquad 4.29$$

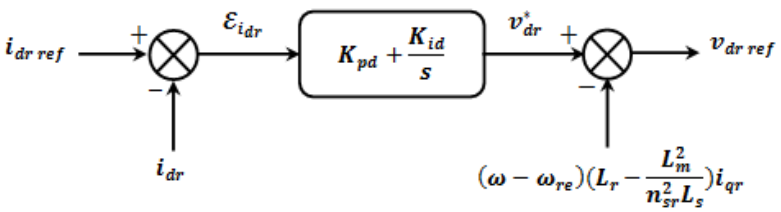

Fig. 4.5: Block diagram of *d*-axis rotor current control

Since the control system is symmetrical, the PI controllers have the same parameters for the rotor current *d*- and the *q*-axis loops. Assuming that all machine reactive power was supplied by the stator, the reference value of *d*-axis rotor excitation current may set to zero ($i_{dr\,ref} = 0$). As a result of setting this value, the total magnetization current (i_m) drawn by the machine to maintain the field flux will be provided by the *d*-axis component of the stator. Using Eqs. 4.3 and 4.4, the magnetization current can be calculated by:

$$i_m = i_{ms} = \frac{L_S}{L_m} i_{ds} = \frac{|V_S|}{\omega L_m} \tag{4.30}$$

In practice, it is generally desirable to keep the *d*-axis rotor current to a minimum and supply magnetising current entirely from the stator to decrease converter current, reduce converter losses [82] and limit converter rating, which minimises converter size and cost.

4.6 PWM Generator

A PWM scheme, based on a triangular carrier, was used to control the converter IGBT switches. Here, a PWM generator block diagram with RSI 3-phase bridge inverter and DFIG rotor is shown in Fig. 4.6. The pulsating rotor voltage was obtained by alternately switching in each phase the upper and lower IGBT switches.

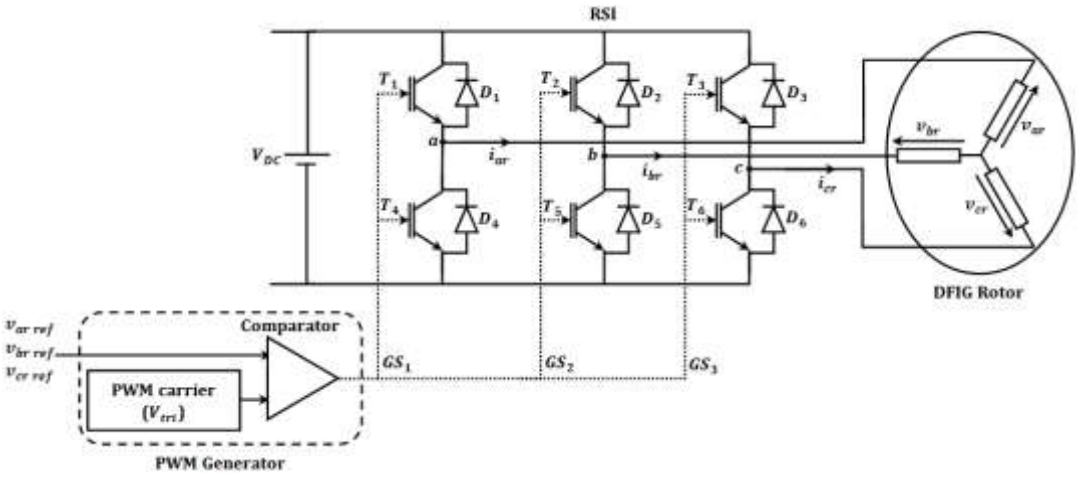

Fig. 4.6: Scheme of PWM voltage source converter

However, several converter switching functions can be employed to yield identical output results. In this research, the switching function employed is demonstrated in Fig.

4.7, and it is known as a sinusoidal or sine-triangle PWM (SPWM). this type of functions has the advantage of simplifying the analysis and evaluation [96]. In this way, all the sinusoidal rotor reference phase voltage outputs from the controller, displaced over 120° or 240° respectively, are compared with a triangular carrier wave (V_{tri}). For example, when $V_{ar\,ref} > V_{tri}$ as shown in Fig. 4.7a, the logical output signal of the comparator is positive and the upper switch was closed. Meanwhile, if $V_{ar\,ref} < V_{tri}$, the logical output signal of the comparator is negative and then the lower switch was closed. Fig. 4.7b illustrates the output signal of the comparator, also called gating signal (GS_1), which can be expressed as Fourier series [96] by:

$$GS_1(t) = \sum_{\substack{n=1 \\ n\ odd}}^{\infty} B_n \sin(n\omega_r t) \tag{4.31}$$

where B is the Fourier series coefficient, ω_r is the fundamental frequency of the Fourier series which is the required frequency of the rotor voltage and can be obtained as:

$$\omega_r = \omega - \omega_{re} = \omega - p\omega_{rm} \tag{4.32}$$

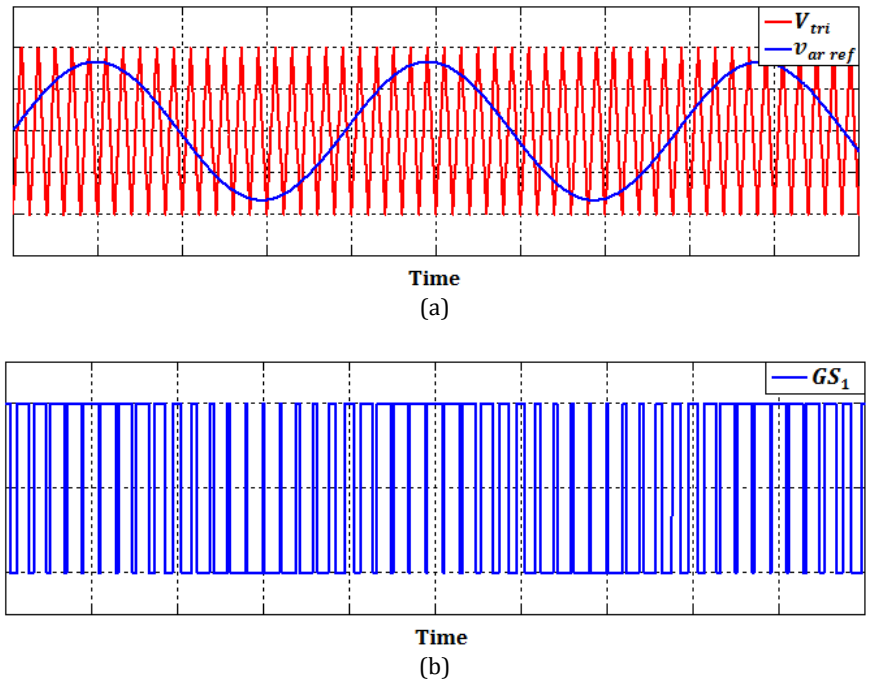

Fig. 4.7: Switching concept of PWM voltage source converter

In the same way, the IGBT switches of the other two inverter legs were open and closed according to output signals GS_2 and GS_3 from the comparator. With this concept,

the rotor phase voltages v_{ar}, v_{br} and v_{cr} were obtained by multiplication of the DC link voltage V_{DC} with the gating signals as follows:

$$v_{ar}(t) = \frac{V_{DC}}{2} GS_1(t) = \frac{V_{DC}}{2} \sum^{\infty}_{\substack{n=1 \\ n\ odd \\ n \neq triplen}} B_n \sin(n\omega_r t) \quad 4.33$$

$$v_{br}(t) = v_{ar}(t - 120^o) \quad 4.34$$

$$v_{cr}(t) = v_{ar}(t + 120^o) \quad 4.35$$

Similarly, the respective line to line voltagesV_{abr}, V_{bcr} and V_{car} are given by:

$$V_{abr}(t) = v_{ar}(t) - v_{br}(t) = \sqrt{3}\frac{V_{DC}}{2} \sum^{\infty}_{\substack{n=1 \\ n\ odd \\ n \neq triplen}} B_n \sin(n(\omega_r t + 30^o)) \quad 4.36$$

$$V_{bcr}(t) = V_{abr}(t - 120^o) \quad 4.37$$

$$V_{car}(t) = V_{abr}(t + 120^o) \quad 4.38$$

Fig. 4.8 shows the inverter rotor phase and rotor line voltage waveforms obtained from the MATLAB Simulink model.

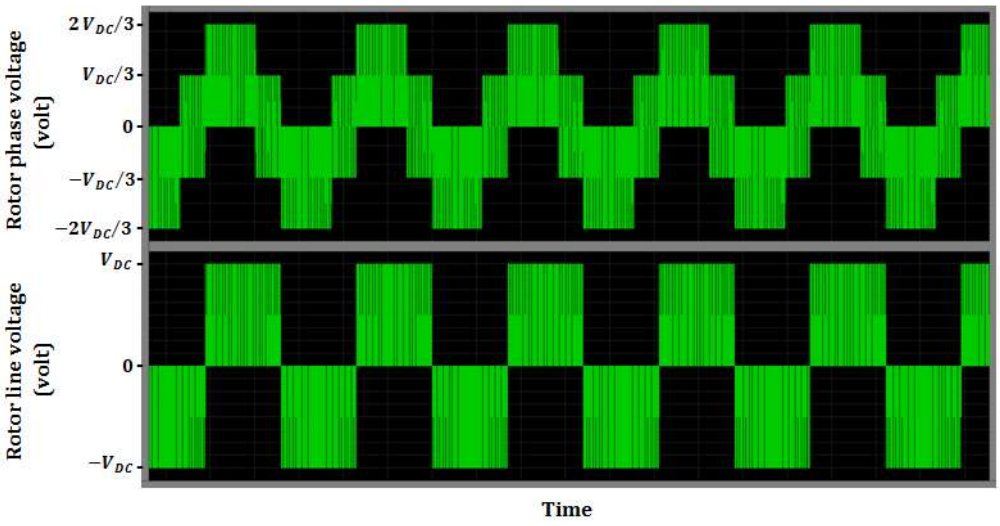

Fig. 4.8: Rotor voltage waveforms

4.7 Other Control Parameters

A schematic diagram of the overall generator control system is shown in Fig. 4.9. The RSI provides the actuation and the control requires the stator and rotor currents, stator voltages and generator speed to be measured. In order to achieve control, Clarke and Park transformations and their inverse were used. The control algorithm also computed the stator flux phase angle. Furthermore, to improve controller performance the initial DFIG rotational position was measured and several LPFs were applied to improve some measurements quality.

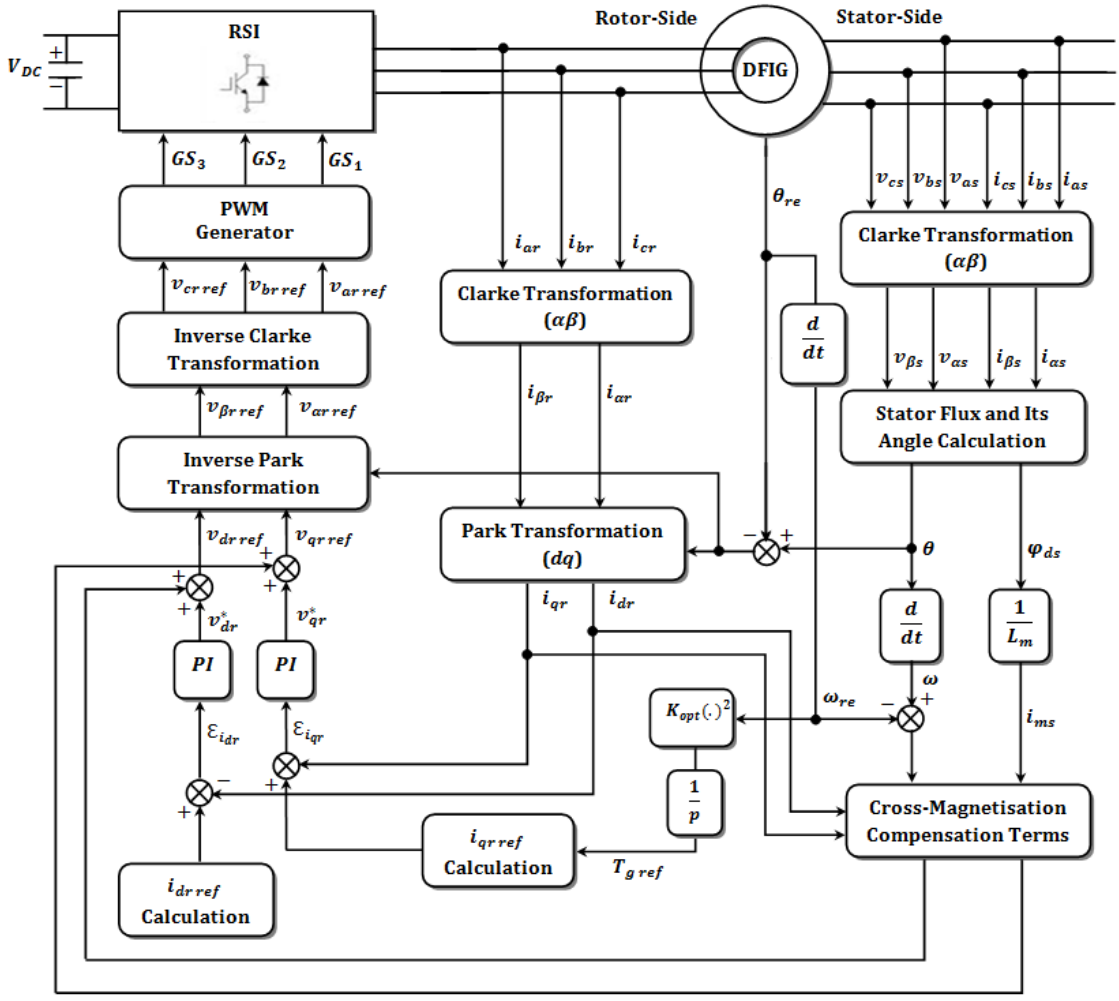

Fig. 4.9: Block diagram of the RSI controller

4.7.1 Clarke and Park Transformations

The controller diagram contains a Clarke Transformation block which transforms 3-phase *abc* quantities into a stationary *αβ*-reference frame whilst the Inverse Clarke Transformation block transformed from the *αβ*-reference to the abc frame. With stator flux phase and rotor position angles, the transformations from *αβ*-reference frame to synchronous *dq*-reference frame and the inverse were performed by the Park and Inverse Park Transformation blocks, respectively. The mathematical description for these transformations is presented in Appendix B.

4.7.2 Stator Flux Angle

The synchronous *dq*-reference frame was rotating at the same speed as the stator voltage (ω), and the stator flux angle was computed using components of the estimated stator flux in the stator *αβ*-frame, according to

$$\varphi_{\alpha s} = \int (v_{\alpha s} + R_s i_{\alpha s}) dt \tag{4.39}$$

$$\varphi_{\beta s} = \int (v_{\beta s} + R_s i_{\beta s}) dt \tag{4.40}$$

$$\theta = tan^{-1} \frac{\varphi_{\beta s}}{\varphi_{\alpha s}} \tag{4.41}$$

where $v_{\alpha s}$, $v_{\beta s}$, $i_{\alpha s}$, $i_{\beta s}$, $\varphi_{\alpha s}$ and $\varphi_{\beta s}$ are the stator voltage, current and flux components in *αβ* frame.

4.7.3 Rotor Electrical Angle

The *dq*-reference frame of the rotor is rotating at electrical speed ($\omega - \omega_{re}$). From the rotor mechanical angular displacement (θ_{rm}), the control algorithm computed the rotor electrical angular displacement, rotor mechanical and electrical speeds by:

$$\theta_{re} = p\theta_{rm} \tag{4.42}$$

$$\omega_{rm} = \frac{d}{dt}\theta_{rm} \tag{4.43}$$

$$\omega_{re} = \frac{d}{dt}\theta_{re} = p\frac{d}{dt}\theta_{rm} = p\omega_{rm} \tag{4.44}$$

However, the incremental encoder, fitted on the physical Test Rig, provided a measure of the relative rotation angle with respect to an initial rotor angular displacement, θ_{rmi}. As a result, the mechanical angle obtained from the encoder and the calculated electrical angle were only equal to θ_{rm} and θ_{re}, respectively, if the rotor and the stationary reference frames were initially aligned at $\theta_{rmi} = 0$. But this was not the situation for the Test Rig DFIG where earlier results showed that $\theta_{rmi} \neq 0$. Therefore, to increase the angular computational accuracy and improve system performance it was necessary to identify this initial rotor position value at some instant. A test was made and the initial position of the DFIG rotor was found to be $\theta_{rmi} = 2.4^o$ from the stationary reference frames. From this moment onward, the encoder measured the mechanical angle increment $\Delta\theta_{rm}(t)$ with respect θ_{rmi}, and $\theta_{rm}(t)$ was derived by adding θ_{rmi} to $\Delta\theta_{rm}(t)$. Then, the electrical angle is estimated by:

$$\theta_{re}(t) = p(\Delta\theta_{rm}(t) + \theta_{rmi}) = p(\Delta\theta_{rm}(t) + 2.4^o) \quad 4.45$$

4.7.4 Filters

For the physical Test Rig, several high pass filters (HPFs) with a 0.63Hz cut-off frequency were inserted in the controller model in the xPC TargetBox environment. These filters were used for the stator current and voltage measurements to eliminate current and voltage transducer DC offsets. Furthermore, experimental time measurements showed visible *dq*-rotor current noise, to be explained in the next section. Therefore, it was decided that *dq*-rotor current signal filtering was also required. As a result of this a 50Hz LPF was applied initially to these signals in the physical Test Rig and then extended into the MATLAB model.

4.8 Results

Several tests were carried by the author to investigate the RSI controller's performance by comparing physical Test Rig and MATLAB model test results. For this purpose, the time domain response of the Test Rig controller and model were analyzed at different operation conditions. The results are given below showing the response of the DFIG and the RSI controller in sub-synchronous operation. For these tests, the Test Rig was driven by the DC motor under speed demand with different step changes as shown in Fig. 4.10. The speed demand was initially applied to the physical Test Rig to measure the resultant generator speed, rotor and stator currents and other system responses. The grid

frequency was also measured during the tests and found to vary from 49.91Hz to 50.10Hz. The reason for measuring grid frequency was because generator speed and torque, and hence control performance, was affected by frequency. Any small frequency change can lead to significant results differences. However, it proved difficult to record grid frequency variation in the lab continuously against time. Therefore, the 50Hz average was used and applied to the model. Furthermore, in order to apply the same operating conditions in the simulation test, the grid (stator) voltage was also measured. Again, this voltage was varied between the 3-phases around the set value, due to changing loads on the individual phases within the University site. However, the unbalance was relatively invariant with time, so measured voltage values were averaged to 110volt, 109volt and 108volt for phases *a*, *b* and *c*, respectively, and then applied to the model.

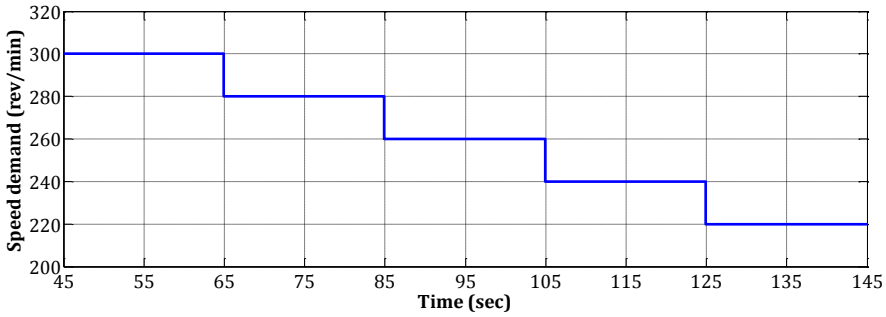

Fig. 4.10: DC motor speed demand of the physical Test Rig & the MATLAB model

4.8.1 DFIG Speed

Fig. 4.11 demonstrates the response to step changes of speed demand in the generator speed. The experimental signal was obtained from the rotor position measurement inside the xPC TargetBox environment as discussed in Chapter 3. As we can see, the model achieved good accuracy in the generator speed response with oscillation corresponding closely at step speed changes for between the model and physical Test Rig.

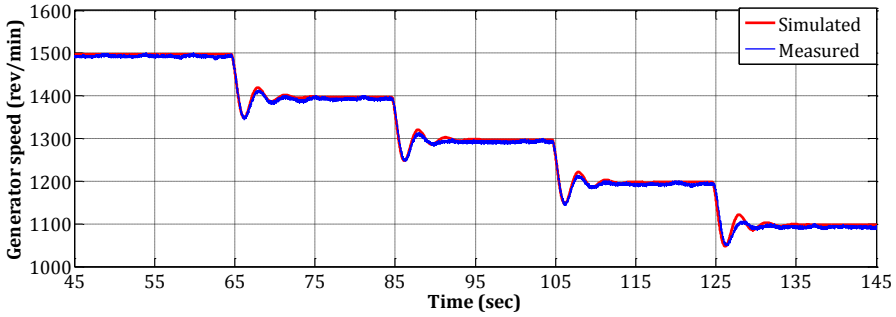

Fig. 4.11: Generator speed response of the physical Test Rig & the model

4.8.2 Rotor Currents

The closed loop response was investigated using the rotor currents. Fig. 4.12 displays the actual currents from measurement and simulation for the *q*-rotor reference, with the excitation *d*-rotor current maintained at zero. Several observations can be made from these results. Firstly, the controller worked correctly, the generated and actual *q*-rotor reference currents correspond, following the generator speed changes precisely. Secondly, the controller performances experimentally and in simulation were similar where the simulated control signals closely correlate with measured signals. However, there was noise in the measured signals compared to the noise-free simulation signals and it was found that several fundamental causes are responsible for the overall noise and they will be explained in section 4.8.4.

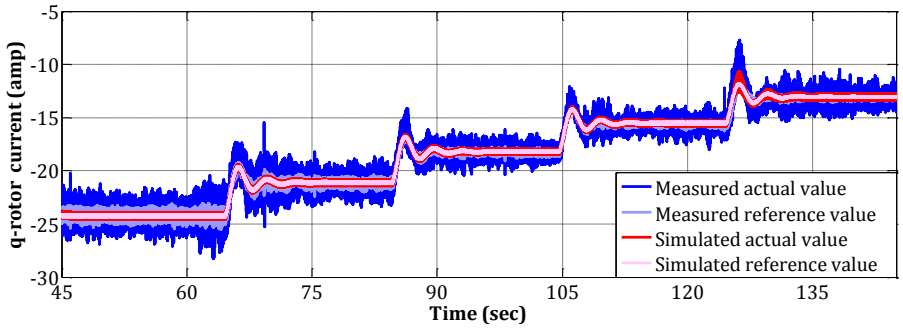

Fig. 4.12: Responses of *q*-rotor reference, measured & simulated currents to speed demand step changes

The system performance was also evaluated for the rotor phase currents. A comparison between the measured and simulated rotor current for one phase is presented in Fig. 4.13. It is clear that there was good agreement between measured and simulated data with a slight variation due to frequency. As mentioned above, the grid frequency varies around 50Hz between 45sec to 65sec, when the Rig was operated close to synchronous speed, and the effects can be seen in Fig. 4.13(a) and in more detail in Fig. 4.13(b).

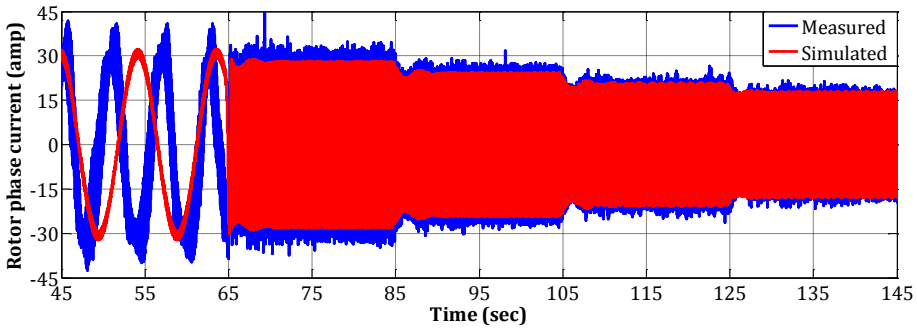

(a)

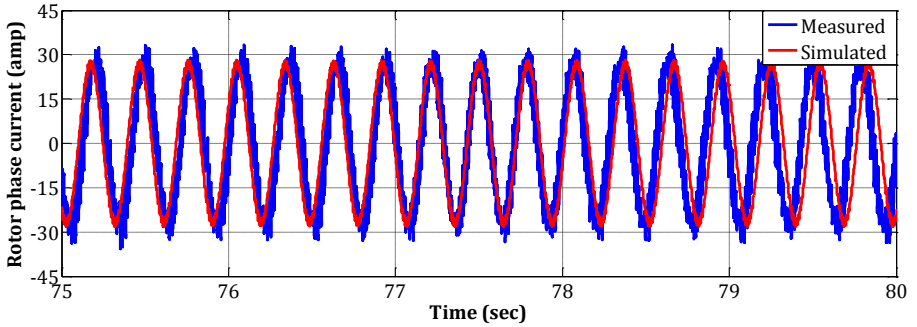

(b)

Fig. 4.13: Rotor phase current measured & simulated responses to speed demand step changes

4.8.3 Stator Powers & Currents

The influence of speed changes on stator power and current produced by the system were then studied. Fig. 4.14 shows the corresponding the total stator active and reactive powers and Fig. 4.15 shows the response of the stator phase currents. The behaviour of the active power variations as well as the currents was similar for the measured and simulated systems. However, it is clear that although the reactive power was constant at around 1950VAr, it had limited variations around 1950VAr at step speed changes in both measured and simulated systems. Again, the measured quantities contained noise due to the reasons which will be discussed in section 4.8.4.

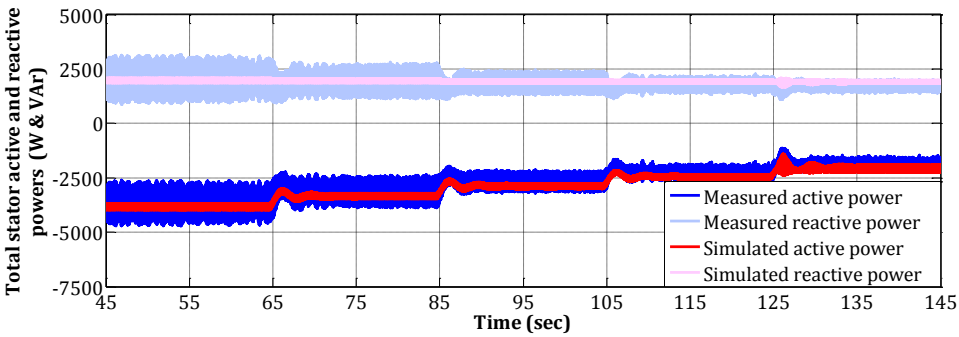

Fig. 4.14: Measured & simulated total stator power responses to step changes in speed demand

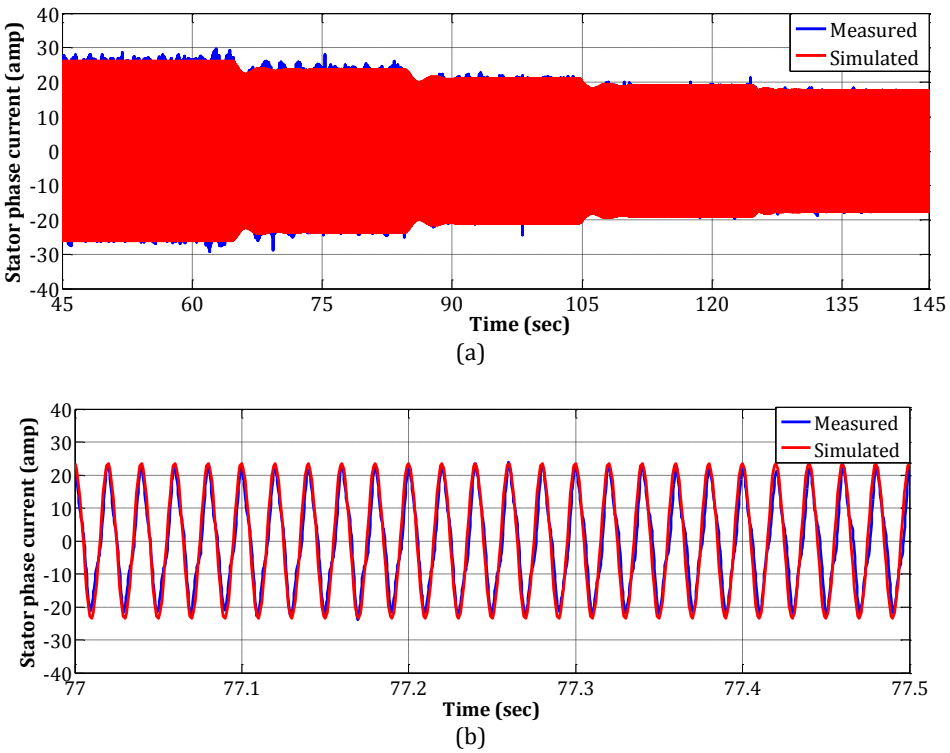

Fig. 4.15: Measured & simulated stator current responses to step changes in speed demand

4.8.4 Noise

It can be seen easily that the measured quantities are contaminated with noise. This noise is generated in the experimental Test Rig by combination of different reasons such as the noise from the voltage and current cards, but the main noise sources in this system are:

- The small continuous fluctuation in the grid frequency around 50Hz. This fluctuation leads to change the torque, synchronous electrical angular speed, electrical angular speed of the generator rotor, the speed of the *dq*-reference frame and then the RSI control quantities.
- Stator magnetising unbalance. It was found from frequency analysis to rotor and stator currents that the current DFIG has clear impedance unbalance in the stator circuit, due to a rotor eccentricity unbalancing the machine magnetising reactance between the three phases.
- The three phase PWM signals (GS_1 to GS_3) were unsynchronised, because of xPC TargetBox hardware limitations. Therefore, there will always be a delay between signals affecting converter IGBT switching, producing noise in rotor voltages and currents.

- Grid voltage unbalance. The grid voltage measurements showed that an unbalance between the 3-phase voltage values in the University site. Even this unbalance is small but it contributes in the stator unbalance and the noise.

Unfortunately, these noise sources are unavoidable with the current measurements from the physical Test Rig. However, they are not specific to the Test Rig and would also be present in the real machines where the machines and the grid are not perfect.

4.9 Conclusions

From all these measured and simulated results, it is clear that the RSI controller, designed and built by the author, accurately enables the Test Rig to represent a variable-speed WT-driven DFIG and the MATLAB model, constructed by the author, to represent that Test Rig.

5 WT Induction Generator Failures & Signal Processing

5.1 WT Induction Generator Failures

5.1.1 Introduction

Wind generators are one of the critical components in a WECS. However, weather, turbulent wind conditions, duty and installation issues may accelerate generator failure sooner than expected generator life. As mentioned in Chapter 2, these generators are prone to many electromechanical faults, for example in the stator, rotor, bearings and air gap, due to eccentricity. The major generator faults can be categorised into two types [97]:

i. Electrical faults:
   - Rotor electrical faults, defined by broken bars or end ring segments for squirrel-cage rotors and rotor winding open- or short-circuit and brushgear faults for wound rotor generators.
   - Stator faults, defined by stator winding open- or short-circuited.

ii. Rotor mechanical faults such as bearing damage, eccentricity, bent shaft or misalignment.

These failures may exhibit one or more of the following symptoms: disturbances in the current/voltage/flux, leading to unbalanced and harmonic line currents and consequent air-gap voltages, increased consequent harmonic torque pulsations, decreased average torque, excessive winding heating and increased losses or efficiency reduction [40], [64], [98]. All these effects are undesirable because they damage and reduce the reliability of the generator and the whole WECS.

Although bearing faults dominate total generator failures, as shown before in Fig. 2.5, the failures associated with rotor contribute significantly to the total generator failures, particularly in small size. These accounted for 12% of the total IG failures in larger MW range generators while exceeded 50% of failures in smaller MW scale machines. Due to these significant percentages, rotor fault diagnosis has received considerable attention during the last decades. Previous work, including [63], investigated the detection of rotor faults based on the known fault frequencies in the

stator current or power signal. However, understanding the influence of these failures on different WT generator control signals and utilising control signals to monitor the generator has received little attention and few papers have been published in this field. This research will focus initially on understanding the effect of rotor faults on the generator terminal and control variables for a modern WT-driven DFIG. Then, detection of faults is to be effected by applying frequency analysis to the control signals inside the RSI controller, particularly:

- *d*-rotor current error signal;
- *q*-rotor current error signal;
- *q*-rotor current signal.

The use of generator control loop signals for CM, compared to conventional techniques such as vibration monitoring, should have the following advantages:

- Reduced numbers of sensors;
- Electrical measurements are cheaper than mechanical measurements;
- Generator control signals are already available and can be easily accessed.

Common failures in an IG rotor cause rotor electrical asymmetry, which is considered in this research. This fault is generally represented as brush-gear or rotor winding open-circuit faults for the WRIG or DFIG, or broken rotor bars or cracked rotor end-rings for the squirrel cage induction generator (SCIG).

5.1.2 Rotor Electrical Asymmetry

Although rotor asymmetries do not initially cause a machine to fail, they can have serious secondary effects. For example in an SCIG, the broken bar faults may result in parts striking the stator windings at high velocity, causing serious stator winding damage to the IG [99]. The most serious effect of these faults may be that it is too costly to repair the rotor. However, this could be avoided, if the machine were supervised by an appropriate CM or diagnostic system. IG rotor faults generally start from a small fracture or high resistivity spot in the rotor winding. As such a fault increases the lack of induced currents in the rotor faulty section causes local saturation in stator and rotor teeth alongside the broken bars, a disproportional distribution of magnetic field and consequent asymmetrical air-gap magnetic field [100].

5.1.2.1 Causes of Rotor Electrical Asymmetry

A common reason for such failure is manufacture, such as defective casting or brazing, or thermo-mechanical activity over the machine life. Another general reason is over current, for example due to a single or successive rotor stalls, but there can be various reasons that will lead to failure [101], [102]:

- Thermal stresses due to thermal overloading of the machine, non-uniform heat distribution, hot spots, or excessive losses, sparking, mainly in cast rotors;
- Magnetic stresses due to electromagnetic forces, electromagnetic noise and vibration;
- Residual stresses from manufacture;
- Dynamic stress due to rotor axial torque and centrifugal forces;
- Environmental stresses caused by contamination and abrasion of rotor material due to chemicals or humidity;
- Mechanical stresses due to bearing damage or fatigued parts.

5.1.2.2 Basic Derivation of Electrical Frequency

The sequence of electromagnetic and mechanical phenomena due to the rotor asymmetry in the stator and the rotor of an induction machine that causes the current components were explained in [37], [68] and [103]. In a balanced and healthy machine, the symmetrical stator circuit generates the rotating magnetic field at frequency (f), which produces *e.m.f* in the rotor windings at frequency (sf). The presence of a rotor asymmetry leads to unbalanced rotor currents, which causes a reverse rotating magnetic field, related to a rotor inverse current sequence component at frequency ($-sf$). The rotor current (i_r) waveform can be written as:

$$i_r(t) = a\cos(2\pi\, sft + \emptyset_a) + b\cos(2\pi\,(-sf)t + \emptyset_b) \qquad 5.1$$

where a and b are the component magnitudes and $\emptyset$ is the component phase angle. Consequently, these positive and inverse sequence is reflected on the stator side and induce *e.m.f* with frequencies f & $(1-2s)f$ and the stator current (i_s) becomes:

$$i_s(t) = A\cos(2\pi\, ft + \emptyset_A) + B\cos(2\pi\,(1-2s)ft + \emptyset_B) \qquad 5.2$$

where A and B are the component magnitudes. The arising $(1-2s)f$ harmonic component in the stator interacts with rotor current of frequency ($-sf$). This harmonic

also interacts with the fundamental magnetic flux $\psi\cos(2\pi ft + \emptyset_\varphi)$ and produces the oscillatory torque at frequency $2sf$.

$$\Delta T_g(t) = 3p\psi B\sin(4\pi sft + (\emptyset_\varphi - \emptyset_B)) \quad 5.3$$

and then to speed ripple results as follows:

$$\Delta\omega_{rm}(t) = \frac{1}{J_g}\int \Delta T_g(t)dt = -\frac{3p\psi B}{4\pi sfJ_g}\cos(4\pi sft + (\emptyset_\varphi - \emptyset_B)) \quad 5.4$$

where p is the number of pole pairs, J_g is the generator inertia and the displacements are referred to the fundamental current components. The rotor speed variation gives rise to a further distortion in the stator variables. The rotor speed variation is seen by the stator as a mechanic angular variation and can be computed by rotor speed integration as:

$$\int \Delta\omega_{rm}(t)dt = -\frac{3p\psi B}{4(2\pi sf)^2 J_g}\sin(4\pi sft + (\emptyset_\varphi - \emptyset_B)) \quad 5.5$$

This angular variation causes a phase modulation in the stator flux that becomes:

$$\begin{aligned}\varphi_s(t) &= \psi\cos(2\pi sf + \emptyset_\varphi - \frac{3p\psi B}{4(2\pi sf)^2 J_g}\sin(4\pi sft + (\emptyset_\varphi - \emptyset_B))) \\ &= \frac{3p^2\psi^2 B}{8(2\pi sf)^2 J_g}[\cos\big(2\pi(1-2s)ft + \emptyset_\varphi\big) - \cos\big(2\pi(1+2s)ft + (2\emptyset_\varphi - \emptyset_B)\big)] \quad 5.6\end{aligned}$$

These fluxes induce in the stator windings two *e.m.fs* at frequencies $(1 \pm 2s)f$. The $(1-2s)f$ causes a stator current component which interacts with rotor current of frequency $(-sf)$. The other component $(1+2s)f$ will cause a rotating magnetic field at frequency $3sf$ with respect to the rotor. Due to rotor asymmetry, the rotor currents induced by the resultant rotor *e.m.f* generate two rotating fields at frequencies $\pm 3sf$.

$$\begin{aligned}i_s(t) &= A\cos(2\pi ft + \emptyset_A) + B\cos(2\pi(1-2s)ft + \emptyset_B) \\ &+C_1\cos(2\pi(1-2s)ft + \emptyset_B + \emptyset_C) + C_2\cos\big(2\pi(1+2s)ft + 2\emptyset_\varphi - \emptyset_B + \emptyset_C\big) \quad 5.7\end{aligned}$$

$$\begin{aligned}i_r(t) &= a\cos(2\pi sft + \emptyset_a) + b\cos(2\pi(-sf)t + \emptyset_b) + c_1\cos(2\pi(-sf)t + \emptyset_b + \emptyset_c) \\ &+c_2\cos(2\pi(3s)ft + \emptyset_b + \emptyset_c) + d_1\cos(2\pi(-3s)ft + +\emptyset_b + \emptyset_c + \emptyset_d) \quad 5.8\end{aligned}$$

The consequence of these phenomena continues for every different frequency flux variation. The interaction process and the reflected harmonics due to rotor dissymmetry can be summarized as shown in Fig. 5.1. Note that these harmonics have less effect in the speed and the torque than the stator and rotor currents due to the generator inertia which react to damp and absorb these harmonics.

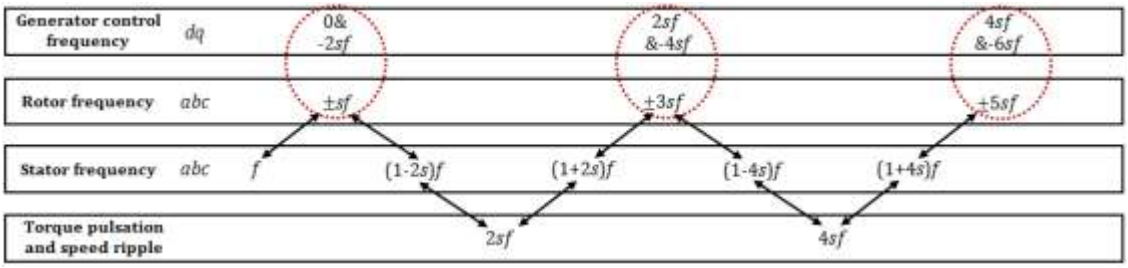

Fig. 5.1: Frequency propagation of rotor electrical asymmetry in different generator & control variables

This process gives rise to stator and rotor current components at frequencies $(1 \pm 2ks)f$ with $k = 0,1,2,3,\ldots$ and $\pm lsf$ with $l = 1,3,5,7,\ldots$, respectivetly. Therefore, both Eqs. 5.7and 5.8 can be developed and rewritten as:

$$i_s(t) = A_0 \cos(2\pi ft + \emptyset_{s_0}) + \sum_{k=1}^{\infty} A_{\pm 2k} \cos(2\pi (1 \pm 2ks)ft + \emptyset_{s_{\pm 2k}}) \quad 5.9$$

$$i_r(t) = a_1 \cos(2\pi s ft + \emptyset_{r_1}) + a_{-1} \cos(2\pi(-s f)t + \emptyset_{r_{-1}})) + \sum_{\substack{l=3 \\ l\ is\ odd}}^{\infty} a_{\pm l} \cos(2\pi (\pm ls)ft + \emptyset_{r_{\pm l}}) \quad 5.10$$

According to Eq. 5.10, the rotor faulty harmonics will be transferred into RSI control loop signals and are expected to produce a relevant harmonic in the spectrum of the actual *d*- and *q*-rotor. In this case, both of the actual *d*- and *q*-rotor current waveforms can be written as:

$$i_{dr}(t) = I_{dr_0}(t) + \sum_{m=1}^{\infty} I_{dr_{\pm 2m}} \cos(2\pi (\pm 2ms)ft + \emptyset_{dr_{\pm 2m}}) \quad 5.11$$

$$i_{qr}(t) = I_{qr_0}(t) + \sum_{m=1}^{\infty} I_{qr_{\pm 2m}} \cos(2\pi (\pm 2ms)ft + \emptyset_{qr_{\pm 2m}}) \quad 5.12$$

where I_{dr_0} and I_{qr_0} are the fundamental harmonics of *d*- and *q*-rotor currents, respectively, $m = 1,2,3,\ldots$. Extracting the frequency components from the above equations we see that rotor electrical asymmetry results in actual *d*- and *q*-rotor current harmonic components at $\pm 2msf$. By subtracting Eq. 5.11 from the *d*-rotor reference current and Eq. 5.12 from the *q*-rotor reference current, the instantaneous values of the error signals inside PI control loops are:

$$\mathcal{E}_{i_{dr}}(t) = i_{dr\,ref}(t) - I_{dr_0}(t) - \sum_{m=1}^{\infty} I_{d_{\pm 2m}} \cos(2\pi (\pm 2ms)ft + \emptyset_{dr_{\pm 2m}}) \quad 5.13$$

$$\mathcal{E}_{i_{qr}}(t) = i_{qr\,ref}(t) - I_{qr_0}(t) - \sum_{m=1}^{\infty} I_{q_{\pm 2m}} \cos(2\pi (\pm 2ms)ft + \emptyset_{q_{r\pm 2m}}) \quad 5.14$$

In a steady state operation conditions, $i_{dr\,ref}(t) \cong I_{dr_0}(t)$ and $i_{qr\,ref}(t) \cong I_{qr_0}(t)$. Therefore, the expressions of Eq. 5.13 and Eq. 5.14 can be expressed as:

$$\mathcal{E}_{i_{dr}}(t) \cong \sum_{m=1}^{\infty} I_{dr_{\pm 2m}} \cos(2\pi\,(\pm 2ms)ft + \emptyset_{dr_{\pm 2m}}) \qquad 5.15$$

$$\mathcal{E}_{i_{qr}}(t) \cong \sum_{m=1}^{\infty} I_{qr_{\pm 2m}} \cos(2\pi\,(\pm 2ms)ft + \emptyset_{qr_{\pm 2m}}) \qquad 5.16$$

From Eq. 5.15 and Eq. 5.16, the remaining error signals can be expected to mainly contain the fault existence harmonics at frequencies ($\pm 2msf$). Furthermore, the spectra of these signals are expected to give better evidence of asymmetry than other electrical signals, such as stator current and total power, due to:

- Faulty harmonics dominate the whole error signal spectra, while 50Hz and 0Hz components dominate the stator current and total power spectra, respectively;
- They suggest easy fault detection ability for the DFIG even at synchronous speed, whilst that is difficult using the stator current and total power;
- Monitoring line or phase stator current only gives information about the specific phase or line being measured, while monitoring total power increases the number of transducers and the consequent noise. However, monitoring the control error signals can offer an equal contribution from all phases and minimize costly transducers and data processing.

In this research, the attention will be focused only on the investigation of the $2sf$ faulty component amplitude inside the control error signals for *d*- and *q*-axes as well as the *q*-rotor current. However, the *d*-rotor current is not considered further in this investigation because it is equal to the *d*-rotor error current ($i_{dr}(t) = \mathcal{E}_{i_{dr}}(t)$), due to the control strategy ($i_{dr\,ref}(t) = 0$) used. Furthermore, the spectra of the proposed signals will be compared with the spectra of the stator current at $(1-2s)f$ and the total power at $2sf$.

5.1.2.3 Fault Representation

In order to test several practical WECS IG fault situations, it is necessary to realize fault situations similar to reality. Faults which damage one or more rotor winding or brush-gear circuits have the effect of increasing faulty phase resistance and unbalancing rotor circuit resistances. Therefore, the rotor electrical asymmetries can be practically modelled in the generator by inserting an additional resistance in series to the phase rotor windings. In this research, the 3-phase rotor resistances of the experimental

Durham Test Rig generator were increased by external variable resistors connected into the rotor circuit via the machine slip rings, as shown in Fig. 5.2. These resistors were introduced to increase the balanced phase resistance of the rotor and apply small asymmetry in a controllable fashion.

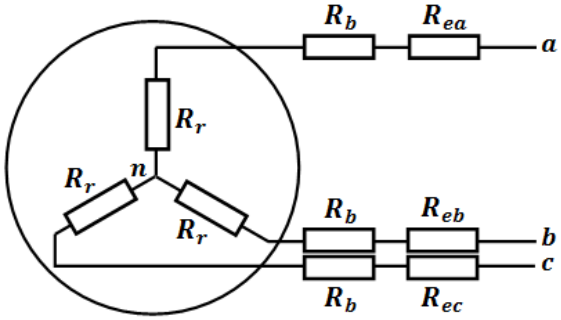

Fig. 5.2: Rotor asymmetry by the insertion of additional resistances

From this figure, the total resistance in each rotor phase (R_{ra}, R_{rb}, R_{rc}) can be calculated as:

$$\begin{aligned} R_{ra} &= R_r + R_b + R_{ea} \\ R_{rb} &= R_r + R_b + R_{eb} \\ R_{rc} &= R_r + R_b + R_{ec} \end{aligned} \tag{5.17}$$

where R_r and R_b are the rotor internal and brushgear phase resistors, respectively. R_{ea}, R_{eb} and R_{ec} are the three external resistors. Therefore, the balanced rotor circuit ($R_{rah} = R_{rbh} = R_{rch}$) is only given when

$$R_{ea} = R_{eb} = R_{ec} \tag{5.18}$$

From Eq. 5.18, the rotor electrical asymmetry can be introduced when at least one of the external resistors has higher value compared with the other. So, assuming the fault to be in phase *a* of the rotor circuit, then the unbalanced condition in this case is given by:

$$R_{raf} > (R_{rbh} = R_{rch}) \tag{5.19}$$

and

$$R_{ea} = R_{eb} + \delta R = R_{ec} + \delta R \tag{5.20}$$

where δR is the increase of the rotor resistance due to the fault existence, or rotor asymmetry. Since the rotor circuit is star connected, the absolute experimental electrical unbalance can be estimated by calculating:

$$\delta R = \left| R_{raf} e^{j\theta_a} + R_{rbh} e^{j\theta_b} + R_{rch} e^{j\theta_c} \right| \quad 5.21$$

where $j = \sqrt{-1}$, $\theta_a = 0, \theta_b = \frac{2\pi}{3}$ and $\theta_c = \frac{4\pi}{3}$. For clarity, the rotor resistance is given as a percentage of the balanced phase resistance so that the rotor asymmetry, ΔR, in percent, is given by:

$$\Delta R(\%) = \frac{\delta R}{R_{rah}} \times 100 = \frac{\delta R}{R_{rbh}} \times 100 = \frac{\delta R}{R_{rch}} \times 100 \quad 5.22$$

In the same way, the rotor asymmetry also was applied to the MATLAB model of the Test Rig.

5.2 Signal Processing

Many signal processing techniques have been introduced in CM for WT diagnostic and prognostic systems over last years. These techniques mainly depend on the types of data and components studied. For electrical signals, the data are usually analyzed from time domain into frequency domain where the particular frequency components corresponding to the fault can be identified. As mentioned in Chapter 2, this analysis can be performed using different techniques such as FFT analysis, cepstrum analysis and bispectrum analysis. Among these techniques, the FFT analysis is the most commonly used. Furthermore, the FFT is the basis for many advanced signal processing techniques. During the research, the FFT was applied to analyse the proposed control signals as well as the stator current and total power. In this section, the principle of the FFT is introduced. This included introduction to the Fourier transform and its development into the discrete Fourier transform (DFT) and then the FFT.

5.2.1 Fourier Transform

The Fourier theorem states that any waveform can be duplicated by the superposition of a series of sine and cosine waves. As an example, the following Fourier expansion of sine waves provides an approximation of a square wave as shown in Fig. 5.3. The square wave is shown as a blue line over two periods. The four curves in the red colour of the plot show the first term, two terms, three terms and four terms in the Fourier expansion. As more terms are added the superposition of sine waves better matches a square wave.

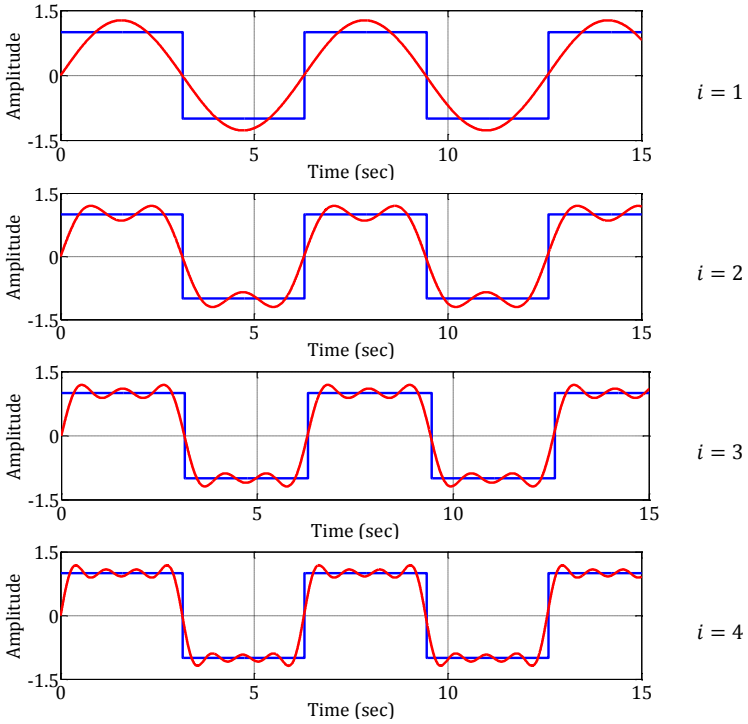

Fig. 5.3: Fourier series approximation of square wave & number of Fourier terms indicated

The Fourier Transform uses the above concept to convert the time description of the continuous waveform $x(t)$ into an equivalent function in frequency by:

$$X(f) = \int_{-\infty}^{\infty} x(t)\, e^{j2\pi ft} df \qquad 5.23$$

where $X(f)$ is the Fourier Transform that gives the frequencies at which the signal is non-zero and e denotes the natural exponent and is defined by:

$$e^{j2\pi f} = \cos(2\pi ft) + jsin(2\pi ft) \qquad 5.24$$

In addition, the original signal $x(t)$ can be obtained from the frequency domain signal $X(f)$ by taking the inverse Fourier Transform as following:

$$x(t) = \int_{-\infty}^{\infty} X(f)\, e^{j2\pi ft} dt \qquad 5.25$$

However, experimental data usually consists of discrete data points rather than a continuous function as used in the equations above. For the data sequence $x(n)$ of signal $x(t)$ with total number of samples N, the discrete Fourier Transform (DFT) can be calculated by:

$$X(k) = \sum_{n=0}^{N-1} x(n) e^{-j\frac{2\pi nk}{N}} \quad , k = 0, 1, \dots, N-1 \qquad 5.26$$

where $X(k)$ is the DFT. The disadvantage of the DFT technique is that it requires each harmonic to be calculated separately, which requires much more processing power. Moreover, the DFT is an order N^2 calculation, meaning that the number of multiplications is equal to the square of the number of data points. For thousands of data there will be millions of multiplications and additions that need a lot of memory, time and cost. Therefore, a large amount of work has been devoted to reducing the computation time of a DFT. This has led to efficient method which is known as the Fast Fourier transform (FFT).

5.2.2 Fast Fourier Transform

The FFT are efficient algorithms for calculating the DFT. The central insight which leads to this method is the realization that the DFT of a sequence of N points can be written in terms of two DFT of length $N/2$. Thus if N is a power of two, it is possible to recursively apply this decomposition until we are left with DFT of single points. Eq. 5.26 can be rewritten as:

$$X(k) = \sum_{n=0}^{N-1} x(n) W_N^{nk}, k = 0, 1, \dots, N-1 \quad 5.27$$

and $$W_N^{nk} = e^{-j\frac{2\pi nk}{N}} \quad 5.28$$

It is easy to realize that the same values of W_N^{nk} are calculated many times as the computation proceeds. With divide the data sequence $x(n)$ into equal even and odd sequences as:

$$x(2n) = x(0), x(2), \dots \dots, x(N-2) \quad 5.29$$

$$x(2n+1) = x(1), x(3), \dots \dots, x(N-1) \quad 5.30$$

Then, Eq. 5.27 can rewritten as:

$$X(k) = \sum_{n=0}^{\frac{N}{2}-1} x(2n) W_N^{2nk} + \sum_{n=0}^{\frac{N}{2}-1} x(2n+1) W_N^{(2n+1)k} \quad 5.31$$

Since $$W_N^{2nk} = e^{-j\frac{4\pi nk}{N}} = e^{-j\frac{2\pi nk}{N/2}} = W_{\frac{N}{2}}^{nk} \quad 5.32$$

$$W_N^{(2n+1)k} = W_N^k . W_{\frac{N}{2}}^{nk} \quad 5.33$$

By substituting Eqs. 5.32 and 5.33 into Eq. 5.31, the FFT algorithm becomes:

$$X(k) = \sum_{n=0}^{\frac{N}{2}-1} x(2n) W_{\frac{N}{2}}^{nk} + W_N^k \sum_{n=0}^{\frac{N}{2}-1} x(2n+1).W_{\frac{N}{2}}^{nk} \qquad 5.34$$

Thus the N-point DFT can be obtained from two $N/2$-point transforms, one on even input data, and one on odd input data. Figure below shows the application of the FFT analysis for pulse wave signal.

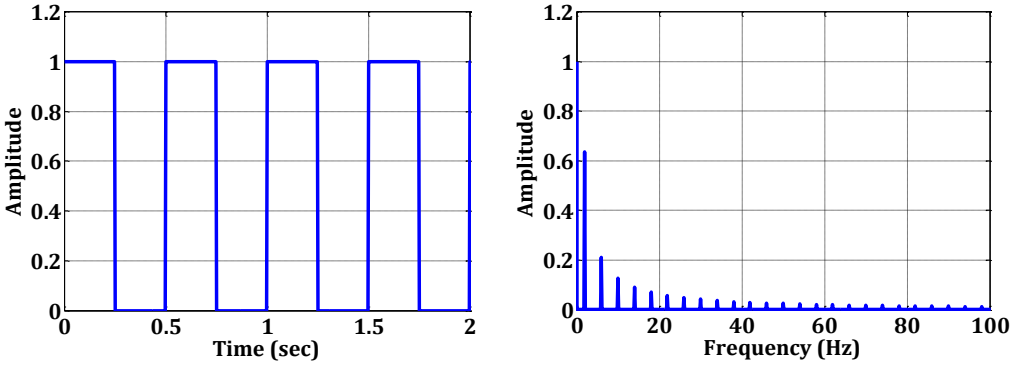

Fig. 5.4: Pulse wave signal & its FFT spectrum

The FFT significantly reduces redundancies and take much less time. The order of this calculation is $Nlog_2N$. For example, a data of 1024 samples, the DFT takes 1,048,576 computations to calculate the harmonics while the FFT takes 10,240 computations. The FFT is over 100 times faster. Furthermore, the FFT is a method of calculating harmonics not one at a time, but as a group. The FFT however requires N to be a power of two (Binary number). If the length of data set is not a power of two, it must be padded with zeros up to the next power of two.

Today, there are many internet locations and types of software which can provide FFT subroutines in different programming languages, from Fortran to C++. Therefore, there is no need to write the FFT routine. For FFT analysis in this research, the author has used the MATLAB command "fft(x,N)", where x is the recorded N-element time array. A simple m-file is included in Table 5.1, which computes and plots the normalized FFT spectrum of discrete time domain signal $x(n)$. This program is used in this research to calculate the results which are presented in Chapter 6. Note that all the time domain simulated and measured signals used in this research have been discretised with sampling rate of 5kHz which is greater than twice the highest frequency of the time record (Nyquist sampling criterion). In order to avoid zero padding, the m-file was written to modify the actual length of chosen data to be 2^m. For example, most of the chosen data to be analyzed during this research has initial length of 50,000 samples

(10sec) or $2^{15.6}$. This length is modified by the m-file to be only 2^{15} and then the data will be reduced to 32,768samples (6.5sec).

Table 5.1: MATLAB module for normalized FFT calculations

```
% Read the time vector data sequence x(n) from the MATLAB workspace
   y1=x;
% Define the data sample location and the sampling frequency for FFT
analysis
   N1=input ('N1 =  ');          % Number of first sample
   N2=input ('N2 =  ');          % Number of last sample
   Fs=input('Fs=  ');            % Sampling frequency [Hz]
% Calculate the normalized FFT spectrum [dB]
   y2=y1(N1:N2,1);
   Na=N2-N1+1;                   % Actual length of data
   N3=log2(Na)
   N4=fix(N3)
   Nm=2^N4                       % Modified length of data

   f=Fs/Nm*(0:1:Nm/2);           % Frequency vector
   Y1=fft(y2,Nm)/Nm;             % Take FFT
   Y2 =2*abs(Y1(1:Nm/2+1));      % Take the magnitude of single-sided
                                 FFT spectrum
   Max_Y2=max(Y2);               % Take the maximum magnitude in the
                                  FFT spectrum
   Y3=10*log(Y2(:,1)./Max_Y2);   % Take the normalized FFT spectrum
                                 [dB]
% Generate the plot, title and labels
   figure (1);
   plot(f,Y3);
   title('Faulty condition');
   xlabel('Frequency (Hz)');
   ylabel('Amplitude (dB)');
   grid on;
```

.

6 Application & Results

6.1 Introduction

As introduced in Chapter 5, the rotor electrical asymmetry in the DFIG may be caused by a number of different fault conditions including a coil open circuit or brush-gear faults. The presence of either of these faults in one rotor phase will lead to a resistance increase for that phase producing an unbalance of the three rotor phase circuit. Therefore such faults can be emulated in the Test Rig by introducing an additional resistance into one rotor phase of the Test Rig generator rotor winding circuit.

In this work, the rated rotor phase resistance of the generator, in both the physical Test Rig and the MATLAB model, are 0.044Ω. In order to increase the balanced rotor phase resistance and model the fault simply, the healthy DFIG phase resistance was increased to 0.235Ω per phase, by introducing an external variable resistance, and adding δR to one phase to represent the unbalanced condition. While acceptable levels of DFIG rotor unbalance have not yet been defined in the literature, the unbalance levels represented and investigated during the research were reasonable for the emulation of faulty rotor unbalance, based on experience [104]. A reasonable percentage unbalance of the rotor winding to represent a fault could be 10-20%.

In order to verify the proposed detection method, several tests were carried out on the physical Test Rig and its MATLAB model under healthy and faulty conditions. During these tests, the Rig was run at variable and fixed speed operating conditions, to represent respectively the condition of the WT generator under either varying power, that is BRWS, or fixed rated power, that is ARWS. The analysis is achieved by comparing the harmonic spectra of stator current and power with the proposed control signals, namely; *q*-rotor current, *d*- and *q*-rotor current errors. However, these spectra were obtained by taking the sum of the side-band harmonic magnitudes on the positive and negative side of each considered centre frequency and presenting them together. For the Test Rig 4-pole DFIG, the frequencies of specific rotor fault components in the signal spectra will vary, as a function of slip and supply frequency, as illustrated in Table 6.1

Table 6.1: Rotor electrical asymmetry frequency of interest for 4-pole DFIG

Signal type	Frequencies of interest	Frequency range
Stator current	$(1-2s)f$	20~80Hz
Stator power	$\pm 2sf$	0~30Hz
d- and q-rotor current errors	$\pm 2sf$	0~30Hz
q-rotor current	$\pm 2sf$	0~30Hz

The sensitivities of these signals, in detecting faults, have been examined with respect to:

- Fault levels;
- Generator speed;
- Control parameter values. However, the generator PI control parameter values should be fixed and the probability of change is low.

All the harmonic spectra were obtained by applying an FFT algorithm to the instantaneous values of the monitored variables, sampled at 5kHz. To simplify the result presentation, all signal spectra were normalized setting at 0 dB the highest harmonic component amplitude for each spectrum. This depends upon the signal type and the operating condition.

As mentioned in section 3.1.1, all the results included in this research were obtained from the Test Rig with the GSI disconnected and using the batteries. However, due to the rating current limitation of the DC Link batteries the DFIG could not, for CM purposes, be operated experimentally over its full variable speed range. Fig. 6.1 below shows the operating region of the closed loop DFIG Test Rig with the stator voltages and DC Link batteries used in this research.

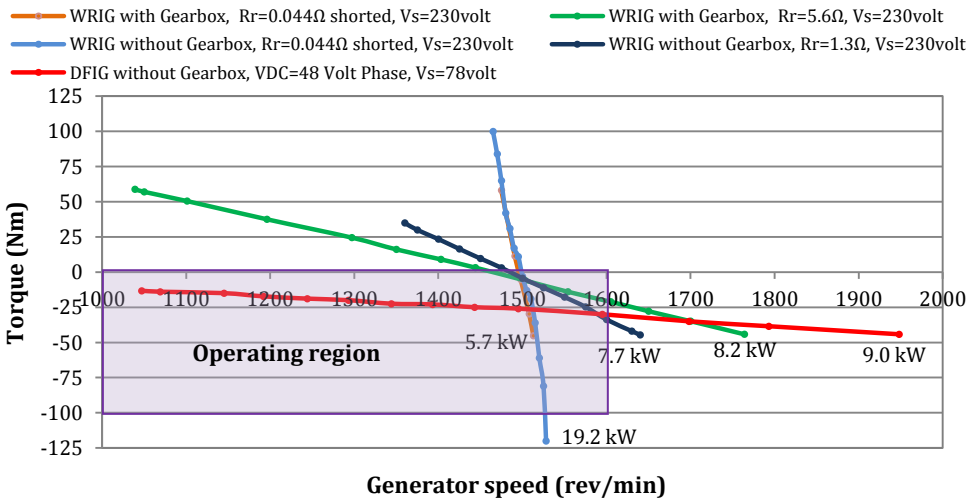

Fig. 6.1: Test Rig operating region

6.2 Fixed Speed Operation

As it is known, the WT-driven DFIG can operate over a slip range up to ±30% and thus enable the turbine to extract the maximum power from the wind with variable operating speeds. Once the turbine reaches its rated speed, the pitch control is employed to limit the power to its rated power and the turbine operates at fixed speed. At this point, the DFIG speed is generally around 30% above its synchronous speed. Due to the battery current limitation, the Test Rig was operated, in both the healthy and faulty conditions, up to its maximum speed of 1600rev/min, representing the fixed speed operation of a variable speed WT ARWS. The time waveform of the generator rotational speeds in both simulation and measured environments are shown in Fig. 6.2. From this figure, it can be seen that there was a small variation about (5rev/min) in the measured speed due to grid voltage variations and frequency variations around 50Hz. The simulated and measured time waveform of the resultant control signals, stator current and total power signals are presented in Appendix C. Additional resistance of 0.047Ω was successively added to one phase of the rotor winding circuit to create a rotor unbalance of 20%, according to Eq. (5.22).

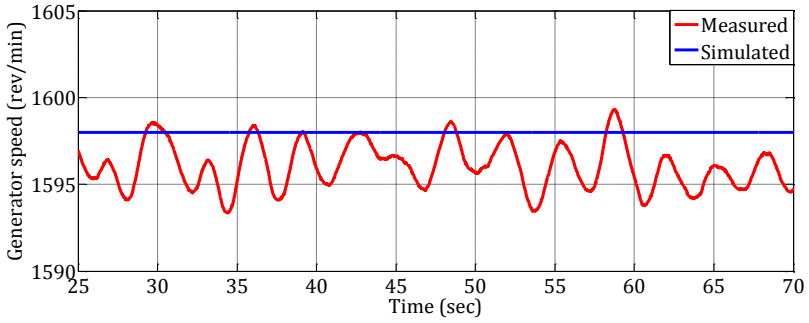

Fig. 6.2: Generator speeds during fixed speed simulated & measured tests

6.2.1 Simulation Results

To identify consistent spectral signatures for different operating conditions, the spectral fault signature of rotor fault in DFIG steady-state and control signals was investigated by comparing the data simulated on the MATLAB model of the Test Rig for balanced and unbalanced rotor operations. These simulations were carried out operating the model in a noise-free environment using a fixed supply frequency of 50.0Hz.

A typical set of simulated healthy and faulty stator current and total instantaneous power spectra are shown, respectively, in Fig. 6.3a to 6.3d. These results are based on analysing data of 34-44sec. Only one phase current signal is presented and analysed here, as is usually the case for MCSA. The healthy current spectrum in Fig. 6.3a indicates the fundamental harmonic at 50.0Hz while the power spectrum in Fig. 6.3c indicates the fundamental harmonic at 0.0Hz or DC. Fig. 6.3c also shows a set of small harmonics in the power at 19.3Hz, 38.6Hz, 58.0Hz, 77.3Hz and 96.6Hz produced by the reflection of the rotor harmonics into the stator. The rotor harmonics are initially produced as a result of the generated six-step rotor voltage waveform by the RSI, as shown in Fig 4.8, and occur at frequency $\pm(6n \pm 1)sf$. They are then reflected on the other generator signals to reproduce other harmonic at $\pm(6ns \pm 1)f$ in the stator current signals and $\pm 6nsf$ in the power and the control current signals. However, these harmonics are not visible in the healthy stator current spectrum because their values are very small. Moreover, the component of the negative frequencies for all spectra, presented in this research, were added to the positive frequency components and plotted on the positive side.

The simulated faulty stator current given in Fig. 6.3b indicates that rotor unbalance induces a change of considerable magnitude in a frequency around 56.5Hz with magnitude of -66.0dB. An indication of fault spectral signature is also presented in the faulty DFIG total power spectrum in Fig. 6.3d, where there is a clear increase in the magnitude of the dominant fault-related component up to -71.0dB at 6.5Hz. By comparing Fig. 6.3b and 6.3d, despite the current faulty component has higher value than the power, the fault existence is more clearly in the power spectra than the stator current.

Fig. 6.3e to 6.3j demonstrate the control loop current signals spectra corresponding to healthy and faulty conditions. As in the healthy power spectra, a set of tiny harmonics are clearly visible in the three healthy spectra at 19.3Hz, 38.6Hz, 58.0Hz, 77.3Hz and 96.6Hz as a results of the rotor switching harmonics. Also, these spectra show the fundamental harmonics appear at 0.0Hz with magnitude values 0.0dB in the healthy condition. However, the faulty spectra, shown in Fig. 6.3f, 6.3h and 6.3j indicate a significant rise in magnitude of spectral component at 6.5Hz. This component has magnitude of 0.0dB in both current error spectra while it around -71.0dB in the q-rotor current spectrum. Notice that, both fault components of the total power and q-rotor current spectra have the same value due to the control scheme used, based on the stator flux oriented vector explained in Chapter 4. More importantly, the comparison of faulty data of all signals shows that the faulty components in the current error signals, as

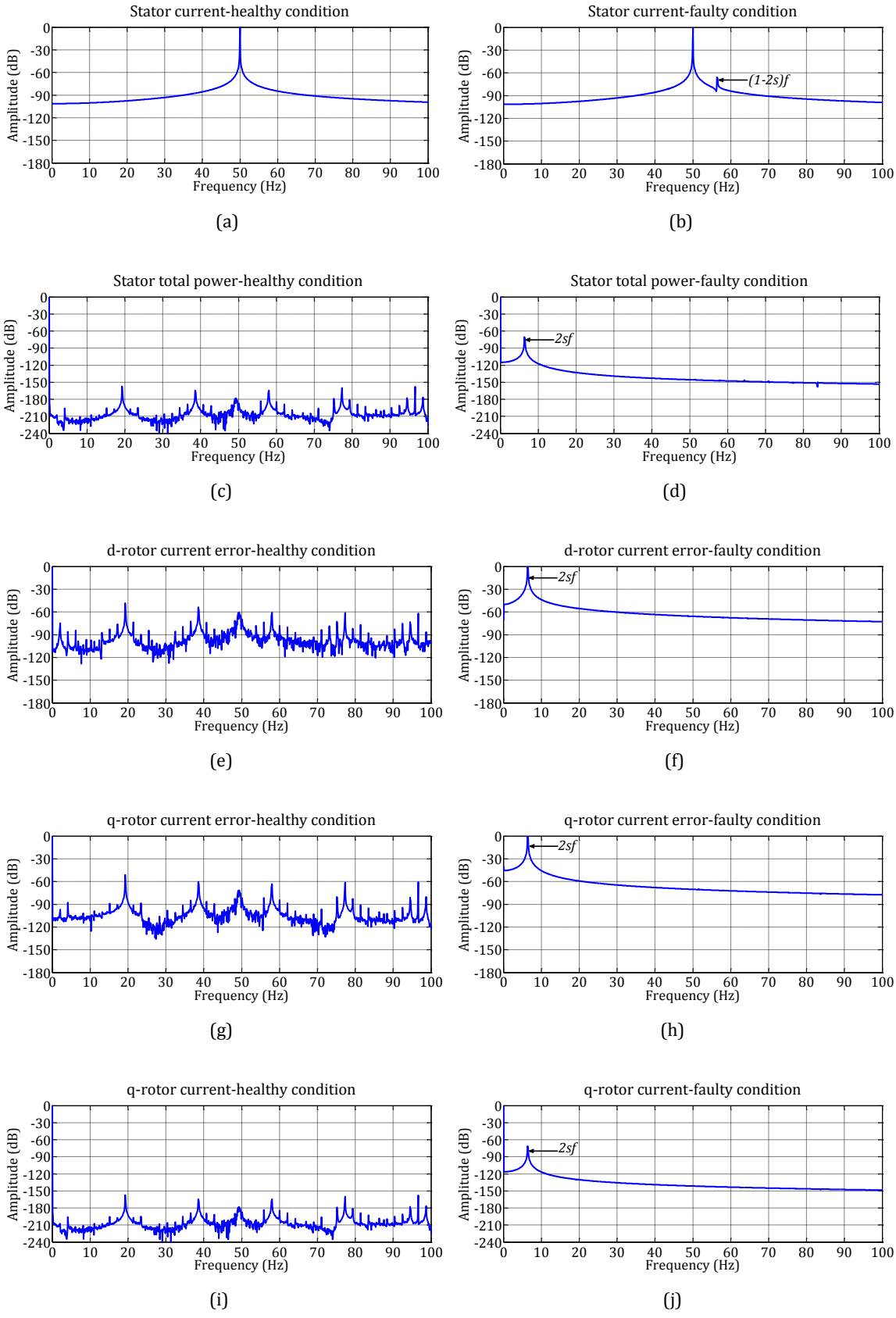

Fig. 6.3: DFIG & RSI control signal spectra simulated at fixed speed ≃1598rev/min

expected, dominate their spectra and have higher magnitudes than other signals. This gives the advantage to the current error control signal over the *q*-rotor current, stator current and power for fault detection, as the fault-frequency can be more easily observed and detected in this signal. Therefore, the simulation suggests that the proposed CM technique should be based upon monitoring the current error control signal as an interesting alternative diagnostic index for detecting rotor faults.

6.2.2 Measured Results

As in the simulation, the stator current, total power and control signals were collected from the physical Test Rig with the rotor circuit either balanced or unbalanced. The data differ, however, in the general noise levels, with measurements exhibiting a higher noise levels compared to the noise-free simulation environment. The measured healthy and faulty DFIG stator current and power spectra are shown in Fig. 6.4a to 6.4d. From these figures, the harmonic related to the fault presence is located at 56.0Hz with a magnitude of -46.7dB in the current and at 6.0Hz with -60.4dB in the power.

For the control signals, a clearer indication of fault spectral signature are obtained by comparing measured healthy and faulty current error spectra given in Fig. 6.4e to 6.4h. There is a clear increase in the magnitude of the fault-related components at 6.0Hz with significant magnitudes -28.0dB and -22.2dB for *d*- and *q*-error signals, respectively. However, comparing with the simulation results in Fig. 6.3f and 6.3h, it can be seen that these magnitudes were dropped and not the highest values in both spectra due to the large amplitude of both spectra at 100.0Hz. These harmonic is resulting from the stator fault where it was found during this research that the DFIG has a magnetising unbalance in the stator windings contributed by a little grid voltage unbalance.

Fig. 6.4i and 6.4j show the measured spectra of *q*-rotor current for balance and fault operations. It can be seen that the fault-frequency is visible at 6.0Hz with amplitude -61.0dB and again it is similar to the fault-frequency obtained from the power spectra.

These experimental results have, for steady state operation, confirmed the simulation observations in the previous section that the fault-frequency within the stator current is less visible than other signals monitored. The *q*-rotor current gives the same results as the total power in rotor fault detection. However, the current error control

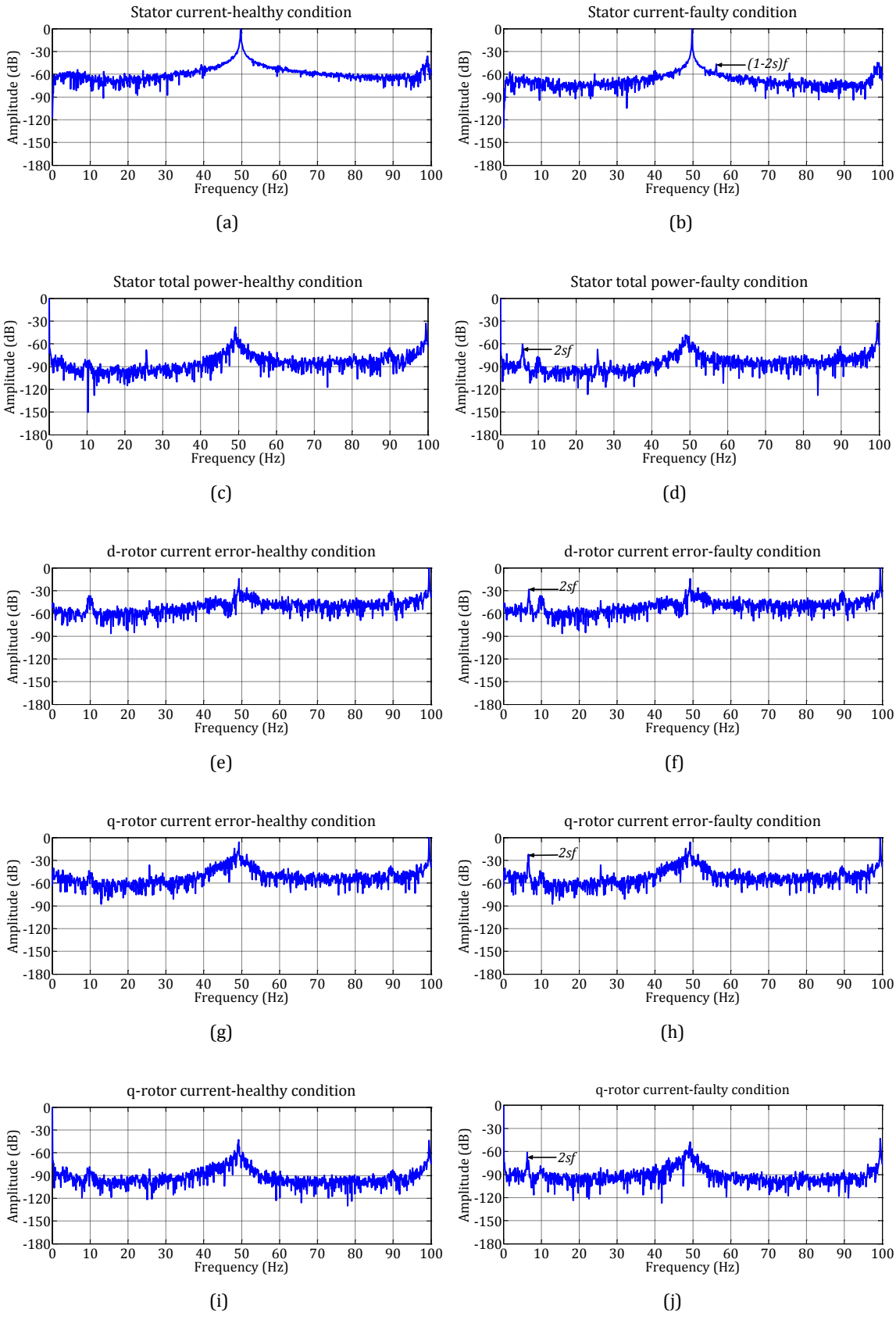

Fig. 6.4: DFIG & RSI control signal spectra measured at fixed speed ≃1598rev/min

signal, with comparative advantage to the q-axis control signal, still contains a faulty frequency component ($2sf$) higher than any other signals used in this research. Therefore, the measurements confirm that a CM technique based upon monitoring the current error control signals will be an interesting alternative diagnostic index for detecting rotor faults. It has the potential to detect incipient electrical asymmetry on a WT DFIG, since the magnitude of the characteristic harmonic frequency can be easily detected better than stator current and power.

6.3 Variable Speed Operation

Following successful rotor fault detection using the current error control signal in fixed speed operation, attention is now turned to analysis of these signals under variable speed conditions, as would occur in a variable speed WT at wind speeds below the rated speed, where the turbine speed varies according to the torque applied to the DFIG.

To represent operation in a real variable speed WT with a DFIG, both simulated and measured systems were run for a period of 210sec below synchronous speed with a driving condition based on a wind record at 7.5m/sec and 6% turbulence. The resultant generator speeds are shown in Fig. 6.5. Again, the simulated speed was smoother than the measured speed which had small variations due to the grid frequency and voltage deviations. As before, data was recorded for conditions where the rotor was balanced and 20% unbalanced. All the spectra presented were calculated from data collected from 150sec to 160sec with 12rev/min speed variation in the simulated and measured cases. However, more results obtained under other different variable speed operation are presented in Appendix C.

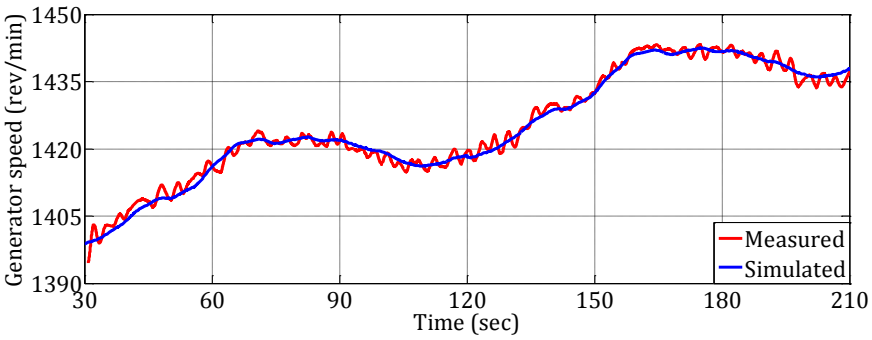

Fig. 6.5: Generator rotational speed signal during simulated & measured variable speed tests

6.3.1 Simulation Results

The simulated results for rotor fault detection under variable speed operation, shown in Fig. 6.5, are presented in Fig. 6.6a to 6.6j. As for fixed speed, the spectra show that a new harmonic component appears as the fault is introduced.

For the stator current the fault-frequency is visible at frequency 46.0Hz with a normalized magnitude -66.0dB, Fig. 6.6b.

The total power spectrum with balance rotor circuit is shown in Fig. 6.6c. There is, however, a clear increase in spectral content in the healthy power data compared healthy power spectrum, in Fig. 6.3c, of fixed speed due to the transient conditions with speed changes. After the rotor imbalance was applied, the power spectrum in Fig. 6.6d demonstrates the fault-frequency component rise at 4.0Hz and normalized magnitude -71.0dB.

The control current signal spectra under healthy and faulty conditions were also evaluated for variable speed operation and the results presented in Fig. 6.6e to 6.6j. As in the power spectrum, due to the transients in the three control signal responses their healthy spectra illustrate rise the spectral content compared with the fixed speed results. Even the component $2sf$ in the presence of the fault can be observed from the q-rotor current spectrum in Fig. 6.6j at 4.0Hz with -71.0dB, its normalized magnitude has bigger value with 0dB in the current error spectra as shown in Fig. 6.6f and 6.6h. Furthermore, the fault-frequency still dominates both current error spectra as in the fixed speed operation. Therefore, despite the frequency analysis of stator current, power and q-rotor current are valid for rotor fault detection, the d- and q-rotor current error signals can be considered as more attractive method.

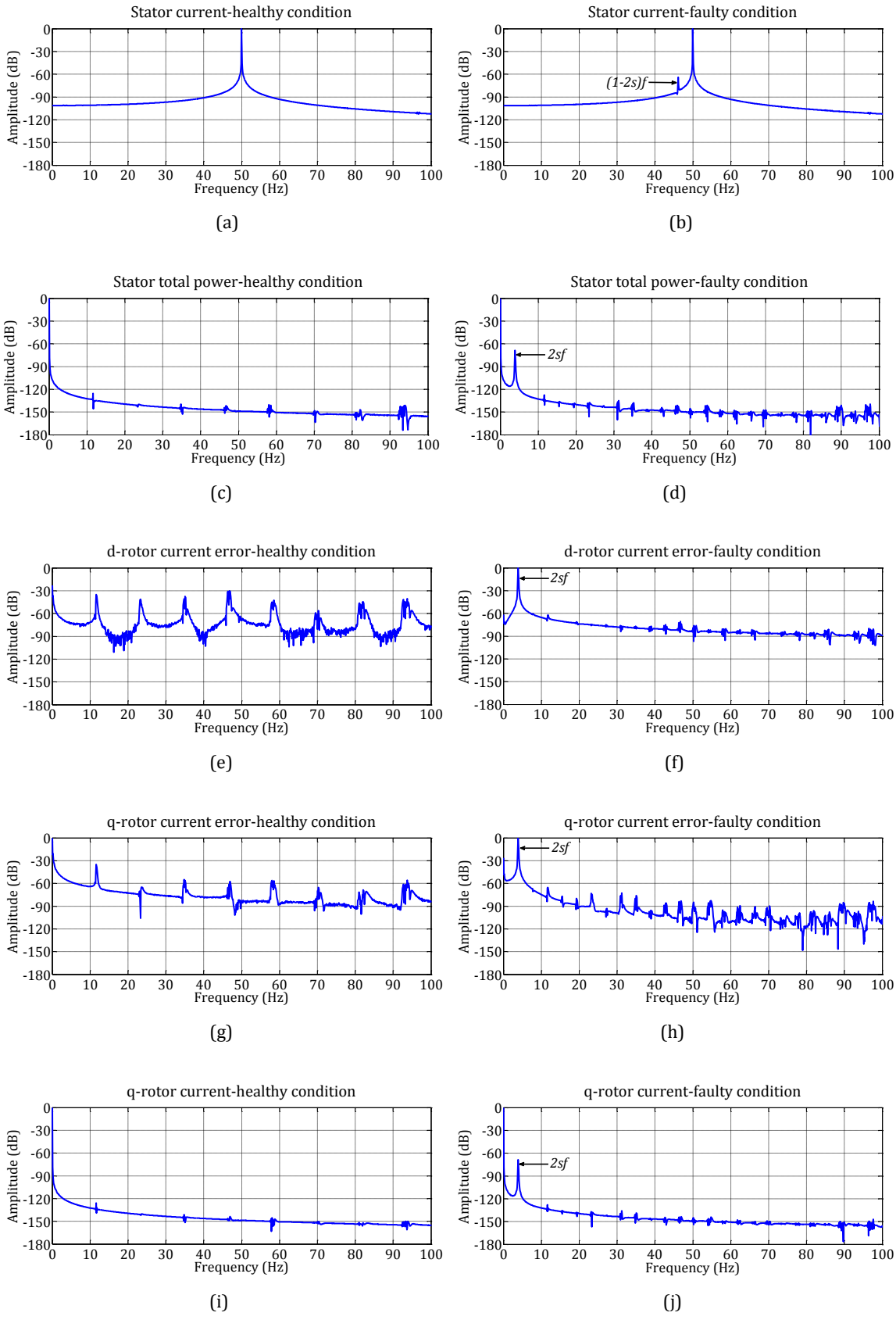

Fig. 6.6: DFIG & RSI control signal spectra simulated at variable speed

6.3.2 Measured Results

The measured results for rotor fault detection under variable speed operation, as shown in Fig. 6.5, are presented in Fig. 6.7a to 6.7j. As shown in section 6.1.2, these measured spectra are noisy compared to the simulated spectra.

The healthy and faulty stator current and total power spectra are presented in Fig. 6.7a to 6.7d. As we can see that the relevant harmonic to the fault is not clear in the current spectrum while it appears at 3.7Hz with a visible normalized value of -60.8dB in the total power spectrum.

Fig. 6.7e to 6.7h compare the measured healthy and faulty spectra for the d- and q-rotor current error signals inside the RSI controller. These spectra show a strong fault indication with a rising harmonic at 3.7Hz with significant magnitudes of -25.0dB and 18.8dB in d- and q-error control signals. As expected from earlier measurements at fixed speed operation, the fault-frequency does not dominate these spectra as they do in the simulated results due to the presence of 100Hz harmonic, due to stator unbalance. The q-rotor current signal is also used in this experimental investigation and the spectrum related the healthy and faulty conditions are shown in Fig. 6.7i and 6.7j. The faulty component ($2sf$) is visible in Fig. 6.7j at frequency 3.7Hz with value -61.6dB. Notice that, this result is similar to the result obtained from using the total power and confirms the previous result in the simulations that the both power and q-rotor current spectra lead to the same normalized magnitude for the faulty component.

It is worth noting that the $2sf$ component magnitudes in the d- and q-rotor current error signals are greater than the same components in the q-rotor current and total power. This is also true for the $(1-2s)f$ component in the stator current. Therefore, the control signal spectral analysis, particularly of the error signals, can be used without confusion as a rotor fault diagnostic index under variable speed operation.

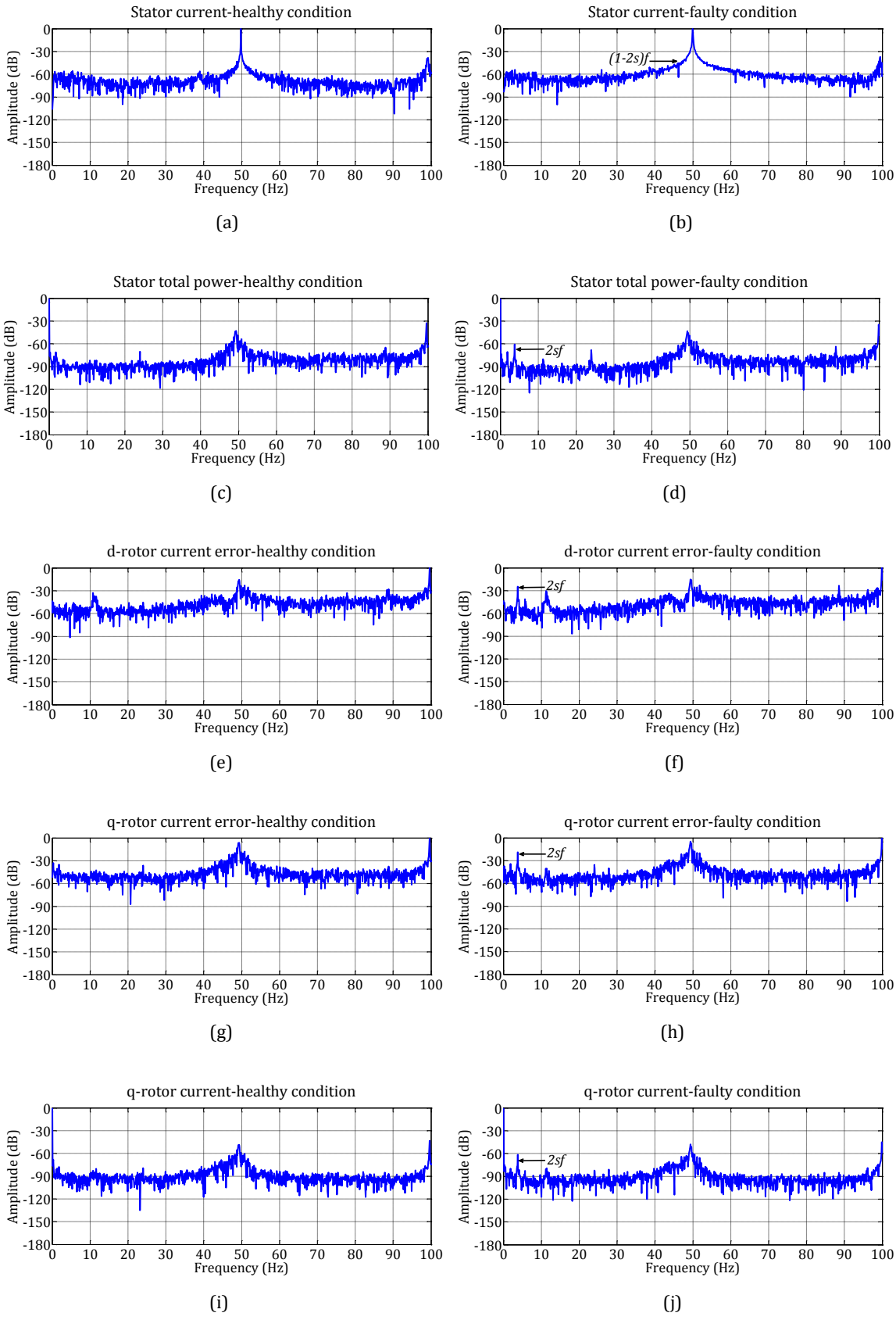

Fig. 6.7: DFIG & RSI control signal spectra measured at variable speed

6.4 Operating Close to Synchronous Speed

As shown in the previous section monitoring of control signals using FFT analysis has successfully detected DFIG rotor electrical asymmetry under both fixed and variable WT speed operation. These results are based on data collected both above and below DFIG synchronous speed. However, real WT DFIGs can operate at synchronous speed or close to it. As stated in Chapter 5, it can be difficult to detect rotor electrical asymmetry when the DFIG operates here due to the dominance of 50.0Hz and 0.0Hz harmonics, respectively in the current or power signal. In theory, this difficulty could be eliminated by using the proposed RSI error signals, where the fault-frequency dominates the spectra. In order to investigate that, several tests were carried out using the Durham Test Rig and its MATLAB model with driving the DFIG almost synchronous speed as shown in Fig. 6.8. Both of rotor balance and 20% rotor unbalance circuits were considered during these investigations.

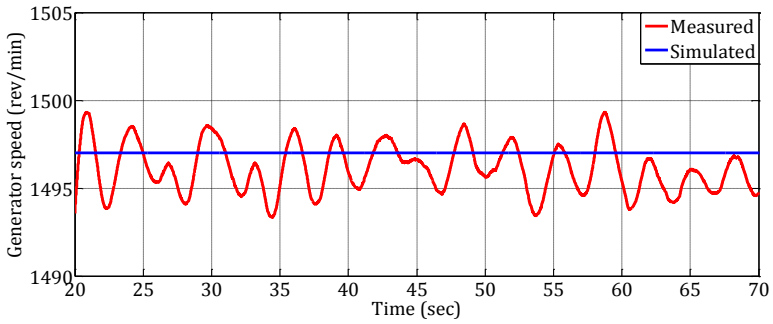

Fig. 6.8: Generator rotational speed signal during simulated & measured tests at almost synchronous speed

6.4.1 Simulation Results

The healthy and faulty spectra of stator current, based on analysing free-noise data, are presented in Fig. 6.9a and 6.9b. It can be seen that, the component $(1-2s)f$ in the presence of the fault is difficult to observe at 49.8Hz with negligible magnitude. Meanwhile, the total power, rotor current errors and q-rotor current spectra, as shown in Fig. 6.9c to 6.9j, lead to indentify the $2sf$ fault-frequency at 0.2Hz. This has the same magnitude of –71.5dB in the power and q-rotor current spectra, while they still have higher magnitudes with 0dB in the d- and q-current error spectra. Due to the location of the fault-frequency being closer to the fundamental 0.0Hz harmonic, detection is clearer using the error signals since the fault harmonic dominates the spectrum, compared to the total power or q-rotor current signals where the fundamental harmonic dominates.

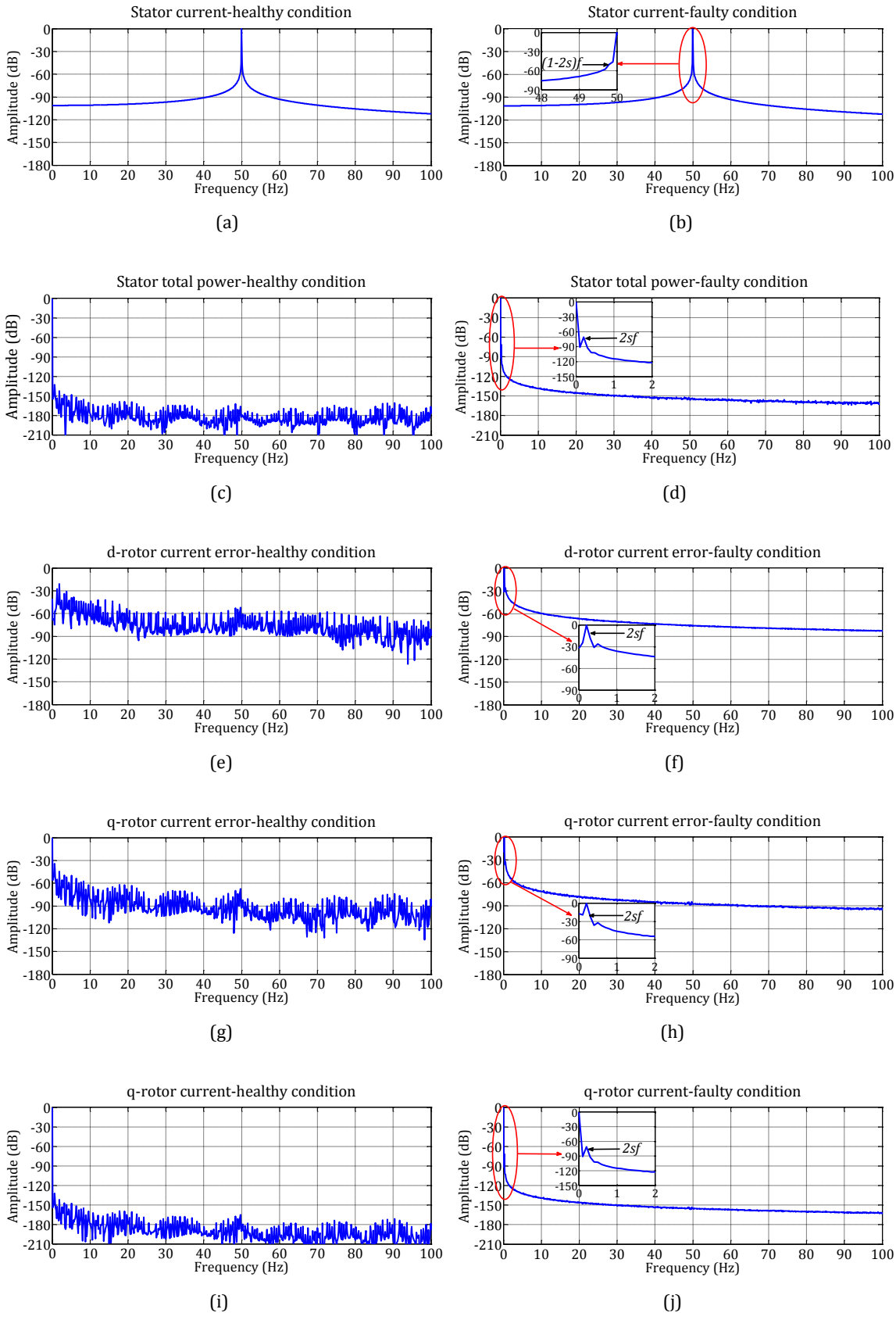

Fig. 6.9: DFIG & RSI control signal spectra simulated at almost synchronous speed

These simulation results show that the harmonic spectra of the control signals as well as the total power have successful detection of incipient rotor electrical asymmetry when the DFIG operates at almost synchronous speed with a significant advantage to the rotor current error signals.

6.4.2 Measured Results

All the spectra presented in this section are obtained from measured data under healthy and faulty operating conditions collected for a period of 42-45s at generator speed shown in Fig. 6.8, again these spectra are noisy, as shown in previous measured results.

Fig. 6.10a and 6.10b show the measured stator current spectra. By comparing the healthy and faulty spectra, the fault harmonic $(1-2s)f$ is difficult to observe or identify. This confirms the simulated result that FFT analysis of stator current has drawbacks in rotor fault detection when the generator operates close to the synchronous speed.

Fig. 6.10c and 6.10d show the spectra obtained from total power, where it can be noted, in Fig. 6.10d, that even though there is a general increase in spectral magnitude around 0.25Hz the $2sf$ fault-frequency cannot be distinguished. This is because the measured data noise, contributed to by the small variation of the measured generator speed, causes an increased fault harmonic bandwidth, which unites with the fundamental.

For the control signals the healthy and faulty spectra are presented in Fig. 6.10e to 6.10j for the control current signals. In particular, in Fig. 6.10f and 6.10h, the $2sf$ component of the d- and q-rotor current errors is still visible at 0.25Hz with normalized magnitudes of -22.8dB and -21.2dB, respectively. However, this harmonic is not clear in the q-rotor current spectrum, in Fig. 6.10j, due to noise.

The measured results obtained show that only the analysis of the spectrum of d- and q-rotor current error signals has the ability of rotor electrical asymmetry detection in case of operating closed to the synchronous speed. Therefore, the control error signals can be used as a good diagnostic index for rotor faults without any confusion at operating speed.

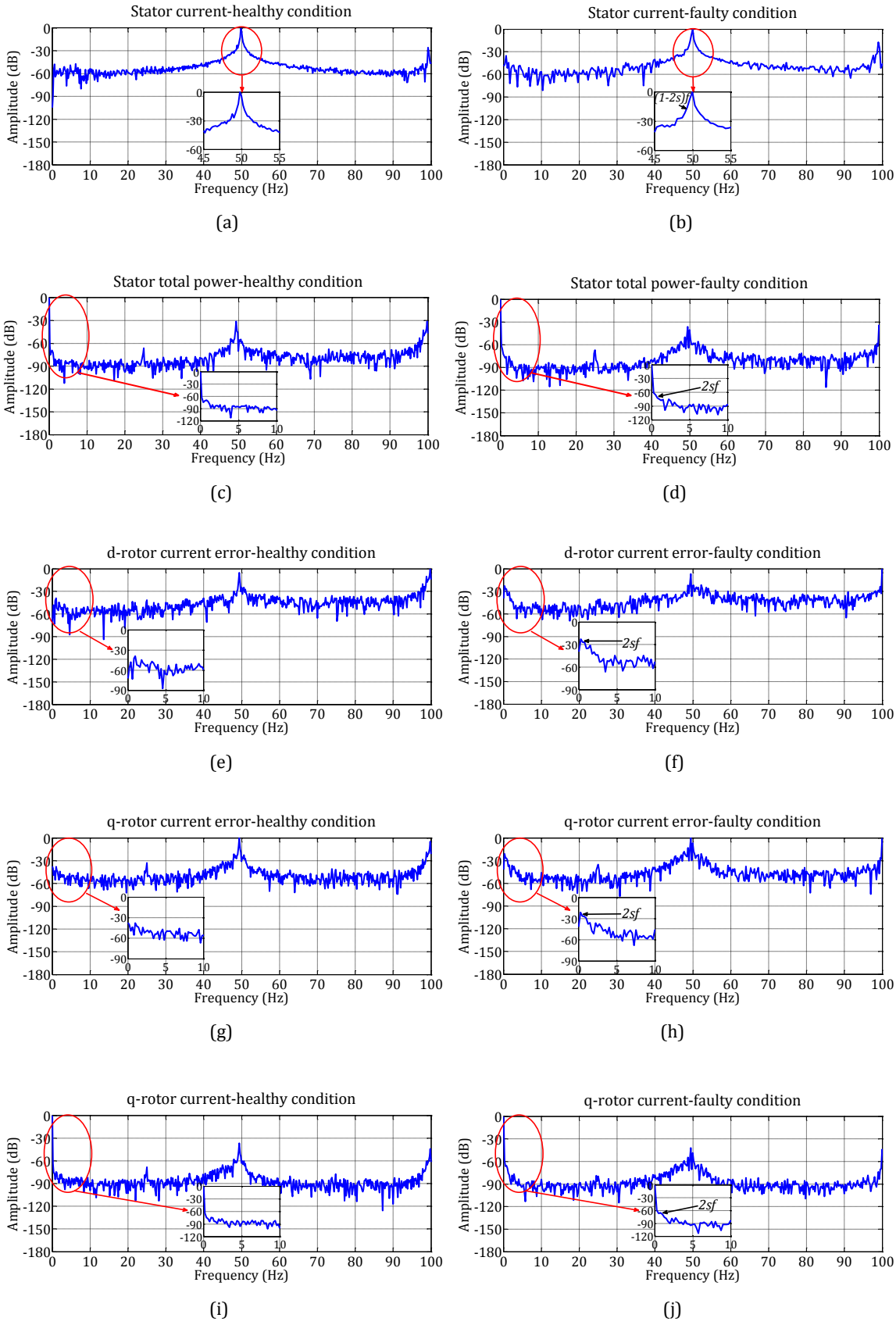

Fig. 6.10: DFIG & RSI control signal spectra measured at almost synchronous speed

6.5 Sensitivity

From the simulated and measured results under fixed and variable speed operations, it can be observed that spectral analysis of all RSI control signals, namely, *d*- and *q*-rotor current error, show an increase in the fault-frequency normalized power level much greater than in the stator current, power and *q*-rotor current. Another advantage of *d*- and *q*-rotor current error signals over the stator current, power and *q*-rotor current is that their spectra demonstrate successful fault detection even when the DFIG operates close to its synchronous speed.

However, the focus on all the previous results is the magnitude of the fault-frequency while the signal that provides the best fault detection not only depends on the fault-frequency magnitude but also on the sensitivity. The higher the sensitivity, the better the fault signature resolution. To verify the sensitivity achievable from the control and other signals for use as diagnostic index, different DFIG operating conditions have been considered. In this work, the detection sensitivity of five signal types has been examined under these different conditions:

- Fault-severity levels;
- Generator speeds;
- PI current control parameters.

In order to investigate the above operating condition cases, further simulated and measured tests were carried out with the DFIG Test Rig for each case. The sensitivity values are obtained from the simulated and measured results in dB by the following:

$$Sensitivity(dB) = 10\log_{10}\left(\frac{A_f - A_h}{A_h}\right) \quad 6.1$$

where A_f and A_h are the magnitudes of the fault and health-harmonic components.

6.5.1 Various Fault-Severities

In this case, various values of the resistance were successively added to one phase of the rotor winding circuit to apply different levels of rotor unbalanced fault. Many tests were simulated on the model Test Rig and measured on the real Test Rig. Those simulated and measured results presented here were collected under steady state operating conditions with the generator delivering 3.35kW and absorbing 1.95kVAr, corresponding to a speed of 1400rev/min (s=0.067).

Complete simulated and measured results of the sensitivity for the five signal types are shown in Fig. 6.11. It can be seen that the sensitivity of all signals increased, in both simulation and measurement, with fault severity. From Fig. 6.11a, the sensitivities of the three simulated control signals have high values and the ability to detect even a small fault severity. The normalized fault-frequency magnitudes are greater in the control error signals. The simulated results show that the *q*-rotor current signal sensitivity is higher than the *d*- and *q*-rotor current error signal sensitivity as well as those of the stator current and power.

The measured results, Fig. 6.11b, shows a decreased sensitivity compared with simulated results, due to the noise in the measured signals, however, the results still show a significant and usable sensitivity for CM purposes. An enlarged version of the measured sensitivity is presented in Appendix D. Again, they show that the control signals have a better sensitivity to rotor faults than the current and power signals, with comparative advantage to the *q*-rotor error current over the other two control signals, stator current and power. That because *q*-rotor error current is less influenced by noise than d-rotor current error and *q*-rotor current, due to the control strategy used.

From these results, it is evident that the three control signals, *q*-rotor current, *d*- and *q*-rotor current errors, are sensitive to any rotor electrical asymmetry condition, with an advantage to the *q*-rotor current and *q*-rotor current error signals over the stator power and current for a whole range of used rotor unbalance.

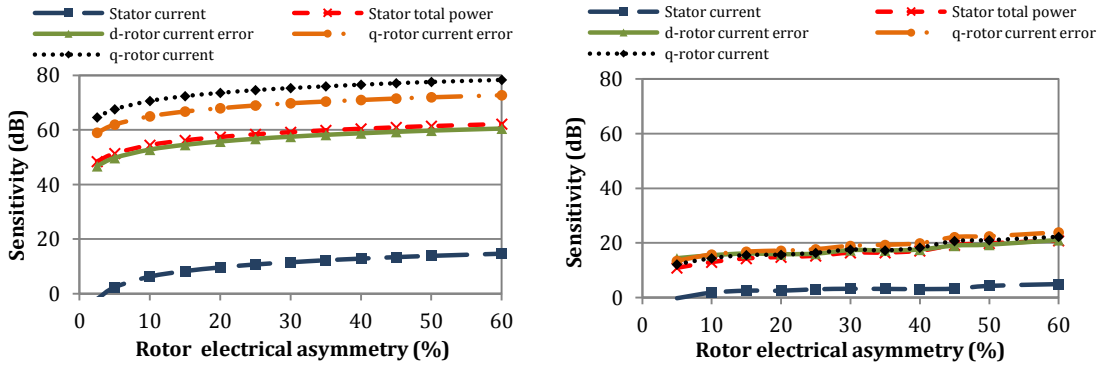

Fig. 6.11: Sensitivity for different severities of fault at fixed speed ≃1400rev/min: (a) simulated (b) measured

6.5.2 Different Generator Speeds

In order to prove the effectiveness of the proposed control signals under different operating speeds, several tests have been performed. During these tests the DFIG operated at different fixed speeds with rotor electrical asymmetry of 20%. Due to the rating current limitation of the batteries the generator has been driven to operate only between 1050rev/min to 1600rev/min (-30% below to +6.7% up synchronous speed). Fig. 6.12a shows the simulated sensitivities of these signals, due to a rotor fault existence, under changing the operating speed of the Test Rig. From these results it can be seen that the control signals has high sensitivity to the fault existence, even at low speed, with a clear advantage to *d*-rotor error current at or close to synchronous speed. Also, the control signal sensitivities are higher than the DFIG stator current and power signals. Furthermore, the control and power signal sensitivities generally increase as the speed moves towards the synchronous speed whiles the stator current decrease. This is as a result of the PI control performance where the whole nonlinear system was linearized at synchronous speed as operating point for control design. Therefore the PI control action becomes more stronger when the system speed move closer to the synchronous speed.

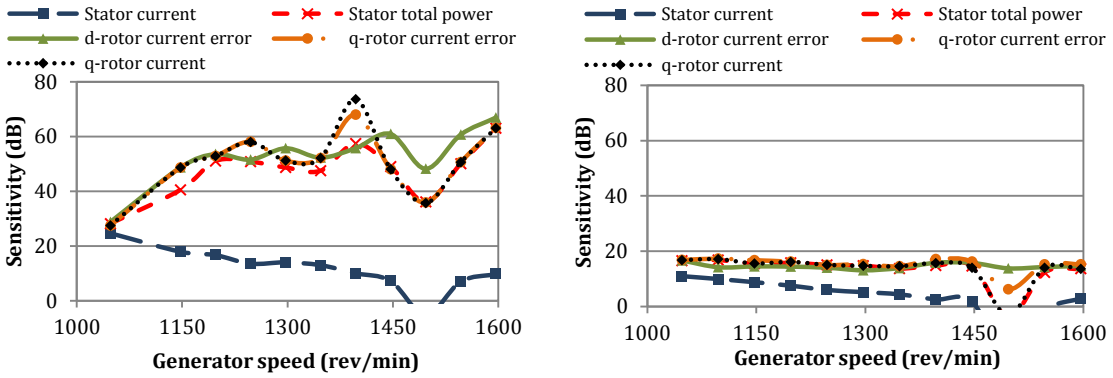

Fig. 6.12: Sensitivity for 20% rotor unbalance at different generator speeds: (a) simulated (b) measured

The measured results, Fig. 6.12b, show that control signals have a good fault detection sensitivity, even at low speeds. Due to the convergence curves in this figure, an enlarged figure of these results can be seen in Appendix D. The results also show a decreased sensitivity compared with simulation, due to the measured signal noise. Moreover, the measured sensitivities of the control and power signal are similar being less affected by speed changes, with a comparative advantage to *q*-rotor current error when the DFIG operates away from the synchronous speed. At synchronous speed, *q*-

rotor current and power sensitivities drop dramatically while the d- and q-rotor current error sensitivities still have significant values, with advantage to the d-rotor current error. However, stator current sensitivity is slightly decreased as speed increases and is completely lost close to synchronous speed.

The results show clearly that, with respect to stator current and power, the control signals have a higher sensitivity for the characteristic rotor fault-frequency, regardless of the generator speed.

6.5.3 Different PI Current Control Parameters

It is known that PI control performance depends upon controller bandwidth, where greater bandwidth means faster response. This bandwidth is usually set by the manufacturer and is, therefore, usually fixed using by well-publicised control parameters.

In this work, the RSI controller had only PI control in the rotor current closed loops and the control performance was strongly affected by these current regulator's bandwidth. Therefore, it was expected that the rotor current closed loop controller bandwidth could affect the proposed fault detection techniques, where the magnitudes of fault-frequencies appearing in the spectrum would depend, not only on machine condition, but also on the control closed loop bandwidth. In this section, therefore, the diagnostic sensitivity of this procedure for rotor asymmetries is investigated with respect to bandwidth variations.

The bandwidth of the rotor current closed loop, in this system, is directly proportional to PI control parameters (K_p & K_i), where higher values of K_p and K_i give higher bandwidth. Therefore the bandwidth effect can be investigated using different values of K_p and K_i. So, simulations were performed with different values of the current PI control parameters, with the generator operating at 1400 rev/min, delivering 3.35kW and absorbing 1.95kVAr from the stator side. In Fig. 6.13a, the simulation results for a 20% rotor electrical asymmetry are reported. It can be seen that the three control signals have higher sensitivity values than the stator current and power signals even at high control parameter values. However, the stator current, stator total power, q-rotor current and q-rotor current error sensitivities are strongly affected by control system action, having lower sensitivity with increased control parameter values. On the contrary, the sensitivity of the $2sf$ component in the d-rotor current error signal is quite independent of control parameters.

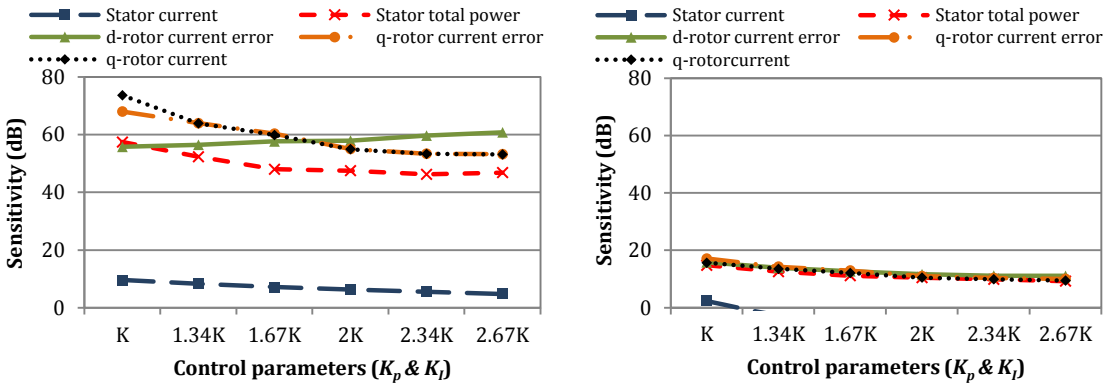

(a) (b)

Fig. 6.13: Sensitivity for different values of the control proportional & integral gains at fixed speed ≃1400rev/min: (a) simulated (b) measured

The impact of closed loop current bandwidth was also realized experimentally by keeping the same operating conditions and changing the values of the PI current control parameters. In practice, a control parameter value increase lead to increased closed loop bandwidth and increased noise in the measured signals, resulting in reduced fault-frequency visibility in the spectrum and therefore reduced signal sensitivity. This can be seen in the measured results presented in Fig. 6.13b where all measured sensitivities decreased compared with simulated results. An enlarged version is presented in Appendix D. Notice that the measured *d*-rotor current error sensitivity is dependent on the control parameter values due to noise, which is not the case in the noise-free simulated signal. These results also show that, as proportional and integral gain values increase the stator current $(1-2s)f$ component is ineffective as a rotor fault diagnostic index because the current component loses its sensitivity. On the other hand, it is evident that, for any control parameter values, the control signals are more sensitive to rotor faults than the stator current or power, with advantage to the control error signals.

The simulated and measured results show that the spectrum of the control signals are affected by the control parameters, however, this should not be considered a drawback of the proposed method for WT applications for the following reasons. In a WT, the generator control parameters are carefully chosen, well-protected and fixed values. They cannot be changed suddenly because any deviation from the chosen values could lead to inaccurate performance of the controller and the whole turbine. Therefore, only fault severity and operating speed conditions will influence on the sensitivity of the proposed technique based.

6.5.4 Comparison of Fault Detection Sensitivities between Open & Closed Loop Test Rig Systems

As mentioned in Chapter 3, the open loop Test Rig was used in previous work to develop successful different CM techniques for fault detection of WT driven WRIGs. One of these techniques is the frequency tracking algorithm based in the stator line current and total power analysis [37]. This method was investigated with different WT fault detection including rotor electrical asymmetry, shaft mass unbalance and gear tooth failure. In this section, an experimental comparison between the rotor fault detection sensitivity of closed loop Test Rig inside RSI control signals and the open loop fault detection sensitivity using the frequency tracking is made. More recently, another technique was introduced in [105] based on the sideband power factor (SBPF) algorithm of the vibration analysis for WT fault detection. The SBPF was successful in detection of early stages of gearbox tooth wearing and missing tooth for high speed shaft pinion. The SBPF algorithm sums the power spectrum amplitudes of the HS stage meshing frequency second harmonic and its first 5 sideband peaks on each side. Current work is being carried out by PhD student D. Zappala to extend the vibration analysis for rotor electrical asymmetry detection in WRIG and however the result is not available at the time of writing. Therefore, only the vibration analysis results for gearbox fault detection was presented in the comparison. Table 6.2 shows a comparison between the three different techniques being used with open & closed loop Test Rig for fault detections as well as the measured sensitivities from each technique achieved at two different generator speeds. Notice that it is not valid to compare the presented vibration result directly with the other results because it was obtained for different type of fault.

Table 6.2: Comparison of fault detection sensitivities between open & closed loop Test Rig

Test Rig system	**Closed loop system**		**Open loop system**				**Open loop system**
Signal type	Current error signals inside RSI		Stator current		Stator total power		Vibration
	$\varepsilon_{i_{dr}}$	$\varepsilon_{i_{qr}}$					
Frequency analysis	FFT		Frequency tracking algorithm				SBPF
Fault type	20% Rotor electrical asymmetry		23% Rotor electrical asymmetry				Missing tooth of high speed shaft pinion
Harmonics of interests	$2sf$		$(1-2s)f$	$(3-2s)f$	$2sf$	$(2-2s)f$	$2f_{mesh,HS}$ & its first 5 sideband peaks on each side.
Sensitivity calculated at 1550rev/min	14.3dB	15.2dB	3.0dB	4.7dB	6.7dB	4.9dB	5.1dB
Sensitivity calculated at 1600rev/min	14.6dB	15.3dB	3.7dB	6.9dB	7.3dB	6.0dB	4.6dB

As we can see from Table 2.1, the RSI control current error sensitivity to the fault existence is much higher than the frequency tracking algorithm with the same fault magnitude. This comparison confirms that the closed loop detection sensitivities, even with noise on the Test Rig, are considerably greater than they were achieved open loop with current, and power signals. A direct comparison with the SPBF results for electrical fault detection would be possible once results are available.

6.6 Conclusions

This chapter has presented the results from the application of the new monitoring and diagnosis algorithm, based on the FFT analysis of the RSI control signals, for WT DFIG rotor fault. The data has been collected from a physical Test Rig, representing a WT DFIG concept, and its validated MATLAB model, under different fixed and variable speed operation conditions. An RSI stator flux-oriented vector control scheme has been adopted in both systems. Rotor electrical asymmetry of 20% has been applied to the generator and the relevant fault frequency of interest ($2sf$), introduced through Chapter 5, was successfully detected in selected signals by the proposed algorithm. The simulated and measured results have proved the benefits of this method, particularly using the *d*- and *q*-rotor current error signals compared to the stator current and power signals. These benefits are:

- Lower fault-frequency compared with stator current signal;
- *d*- and *q*-rotor current error signals have characteristic frequencies that act as strong indicators of rotor electrical asymmetry under fixed or variable speed conditions, and the fault-frequency dominates its spectrum if the generator has no other faults;
- *d*- and *q*-rotor current error spectra leads to easy fault detection when the system operates at or close to the synchronous speed;
- In practice, these signals are available for control purpose and can easily be accessed, thereby reducing the number of sensors required, compared with the stator power;
- Both *d*- and *q*-rotor current error spectra give complete information about the DFIG three phases condition, compared with just one specific phase monitored in the case of stator current.

The sensitivity of the proposed method has been investigated with respect to the following operating conditions

- Different generator speeds;
- Different fault levels;
- Different control parameters.

Although the RSI control signals are affected by these operating conditions, as well as DFIG stator current and power, the simulated and measured results have confirmed the success of fault detection using control signals and their sensitivity is generally higher than that of stator current or total power signals. Also, the results showed that the fault detection sensitivity for the closed loop WT-IG inside the RSI control signals is better than the sensitivity for open loop WT-IG achieved by vibration, current and power signals.

7 Conclusions & Further Work

7.1 Conclusions

This thesis has presented an investigation into CM for a modern variable speed WT using the DFIG concept and proposes a new generator fault detection technique based on the frequency analysis of the DFIG closed loop controller signals. The signals, namely; *q*-rotor current, *d*- and *q*-rotor current errors, were used for diagnostic purpose are generated inside the control system of the RSI. This technique depends upon monitoring the increase in power level of a fault-frequency component in the control signal spectrum, obtained by FFT analysis. The use of generator control loop signals for CM, was proposed due to its advantages over conventional techniques, such as vibration monitoring, namely that it can reduce the number of sensors required and will be cheaper. Furthermore, these signals are already readily available for control purposes and can be easily accessed.

7.1.1 Investigation Tools

In order to investigate the proposed method, an existing MATLAB and physical Durham Test Rig were developed further from an open loop generator (WRIG configuration) into closed loop generator (DFIG configuration) with appropriate converter. The main developments to the simulation and physical systems, as a part of this research, by the author were:

7.1.1.1 MATLAB Simulink Test Rig Model

- Improving the drive train model by representing the friction, windage loss coefficients of the DC motor, gearbox and DFIG;
- Improving the performance of the control loop of DC motor, by adding the inner current control loop and represent the DC motor field windings circuit;
- Modelling the DFIG electrical system;
- Modelling the grid voltage and impedance;
- Modelling the generator closed loop. This includes modelling the RSI itself, the DC voltage link and designing and modelling RSI controller based on SFOVC scheme.

7.1.1.2 Physical Test Rig

After modelling the generator closed loop successfully in the MATLAB Model, the work was extended experimentally to close the generator control loop in the physical Test Rig. This work included:

- Installation of back-to-back converter between the grid and the rotor side of the generator;
- Installation of an xPC TargetBox as an interface between the PC controller and the generator;
- Installation of new voltage and current cards;
- Installation of incremental encoder on the generator rotor;
- Building and implementing the RSI controller.

Both closed loop systems were evaluated in the time domain by comparing simulated and measured signals obtained from various tests with different operating speeds. This comparison includes electrical and mechanical signals such as rotor and stator currents, active and reactive stator powers, control currents and generator speed. The results clearly showed that there was good agreement between measured and simulated signals.

7.1.2 Fault Detection Algorithm

In this research the method, based upon spectral analysis of d- and q-current errors, generated by current regulators, as well as of q-rotor current, of the inverter connected to the three-phase DFIG rotor side, is presented. The ability of this technique on fault diagnosis has been investigated in the presence of DFIG rotor electrical asymmetry. An in-depth investigation of the influence of rotor electrical asymmetry on the proposed control signals has been described and the characteristic fault-frequency is explained. The fast Fourier transform (FFT) has been used for analysing the identified signal and presented as a spectrum. Once a spectrum has been extracted, the fault can easily be determined at frequency 2sf. To simplify the presentation of the results and perform easier comparison, all signal spectral analyses has been normalized to the highest harmonic component in the spectrum, which depends on the signal type and machine condition. During this work, the proposed technique has been primarily examined under various fixed and variable speed operating conditions and the results have been compared with the stator current and total power signal results, as these have been commonly used in the past. The sensitivity of the proposed control signals for fault analysis, as well as the previously used

stator current and total power signals, have been studied under different operating conditions in the Matlab model and physical Test Rig using the following conditions:

- Different Generator Speed with fixed fault level and fixed control parameters;
- Different fault level with fixed generator speed and fixed control parameters;
- Different control parameters with fixed generator speed and fixed fault level.

The research effort has provided evidence of the superiority, for the detection of WT DFIG rotor electrical asymmetry, of RSI control signals over DFIG electrical signals, stator current and total power, namely because:

- Fault-frequencies dominate the control error signal spectra, *d*- and *q*-rotor current errors, and therefore their spectra have characteristic frequencies that are stronger indicators of rotor electrical asymmetry than other signals under fixed or variable speed operations;
- The control error signals have easier fault detection ability, when the DFIG operates close to synchronous speed, than the stator current, total power or control *q*-rotor current;
- It also clearly shown that the control signal provides better sensitivity to rotor faults than the stator current or total power signals and is a successful diagnostic even with small faults;
- Even though control signals are influenced by the operating speed and the control gains, they still provide higher sensitivity for a fault than the stator current or total power signals;
- Fault detection sensitivity for the closed loop WT-IG by the RSI control signals is better than the sensitivity of current and power signals for open loop WT-IG;
- Monitoring line or phase stator current only gives information about the specific phase or line being measured, while monitoring total power increases the number of transducers and consequent noise. However, monitoring the control signals offers an equal contribution from all phases, minimizes noise and costly extra transducers and data processing;
- This technique is simple, attractive and could easily be extended to diagnose other generator or embedded turbine faults.

7.2 Future Work

7.2.1 Test Rig

- During this research, a significant development has been carried out on the Durham Test Rig from WRIG (open loop) to DFIG (closed loop) configuration by connecting a converter to the generator rotor. However, due to the limitations of the current xPC TargetBox hardware in synchronizing the generated phase PWM signals both the DC voltage link and the stator voltage was purposely reduced, compared to the generator and converter rating, to provide lower overlap distortion in the control and generator variables and increase safety. This was been achieved with disconnecting the GSI and connecting the RSI through 48volt batteries to represent the DC link. Consequently, to improve the Test Rig it should use a full power back-to-back converter with a version of xPC TargetBox hardware developed to overcome the drawbacks of the current hardware.
- Due to noise on the experimental system the measured results give a lower sensitivity to faults than the simulated results. Work will be require in the future to reduce the noise in measured signals by improving the operational condition, that is balanced stator voltage, fixed stator frequency and balanced stator winding of the Test Rig, to improve signal quality and lead to improved sensitivity.

7.2.2 Faults

The proposed techniques could be used to investigate new fault detection areas of the WT such as:

- Other generator electrical faults such rotor and stator winding short-circuit;
- Mechanical faults such as high speed shaft mechanical unbalance and generator bearing faults. These failures are important and lead to significant downtime when the shaft and generator need to be replaced;
- Power electronic faults such as RSI transistor base open fault and transistor short-circuit fault. Although converter and electronic failure downtimes are normally short onshore they are likely to be significantly changed as WTs go offshore. In the offshore environment, these failures cannot be repaired quickly, due to lack of access, and will have a knock-on effect on converter controlled WT downtime.

References

[1] ExxonMobil, "The Outlook for Energy - A View to 2030," 2008.

[2] D. J. C. MacKay, Sustainable energy: without the hot air. Cambridge, England: UIT Cambridge Ltd., 2009.

[3] E. W. E. Association, "Wind in power-2011 European statistics," February 2012.

[4] E. W. E. Association, "Green Growth: The impact of wind energy on jobs and the economy," April 2012.

[5] E. W. E. Association, "Pure Power: Wind energy targets for 2020 and 2030," 2011.

[6] E. Commission, "EU energy trends to 2030 — Update 2009," 2010.

[7] E. W. E. Association, "Wind in our salis- the coming of Europe's offshore wind energy industry," 2011.

[8] N. Haluzan. (2011, February 16). Offshore wind power – Advantages and disadvantages [Online]. Available: http://www.renewables-info.com/drawbacks_and_benefits/offshore_wind_power_%E2%80%93_advantages_and_disadvantages.html

[9] E. W. E. Association, "the European offshore wind industry-key trends and statistics 1st half 2012," 2012.

[10] A. Truewind, "Offshore Wind Technology Overview," September 2009.

[11] O. E. Council. (2013), Offshore Wind Energy [Online]. Available: http://www.oceanenergycouncil.com/index.php/Offshore-Wind/Offshore-Wind-Energy.html

[12] D. McMillan and G. W. Ault, "Quantification of condition monitoring benefit for offshore wind turbines," Wind Engineering, vol. 31, pp. 267-285, 2007.

[13] J. Nilsson and L. Bertling, "Maintenance management of wind power systems using condition monitoring systems-Life cycle cost analysis for two case studies," IEEE Transactions on Energy Conversion, vol. 22, pp. 223-229, 2007.

[14] S. J. Watson, B. J. Xiang, W. Yang, P. J. Tavner and C. J. Crabtree, "Condition monitoring of the power output of wind turbine generators using wavelets," IEEE Transactions on Energy Conversion, vol. 25, pp. 715-721, 2010.

[15] T. Capital. Transmission for UK Offshore Wind [Online]. Available: http://www.transmissioncapital.co.uk/projects/uk-offshore-wind-transmission

[16] RenewableUK. (2012), 10 facts about UK offshore wind [Online]. Available: http://www.bwea.com/offshore/index.html

[17] A. Misherghi, "Renewable Energy in Libya: Potentials, Current Situation and Way forward," presented at the Africa Energy Forum, Berlin, Germany, 2012.

[18] I. M. Saleh, "Prospects of renewable energy in Libya," in The international symposium on solar physics and solar eclipses (SPSE 2006), Waw an Namos, Libya, 2006, pp. 153-161.

[19] "Country Report Libya," December 2009, revised April 2010.

[20] R. Abdiwe, "Renewable Energy in Libya, Present Situation and Future Plans," presented at the Solar Energy in the MENA Region, Erfurt, Germany, 2009.

[21] J. Santamarta. (2011, January 26). Libya to build first wind energy plant [Online]. Available: http://www.evwind.es/2011/01/26/libya-to-build-first-wind-energy-plant/9786/

[22] E. W. E. Association, "Powering Europe: wind energy and the electricity grid," November 2010.

[23] J. C. Sabonnadière, Renewable Energy Technologies: Wiley-ISTE, 2009.

[24] R. R. Hill, J. A. Stinebaugh, D. Briand, A. S. Benjamin and J. Linsday, "Wind Turbine Reliability: A Database and Analysis Approach," Sandia National Laboratories, Albuquerque, New Mexico 87185 and Livermore, California 94550, Sandia Report SAND2008-0983, 2008.

[25] C. A. Walford, "Wind turbine reliability: understanding and minimizing wind turbine operation and maintenance costs," Sandia National Laboratorie, Albuquerque, New Mexico 87185 and Livermore, California 94550, Sandia Report SAND2006-1100, 2006.

[26] C. o. C. Change, "Costs of low-carbon generation technologies," May 2001.

[27] S. Bassi, A. Bowen and S. Fankhauser, "The case for and against onshore wind energy in the UK," June 2012.

[28] S. Faulstich, B. Hahn, P. Lyding and P. Tavner, "Reliability of offshore turbines-identifying risks by onshore experience," in European Offshore Wind, Stockholm, Sweden, 2009.

[29] P. Tavner, offshore wind turbines reliability, availability and maintenance: The institution of Engineering and Technology, 2012.

[30] P. Tavnet, G. Van Bussel and F. Spinato, "Machine and converter reliabilities in wind turbines," in The 3rd IET International Conference on Power Electronics, Machines and Drives, Dublin, 2006, pp. 127-130.

[31] P. Tavner, J. Xiang and F. Spinato, "Reliability analysis for wind turbines," Wind Energy, vol. 10, pp. 1-18, 2007.

[32] F. Spinato, P. Tavner, G. Van Bussel and E. Koutoulakos, "Reliability of wind turbine subassemblies," IET Renewable Power Generation, vol. 3, pp. 387-401, 2009.

[33] P. Tavner, S. Faulstich, B. Hahn and G. J. W. van Bussel, "Reliability & Availability of Wind Turbine Electrical & Electronic Components," European Power Electronics (EPE), vol. 20, 2010.

[34] S. Faulstich, B. Hahn and P. Tavner, "Wind turbine downtime and its importance for offshore deployment," Wind Energy, vol. 14, pp. 327-337, 2011.

[35] P. J. Tavner, "Review of condition monitoring of rotating electrical machines," IET Electric Power Applications, vol. 2, pp. 215-247, 2008.

[36] K. Alewine and W. Chen, "Wind Turbine Generator Failure Modes Analysis and Occurrence," presented at the Wind power 2010, Dallas, Texas, 2010.

[37] C. J. Crabtree, "Condition Monitoring Techniques for Wind Turbines," PhD Thesis, School of Engineering and Computing Sciences, University of Durham, Durham, United Kingdom, 2011.

[38] D. I. B. Hahn, "Zeitlicher Zusammenhang von Schadenshäufigkeit und Windgeschwindigkeit," in 22. FGW-Workshop "Einfluß der Witterung auf Windenergieanlagen",06, Institut für Meteorologie, Leipzig, 1997.

[39] P. Tavner, C. Edwards, A. Brinkman and F. Spinato, "Influence of wind speed on wind turbine reliability," Wind Engineering, vol. 30, pp. 55-72, 2006.

[40] B. Lu, Y. Li, X. Wu and Z. Yang, "A review of recent advances in wind turbine condition monitoring and fault diagnosis," in IEEE Power Electronics and Machines in Wind Applications (PEMWA), Lincoln, 2009, pp. 1-7.

[41] M. Entezami, "Wind Turbine Condition Monitoring System," 3 Month PhD Progress Report,School of Electronic, Electronic and Computer Engineering, University of Birmingham, Birmingham, United Kingdom, 2010.

[42] M. J. Schulz and M. J. Sundaresan, "Smart Sensor System for Structural Condition Monitoring of Wind Turbines," National Renewable Energy Laboratory, USA, August 2006.

[43] M. J. Sundaresan, M. J. Schulz and A. Ghoshal, "Structural health monitoring static test of a wind turbine blade," National Renewable Energy Laboratory, USA,2002.

[44] C. C. Ciang, J.-R. Lee and H.-J. Bang, "Structural health monitoring for a wind turbine system: a review of damage detection methods," Measurement Science and Technology, vol. 19, pp. 1–20, 2008.

[45] C. J. Crabtree, "Survey of Commercially Available Condition Monitoring Systems for Wind Turbines," University of Durham, Durham, United Kingdom, Technical Report, 2010.

[46] S. Williamson and A. Smith, "Steady-state analysis of 3-phase cage motors with rotor-bar and end-ring faults," IEE Proceedings B Electric Power Applications, vol. 129, pp. 93-100, 1982.

[47] W. T. Thomson and M. Fenger, "Current signature analysis to detect induction motor faults," IEEE Industry Applications Magazine, vol. 7, pp. 26-34 2001.

[48] A. Bellini, F. Filippetti, G. Franceschini, C. Tassoni and G. B. Kliman, "Quantitative evaluation of induction motor broken bars by means of electrical signature analysis," IEEE Transactions on Industry Applications, vol. 37, pp. 1248-1255, 2001.

[49] M. E. H. Benbouzid, H. Nejjari, R. Beguenane and M. Vieira, "Induction motor asymmetrical faults detection using advanced signal processing techniques," IEEE Transactions on Energy Conversion, vol. 14, pp. 147-152, 1999.

[50] J. R. Cameron, W. T. Thomson and A. B. Dow, "Vibration and current monitoring for detecting airgap eccentricity in large induction motors," IEE Proceedings B Electric Power Applications, vol. 133, pp. 155-163 1986.

[51] S. Nandi, R. M. Bharadwaj and H. A. Toliyat, "Performance analysis of a three-phase induction motor under mixed eccentricity condition," IEEE Transactions on Energy Conversion, vol. 17, pp. 392-399, 2002.

[52] C. Concari, G. Franceschini and C. Tassoni, "A MCSA procedure to diagnose low frequency mechanical unbalances in induction machines," presented at the XIX International Conference on Electrical Machines (ICEM), Rome, Italy, 2010.

[53] S. F. Legowski, A. H. M. Sadrul Ula and A. M. Trzynadlowski, "Instantaneous power as a medium for the signature analysis of induction motors," IEEE Transactions on Industry Applications, vol. 32, pp. 904-909 1996.

[54] J. Penman, J. G. Had Wick and B. Barker, "Detection of faults in electrical machines by examination of the axially directed fluxes," in 3rd International Conference on Electrical machines (ICEM), Brussels, Belgium, 1978.

[55] J. S. Hsu, "Monitoring of defects in induction motors through air-gap torque observation," IEEE Transactions on Industry Applications, vol. 31, pp. 1016-1021, 1995.

[56] A. Bellini, F. Filippetti, G. Franceschini and C. Tassoni, "Closed loop influence on induction machine asymmetries effects," in IEEE International Symposium on Diagnostics for Electrical Machines, Power Electronics and Drives (SDEMPED'99), Gijón, Spain, 1999, pp. 43-50.

[57] A. Bellini, F. Filippetti, G. Franceschini and C. Tassoni, "Closed-loop control impact on the diagnosis of induction motors faults," IEEE Transactions on Industry Applications, vol. 36, pp. 1318-1329, 2000.

[58] E. Serna and J. Pacas, "Detection of rotor faults in field oriented controlled induction machines," in IEEE Industry Applications Conference Forty-First IAS Annual Meeting, Tampa, FL, USA, 2006, pp. 2326-2332.

[59] E. Serna and M. Pacas, "Limitations on Detecting Rotor Asymmetries from the Measured Currents in Closed Loop Operation," in IEEE International Symposium on Industrial Electronics (ISIE), Vigo, Spain, 2007, pp. 1311-1316

[60] S. M. A. Cruz and A. J. M. Cardoso, "Fault indicators for the diagnosis of rotor faults in FOC induction motor drives," in IEEE International Electric Machines & Drives Conference (IEMDC), Antalya, Turkey, 2007, pp. 1136-1141.

[61] C. Concari, G. Franceschini, E. Lorenzani and A. Toscani, "Severity assessment of rotor faults in closed loop induction drives by different approaches," in IEEE International Symposium on Diagnostics for Electric Machines, Power Electronics and Drives (SDEMPED 2007), Cracow, Poland, 2007, pp. 309-315.

[62] C. Concari, G. Franceschini and C. Tassoni, "Rotor fault detection in closed loop induction motors drives by electric signal analysis," in the 18th International Conference on Electrical Machines, Vilamoura, Portugal, 2008.

[63] S. Djurovic, C. Crabtree, P. Tavner and S. Smith, "Condition Monitoring of Wind Turbine Induction Generators with Rotor Electrical Asymmetry," IET Renewable Power Generation, vol. 6, pp. 207–216, 2012.

[64] L. M. Popa, B. B. Jensen, E. Ritchie and I. Boldea, "Condition monitoring of wind generators," in IEEE Industry Applications Conference 38rh IAS Annual Meeting, Salt Lake City, 2003, pp. 1839-1846.

[65] D. Shah, S. Nandi and P. Neti, "Stator-Interturn-Fault Detection of Doubly Fed Induction Generators Using Rotor-Current and Search-Coil-Voltage Signature Analysis," IEEE Transactions on Industry Applications, vol. 45, pp. 1831-1842, 2009.

[66] A. Yazidi, H. Henao, G. Capolino, D. Casadei, F. Filippetti and C. Rossi, "Simulation of a doubly-fed induction machine for wind turbine generator fault analysis," in 5th IEEE International Symposium on Diagnostics for Electric Machines, Power Electronic Diagnostics for Electric Machines, Power Electronics and Drives (SDEMPED 2005), Vienna, 2005, pp. 1-6.

[67] D. Casadei, F. Filippetti, A. Stefani, C. Rossi, A. Yazidi and G. Capolino, "Experimental fault characterization of doubly fed induction machines for wind power generation," in International Symposium on Power Electronics, Electrical Drives, Automation and Motion (SPEEDAM) Taormina, 2006, pp. 1281-1286.

[68] A. Stefani, A. Yazidi, C. Rossi, F. Filippetti, D. Casadei and G. A. Capolino, "Doubly fed induction machines diagnosis based on signature analysis of rotor modulating signals," IEEE Transactions on Industry Applications, vol. 44, pp. 1711-1721, 2008.

[69] D. Casadei, F. Filippetti, C. Rossi and A. Stefani, "Closed loop bandwidth impact on doubly fed induction machine asymmetries detection based on rotor voltage signature analysis," in 43rd International Universities Power Engineering Conference "UPEC 2008", Padova, Italy, 2008, pp. 1-5.

[70] S. Yang, A. Bryant, P. Mawby, D. Xiang, L. Ran and P. Tavner, "An Industry-Based Survey of Reliability in Power Electronic Converters," IEEE Transactions on Industry Applications, vol. 47, pp. 1441-1451, 2011.

[71] D. Kastha and B. K. Bose, "Investigation of Fault Modes of Voltage-Fed Inverter System for Induction Motor Drive," IEEE Transactions on Industry Applications, vol. 30, pp. 1028-1038, July-August 1994.

[72] M. R. Wilkinson, "Condition Monitoring for Offshore Wind Turbines," PhD Thesis, Newcastle University, Newcastle, United Kingdom, 2008.

[73] W. Yang, P. J. Tavner, C. J. Crabtree and M. Wilkinson, "Cost-Effective Condition Monitoring for Wind Turbines," IEEE Transactions on Industrial Electronics, vol. 57, pp. 263-271, 2010.

[74] W. Hsu, "Measurements on a Wind Turbine Condition Monitoring Test Rig," MSc Research Project, School of Engineering and Computing Sciences, University of Durham, Durham, United Kingdom, 2008.

[75] J. Emslie, "Mathematical Modelling of the Drive Train of a Wind Turbine Test Rig," MEng Final Year Project Report, School of Engineering and Computing Sciences, University of Durham, Durham, United Kingdom, 2010.

[76] M. George, K. P. Basu and A. T. W. Chiat, "Model Reference Controlled Separately Excited DC Motor," Neural Computing & Applications, vol. 19, pp. 343-351, 2010.

[77] F. Gonzalez-Longatt, O. Amaya, M. Cooz and L. Duran, "Dynamic Behaviour of Constant Speed WT based on Induction Generator Directly connected to Grid," presented at the World Wind Energy Conference and Exhibition, Mar del plata Argentina, 2007.

[78] H. Li, Z. Chen and J. K. Pederson, "Optimal Power Control Strategy of Maximizing Wind Energy Tracking and Conversion for VSCF Doubly Fed Induction Generator System," in CES/IEEE 5th International Power Electronics and Motion Control Conference, Shanghai, China 2006, pp. 1-6.

[79] T. Senjyu, R. Sakamoto, N. Urasaki, T. Funabashi, H. Fujita and H. Sekine, "Output power leveling of wind turbine Generator for all operating regions by pitch angle control," IEEE Transactions on Energy Conversion, vol. 21, pp. 467-475, 2006.

[80] M. B. Mohamed, M. Jemli, M. Gossa and K. Jemli, "Doubly fed induction generator (DFIG) in wind turbine modeling and power flow control," in IEEE International Conference on Industrial Technology USA, 2004, pp. 580-584.

[81] G. Tapia, G. Santamaria, M. Telleria and A. Susperregui, "Methodology for Smooth Connection of Doubly Fed Induction Generators to the Grid," IEEE Transactions on Energy Conversion, vol. 24, pp. 959-971, 2009.

[82] R. Pena, J. C. Clare and G. M. Asher, "Doubly fed induction generator using back-to-back PWM converters and its application to variable-speed wind-energy generation," IEE Proceedings Electric Power Applications, vol. 143, pp. 231-241, 1996.

[83] S. A. Shaheen, H. M. Hasanien and M. A. Badr, "Study on Doubly Fed Induction Generator Control," in the 14th International Middle East Power Systems Conference (MEPCON'10), Cairo, Egypt, 2010, pp. 627-633.

[84] P. Vas, Sensorless Vector and Direct Torque Control: Oxford University Press, 1998.

[85] R. Cardenas and R. Pena, "Sensorless vector control of induction machines for variable-speed wind energy applications," IEEE Transactions on Energy Conversion, vol. 19, pp. 196-205, 2004.

[86] A. D. Hansen, P. Sørensen, F. Iov and F. Blaabjerg, "Centralised power control of wind farm with doubly fed induction generators," Renewable Energy, vol. 31, pp. 935-951, 2006.

[87] Q. Chen, M. Defourny and O. Brüls, "Control and simulation of doubly fed induction generator for variable speed wind turbine systems based on an integrated finite element approach," in Scientific Proceedings of European Wind Energy Conference & Exhibition (EWEA), Brussels, Belgium, 2011, pp. 12-16.

[88] A. D. Hansen, P. Sørensen, F. Iov and F. Blaabjerg, "Control of variable speed wind turbines with doubly-fed induction generators," Wind Engineering, vol. 28, pp. 411-432, June 2004.

[89] L. Holdsworth, X. G. Wu, J. B. Ekanayake and N. Jenkins, "Comparison of fixed speed and doubly-fed induction wind turbines during power system disturbances," IEE Proceedings Generation, Transmission and Distribution, vol. 150, pp. 343-352, 2003.

[90] U. Radel, D. Navarro, G. Berger and S. Berg, "Sensorless field oriented control of a slip ring induction generator for a 2.5 MW wind power plant from Nordex Energy GmbH," in European Power Electronics Conference, Graz, Austria, 2001.

[91] H. Hofmann, S. R. Sanders and C. R. Sullivan, "Stator-Flux-Based Vector Control of Induction Machines in Magnetic Saturation," IEEE Transactions on Industry Applications, vol. 33, pp. 935-942, 1997.

[92] M. R. Esmaeeli, R. Kianinezhad and M. Razzaz, "Field Oriented Control of DFIG in Wind Energy Conversion Systems," Journal of Basic and Applied Scientific Research, vol. 2, pp. 11486-11493, 2012.

[93] A. Petersson, "Analysis, modeling and control of doubly fed induction generators for wind turbines," PhD Thesis, Department of Energy and Environment, Chalmers University of Technology, Gothenburg, Sweden, 2005.

[94] M. Arifujjaman, M. T. Iqbal and J. E. Quaicoe, "Vector Control of a DFIG Based Wind Turbine," Istanbul University-Journal of Electrical and Electronics Engineering, vol. 9, pp. 1057-1066, 2009.

[95] J. Pierik, J. Morren, E. Wiggelinkhuizen, S. de Haan, T. van Engelen and J. Bozelie, "Electrical and Control Aspects of Offshore Wind Farms II (Erao II) volume 1: dynamic models of wind farms," ECN, Petten, Netherlands, Technical Report, 2004.

[96] P. D. Ziogas, E. P. Wiechmann and V. R. Stefanovic, "A Computer-Aided Analysis and Design Approach for Static Voltage Source Inverters," IEEE Transactions on Industry Applications, vol. IA-21, pp. 1234-1241, 1985.

[97] A. Bellini, F. Filippetti, C. Tassoni and G. A. Capolino, "Advances in diagnostic techniques for induction machines," IEEE Transactions on Industrial Electronics, vol. 55, pp. 4109-4126, 2008.

[98] A. Yazidi, G. A. Capolino, F. Filippetti and D. Casadei, "A New Monitoring System for Wind Turbines with Doubly-Fed Induction Generators," in IEEE Mediterranean Electrotechnical Conference (MELECON), Benalmádena (Málaga), Spain, 2006, pp. 1142-1145.

[99] H. Rodriguez-CortBs, C. N. Hadjicostis and A. M. Stankovic, "Model-Based Broken Rotor Bar Detection on an lFOC Driven Squirrel Cage Induction Motor," in the 2004 American Control Conference Boston, Massachusetls, 2004, pp. 3094-3099.

[100] T. Vaimann and A. Kallaste, "Detection of broken rotor bars in three-phase squirrel-cage induction motor using fast Fourier transform," presented at the 10th International Symposium on Topical Problems in the Field of Electrical and Power Engineering, Pärnu, Estonia, 2011.

[101] S. Nandi, H. A. Toliyat and X. Li, "Condition Monitoring and Fault Diagnosis of Electrical Motors-A Review," IEEE Transactions on Energy Conversion, vol. 20, pp. 719-729, 2005.

[102] A. Lebaroud, A. Bentounsi and G. Clerc, "Detailed study of the rotor asymmetry effects of induction machine under different supply conditions," in European Conference on Power Electronics and Applications, Dresden, 2005, pp. 1-8.

[103] F. Filippetti, G. Franceschini, C. Tassoni and P. Vas, "AI Techniques in Induction Machines Diagnosis Including the Speed Ripple Effect," IEEE Transactions on Industry Applications, vol. 34, pp. 98-108, 1998.

[104] P. Tavner, School of Engineering and Computing Sciences, University of Durham, United Kingdom, Personal Communication, 2013.

[105] D. Zappalà, P. Tavner, C. J. Crabtree and S. Sheng, "Sideband Algorithm for Automatic Wind Turbine Gearbox Fault Detection and Diagnosis," in European Wind Energy Association (EWEA) Conference, Vienna, Austria, 2013.

Appendices

A. Test Rig Parameter Measurement & Calculation

This section presents information on the electrical and mechanical measurements and calculation of the Test Rig component parameters, particularly in the DC motor and the generator.

A.1 DC Motor Stiction Torque, Friction & Windage Loss Coefficients

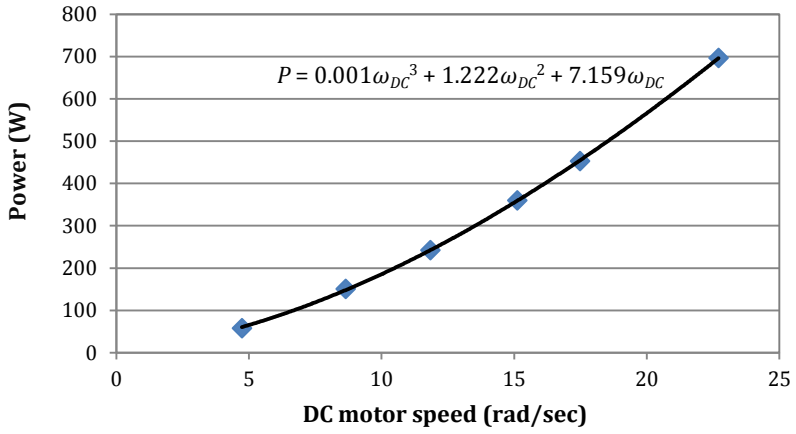

Fig. A.1: Mechanical power vs. DC motor speed

Table A.1: Stiction torque, friction & windage loss coefficients at DC motor-side

Stiction torque (Nm)	Friction loss coefficient (Nm.sec/rad)	Windage loss coefficient (Nm.sec²/rad²)
7.159	1.222	0.001

A.2 Generator Stiction Torque, Friction & Windage Loss Coefficients

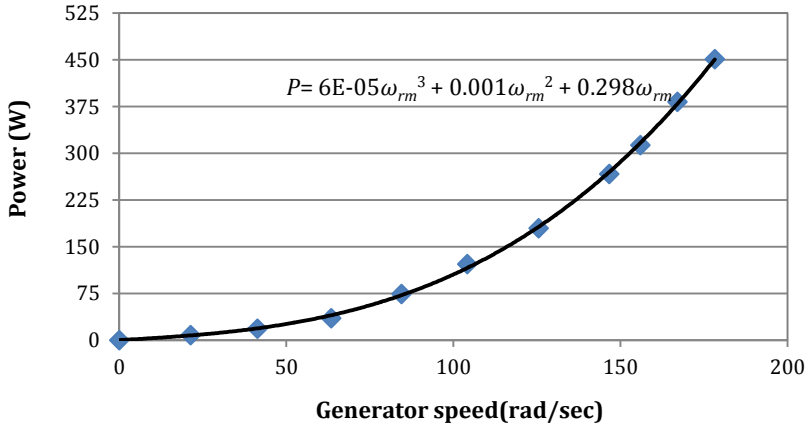

Fig. A.2: Mechanical power vs. Generator speed

Table A.2: Stiction torque, friction & windage loss coefficients at generator-side

Stiction torque (Nm)	Friction loss coefficient (Nm.sec/rad)	Windage loss coefficient (Nm.sec²/rad²)
0.298	0.001	6E-5

A.3 DC Motor Constant Calculation

$$T_{DC} = K_{\emptyset} i_f i_a \quad \text{A.1}$$

From the technical data for DC motor, the output power is 54kW at speed 2120rev/min (221.9rad/sec), armature current 131amps and field current 3.22 Amps.

$$T_{DC} = \frac{P}{\omega_{DC}} = \frac{54000}{221.9} = 243.35\text{Nm} \quad \text{A.2}$$

$$K_{\emptyset} = \frac{T_{DC}}{i_f i_a} = \frac{243.35}{3.22\times131} = 0.577\text{Nm/amp}^2 \quad \text{A.3}$$

A.4 Generator Electrical Parameters

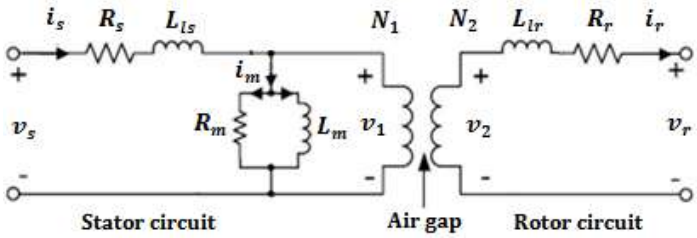

Fig. A.3: Equivalent circuit of DFIG

A.4.1 Stator-Rotor Turn Ratio Test

$$n_{sr} = \frac{v_1}{v_2} = \frac{N_1}{N_2} \approx \frac{v_s}{v_r} \quad \text{A.4}$$

Table A.3: Measured & calculated values during turn ratio test

Method 1			Method 2		
v_s (volt)	v_r (volt)	n_{sr1}	v_r (volt	v_s (volt)	n_{sr2}
51.08	38.90	1.313	38.60	47.26	1.224
70.60	54.00	1.307	43.60	54.17	1.242
80.74	60.71	1.329	50.80	62.64	1.233
100.00	76.34	1.309	75.00	92.00	1.226
$n_{sr1(average)} = 1.314$			$n_{sr2(average)} = 1.231$		
$n_{sr} = \frac{n_{sr1(average)} + n_{sr2(average)}}{2} = \frac{1.314 + 1.231}{2} = 1.272$					

A.4.2 No-Load Test

$$s(\%) = \frac{Synchronous\ speed - Speed}{Synchronous\ speed} \times 100 \quad \text{A.5}$$

$$Z_m = \frac{v_s}{i_s} \quad \text{A.6}$$

$$PF = cos\emptyset = \frac{P_{ph}}{v_s v_s} \quad \text{A.7}$$

$$R_m = \frac{Z_m}{cos\emptyset} \quad \text{A.8}$$

$$X_m = \frac{Z_m}{sin\emptyset} \quad \text{A.9}$$

$$L_m = \frac{X_m}{2\pi f} \quad \text{A.10}$$

Table A.4: Measured & calculated values during no-load test

Speed (rev/min)	s (%)	v_s (volt)	i_s (amp)	P_{ph} (W)	PF	Øº	Z_m (Ω)	R_m (Ω)	L_m (mH)
1498	0.133	232.6	24.8	410	0.071	85.9	9.38	131.9	29.93
1498	0.133	228.1	23.4	389	0.073	85.8	9.75	133.7	31.11
1498	0.133	225.2	22.5	376	0.074	85.7	10.01	134.9	31.97
1497	0.200	222.4	21.8	366	0.075	85.7	10.20	135.1	32.57
1496	0.267	219.7	21.0	356	0.077	85.6	10.46	135.6	33.40
1493	0.467	216.3	20.3	346	0.079	85.5	10.65	135.2	34.04
1490	0.667	213.9	19.7	337	0.080	85.4	10.86	135.7	34.68
1492	0.533	210.7	19.0	329	0.082	85.3	11.09	134.9	35.44
1487	0.867	207.9	18.5	323	0.084	85.2	11.24	133.8	35.92
1487	0.867	204.8	17.9	314	0.086	85.2	11.44	133.6	36.59
1486	0.933	202.4	17.5	307	0.087	85.0	11.57	133.5	29.93
1485	1.000	199.5	16.9	300	0.089	84.9	11.80	132.6	31.11
1487	0.867	196.6	16.5	297	0.092	84.8	11.92	130.2	31.97
1489	0.733	190.2	15.6	283	0.095	84.5	12.19	127.8	32.57

A.4.3 Locked Rotor Test

$$Z = \frac{v_s}{i_s} \quad \text{A.11}$$

$$X = X_s + X'_r = X_s + n_{sr}^2 X_r = Zsin\emptyset \quad \text{A.12}$$

We assume $X_s = X_r$, so

$$X_s = X_r = \frac{Zsin\emptyset}{(1+n_{sr}^2)} \quad \text{A.13}$$

$$L_{ls} = L_{lr} = \frac{X_s}{2\pi f} = \frac{X_r}{2\pi f} \quad \text{A.14}$$

$$L'_{lr} = n_{sr}^2 L_{lr} \quad \text{A.15}$$

Table A.5: Measured & calculated values during locked rotor test

v_s (volt)	i_s (amp)	P_T (W)	P_{ph} (W)	PF	Øº	Z (Ω)	L_{ls} (mH)	L_{lr} (mH)	L'_{lr} (mH)
18.9	26.8	534	178	0.352	69.4	0.704	0.802	0.802	1.298

The stator and rotor resistance were measured immediately by using BS407 Precision Milli/Micro Ohmmeter. These values are $R_s = 79.3m\Omega$, $R_r = 44.9m\Omega$ and $R'_r = n_{sr}^2 R_r = 72.6m\Omega$.

B. Reference Frame Transformations

In this section the theory of the reference frame transformations, used in the RSI controller, are introduced. This includes Clarke and Park transformation and their inverse transformations.

B.1 Clarke & Inverse Clarke Transformations

It is also known as $\alpha\beta$-transformation and it is a space vector transformation from a 3-phase stationary system (abc) into a stationary 2-phase reference frame ($\alpha\beta$). For an example of transformation, a time varying signals in abc-reference system as shown in Fig. B.1. The signal distribution of x_a, x_b and x_c are 120^o apart from each other. Cartesian axes are also portrayed, where x_α is the real axis aligned with phase x_a, and the imaginary axis rotated by 90^o is indicated by x_β.

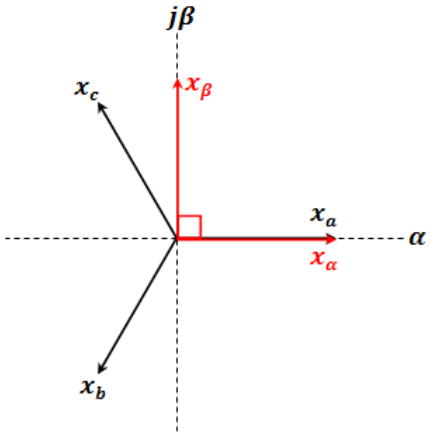

Fig. B.1: Space vector concept in $\alpha\beta$-reference frame

In general, the 3-phase signals in the axes a, b, and c, can be algebraically transformed into a stationary $\alpha\beta$-reference as following:

$$\begin{bmatrix} x_\alpha \\ x_\beta \end{bmatrix} = T_{\alpha\beta} \begin{bmatrix} x_a \\ x_b \\ x_c \end{bmatrix} \qquad \text{B.1}$$

where $T_{\alpha\beta}$ is often called the Clarke direct transformation and defined by:

$$T_{\alpha\beta} = \frac{2}{3}\begin{bmatrix} 1 & -\frac{1}{2} & -\frac{1}{2} \\ 0 & \frac{\sqrt{3}}{2} & -\frac{\sqrt{3}}{2} \end{bmatrix} \quad \text{B.2}$$

In addition, The Inverse Clarke transformation can also be obtained to transform the quantities back from stationary $\alpha\beta$ reference to 3-phase quantities by:

$$\begin{bmatrix} x_a \\ x_b \\ x_c \end{bmatrix} = T_{\alpha\beta}^{-1} \begin{bmatrix} x_\alpha \\ x_\beta \end{bmatrix} \quad \text{B.3}$$

and

$$T_{\alpha\beta}^{-1} = \begin{bmatrix} 1 & 0 \\ -\frac{1}{2} & \frac{\sqrt{3}}{2} \\ -\frac{1}{2} & -\frac{\sqrt{3}}{2} \end{bmatrix} \quad \text{B.4}$$

B.2 Park & Inverse Park Transformations

It is also known as dq-transformation and it is applying an angle transformation to convert from a stationary $\alpha\beta$-reference frame to a synchronously dq-rotating frame. The dq-reference frame is rotating at synchronous speed ω with respect to the $\alpha\beta$-reference frame, and at any instant, the position of d-axis with respect to α-axis is given by $\theta = \omega t$. The reference frames and transformations are shown in Fig. B.2.

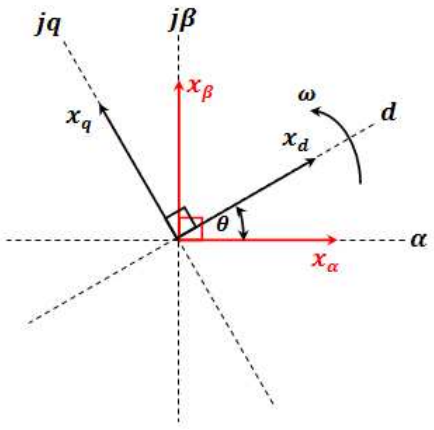

Fig. B.2: Space vector concept in dq-reference frame

The Park transformation is given by:

$$\begin{bmatrix} x_d \\ x_q \end{bmatrix} = \begin{bmatrix} cos\theta & sin\theta \\ -sin\theta & cos\theta \end{bmatrix} \begin{bmatrix} x_\alpha \\ x_\beta \end{bmatrix} \quad \text{B.5}$$

However, The Inverse Park transformation can be obtained by:

$$\begin{bmatrix} x_\alpha \\ x_\beta \end{bmatrix} = \begin{bmatrix} cos\theta & -sin\theta \\ sin\theta & cos\theta \end{bmatrix} \begin{bmatrix} x_d \\ x_q \end{bmatrix} \quad \text{B.6}$$

The synchronous reference frame can be aligned to rotate with the voltage (e.g. used in voltage source converters) or with the current (e.g. used in current source converters).

C. Extended Results

This appendix contains a complete set of figures of time domain simulated and measured data used for the frequency analysis in section 6.2. It also contains a more complete set of results figures for rotor fault detection under variable speed operation conditions above and below synchronous speed.

C.1 Time Domain Data at Fixed Speed ≃1598rev/min

C.1.1 Simulation Data

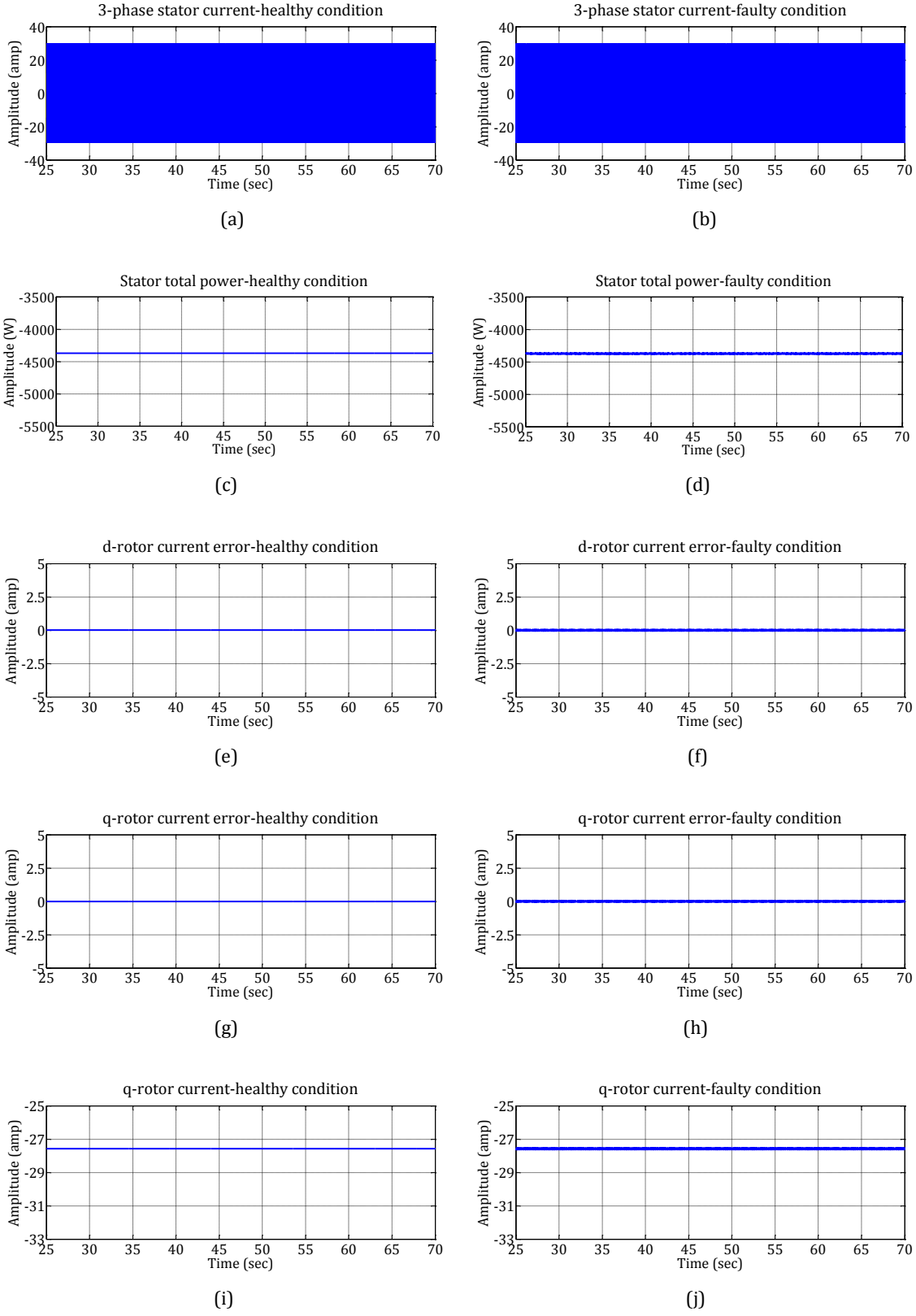

Fig. C.1: DFIG & RSI control signals simulated at fixed speed ≃1598rev/min

C.1.2 Measured Data

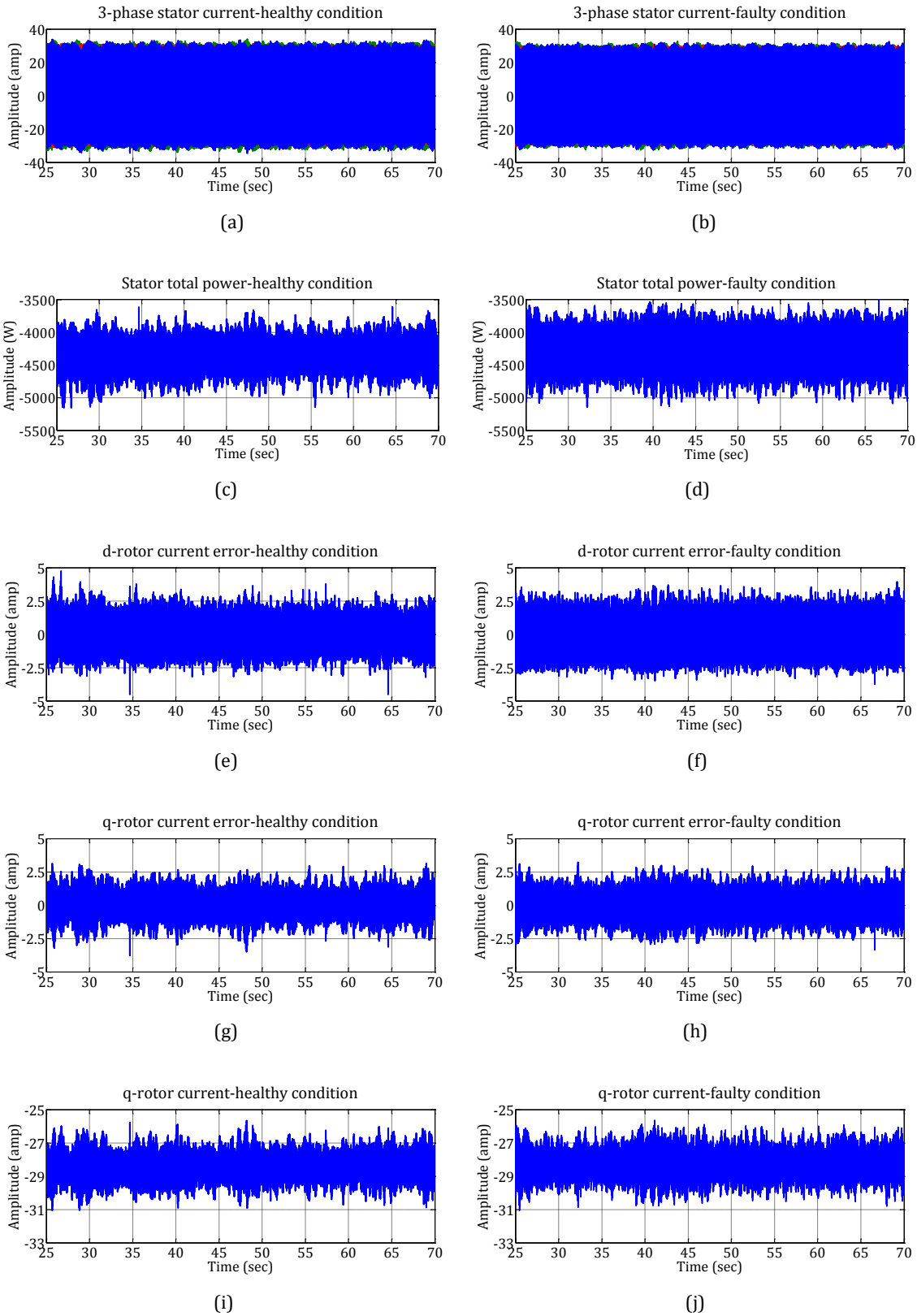

Fig. C.2: DFIG & RSI control signals measured at fixed speed ≃1598rev/min

C.2 Rotor Fault Detection under Variable Speed Operation

Further simulation and experimental results for fault detection of 20% rotor unbalance under variable speed operation conditions using the RSI control and DFIG signals are presented in this section.

C.2.1 Above Synchronous Speed

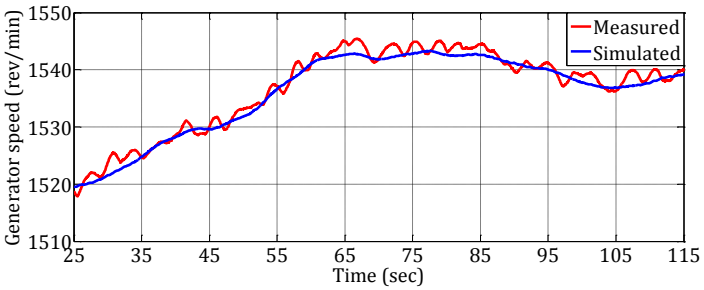

Fig. C.3: Generator rotational speed signal during simulated & measured variable speed tests above synchronous speed

All the spectra presented were calculated from data collected from 48sec to 58sec in both simulated and measured cases.

C.2.1.1 Simulation Results

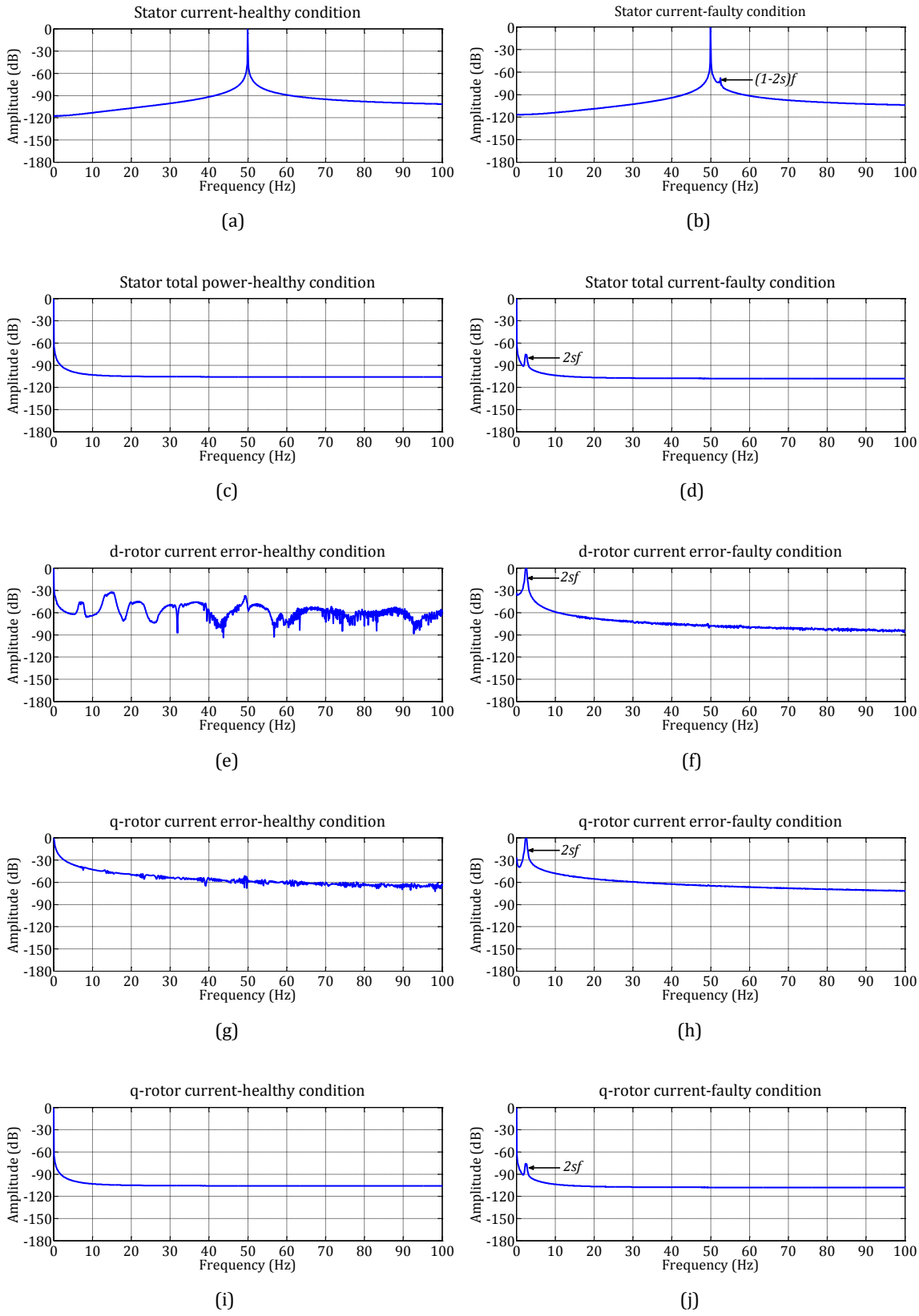

Fig. C.4: DFIG & RSI control signal spectra simulated at variable speed above synchronous speed

C.2.1.2 Measured Results

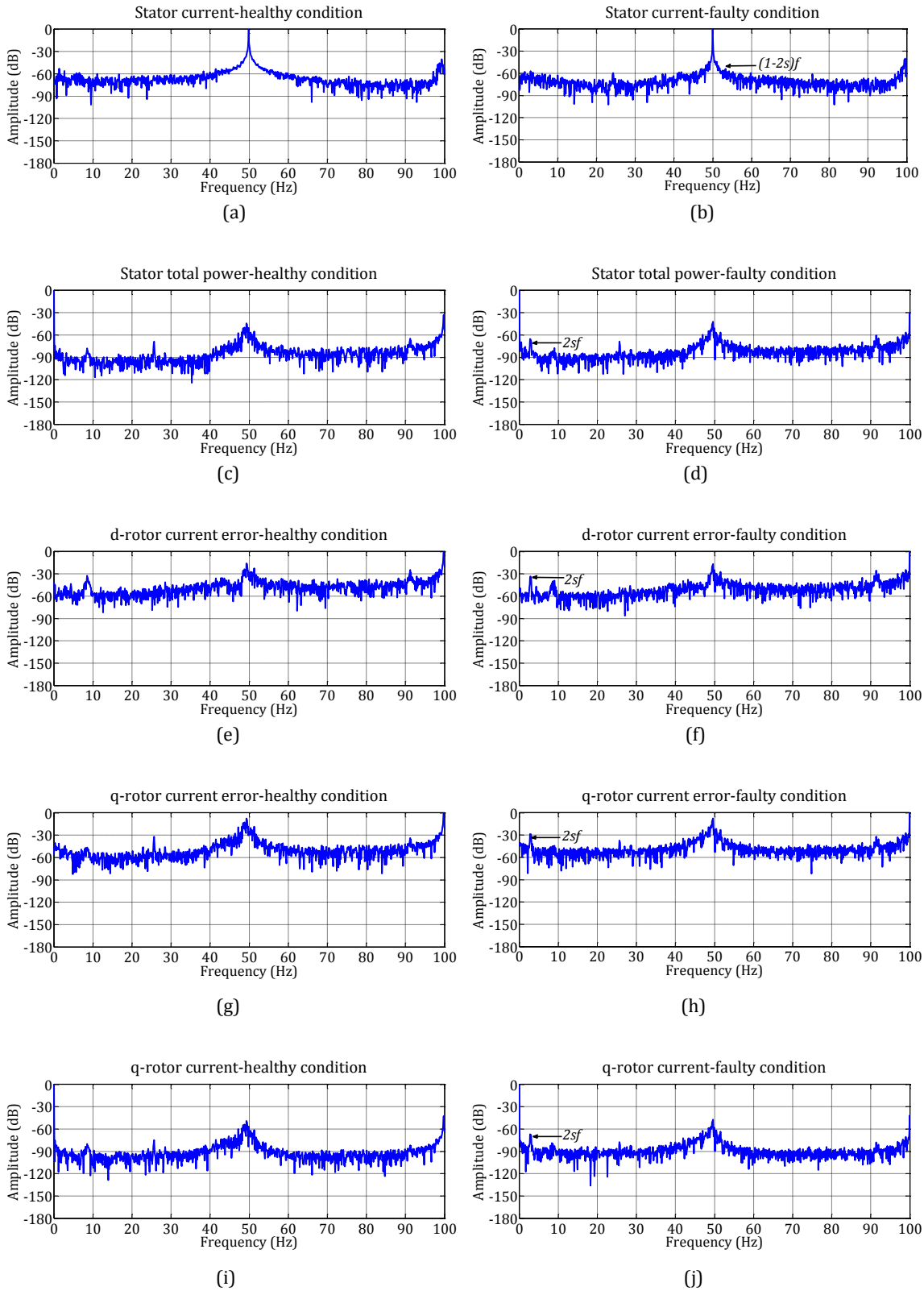

Fig. C.5: DFIG & RSI control signal spectra measured at variable speed above synchronous speed

C.2.2 Below Synchronous Speed

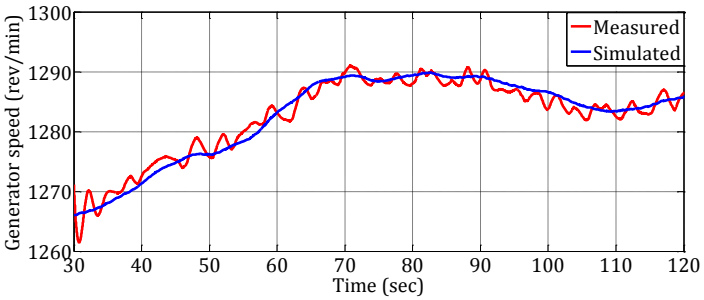

Fig. C.6: Generator rotational speed signal during simulated & measured variable speed tests below synchronous speed

All the spectra presented were calculated from data collected from 50sec to 60sec with sampling rate 5kHz in both simulated and measured cases.

C.2.2.1 Simulation Results

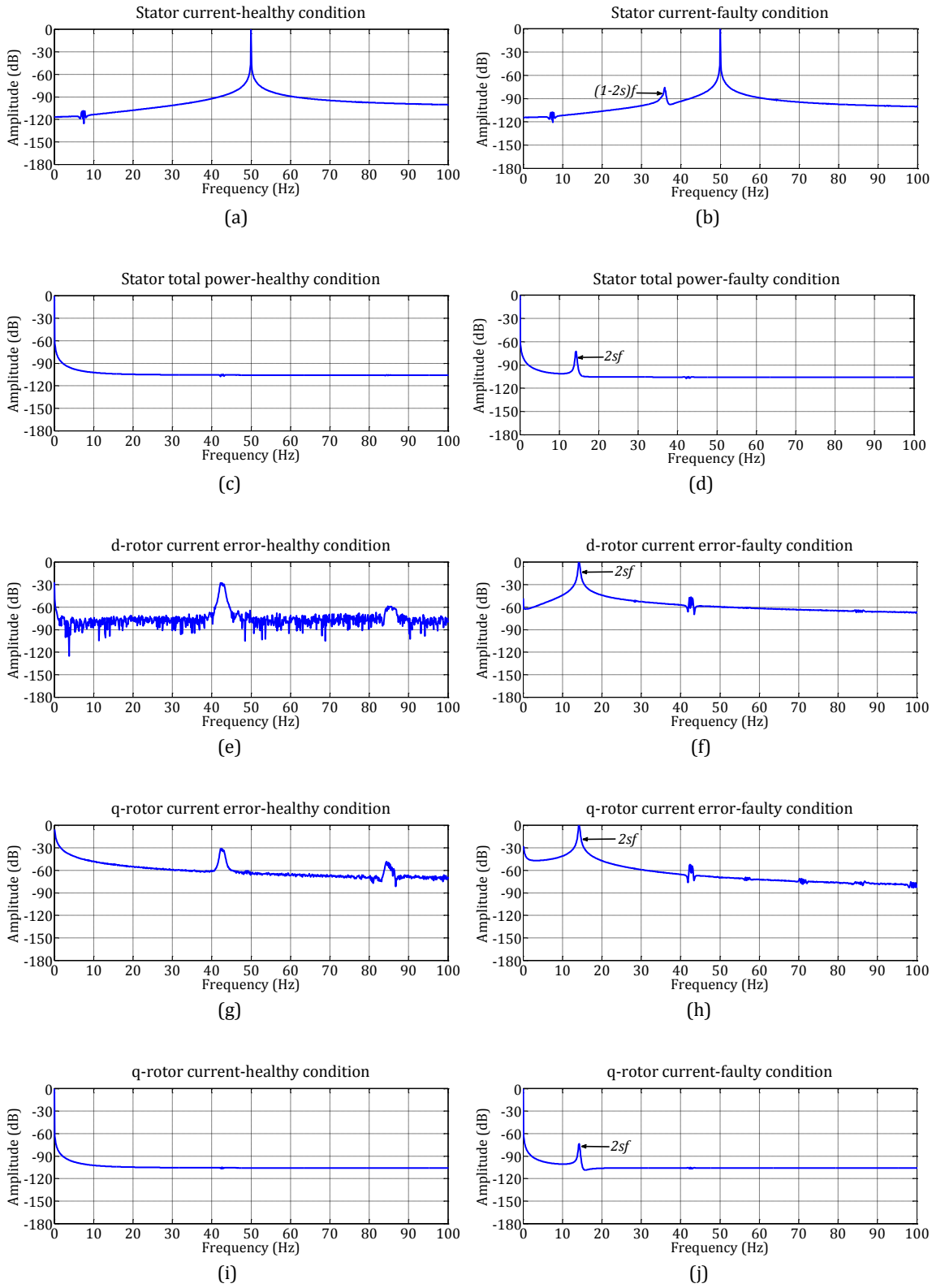

Fig. C.7: DFIG & RSI signal spectra simulated at variable speed below synchronous speed

C.2.2.1 Measured Results

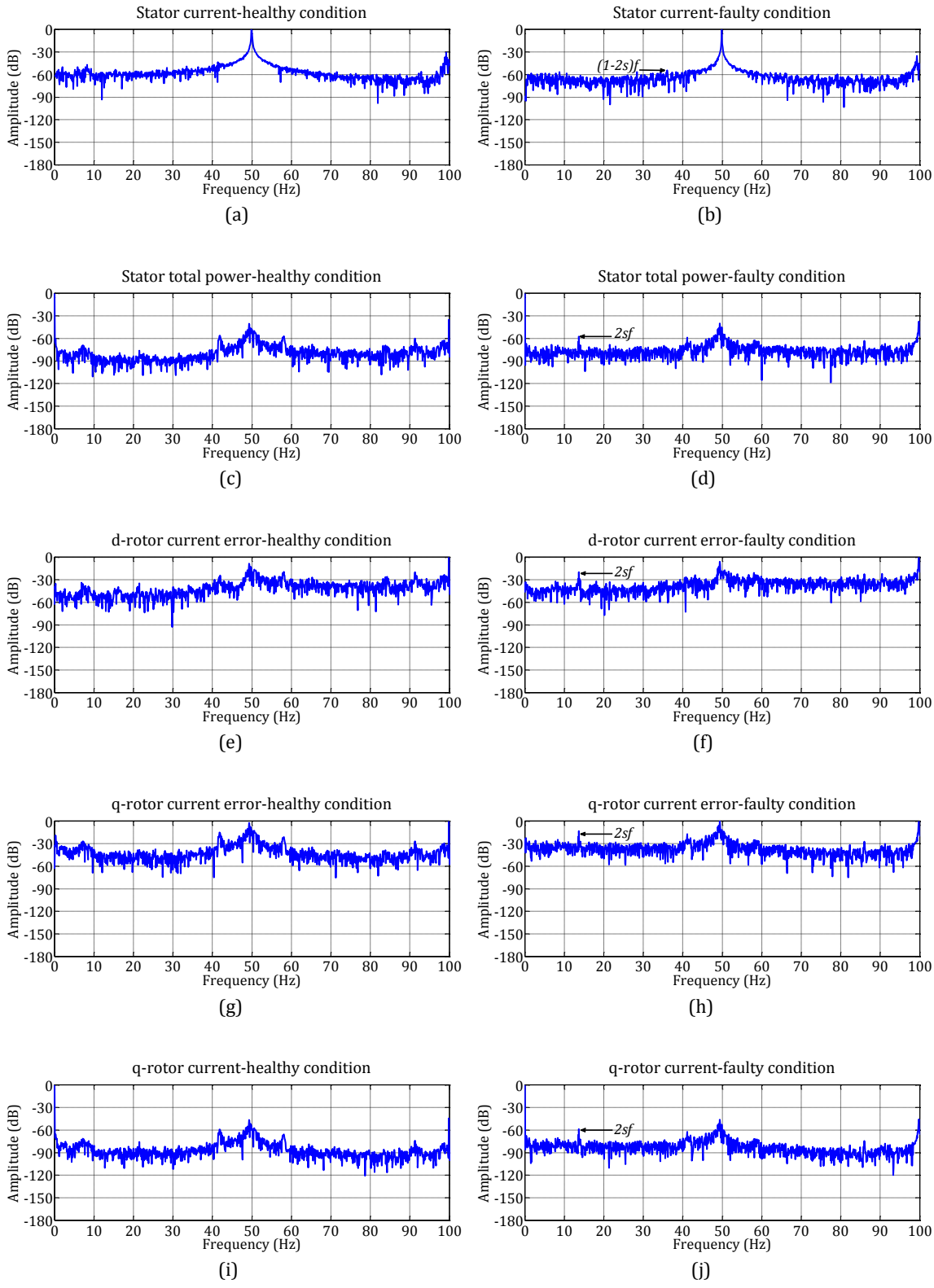

Fig. C.8: DFIG & RSI control signal spectra measured at variable speed below synchronous speed

D. Enlarged Figures from Chapter 6

This appendix contains enlarges version of the measured sensitivity result figures from Chapter 6 of this thesis.

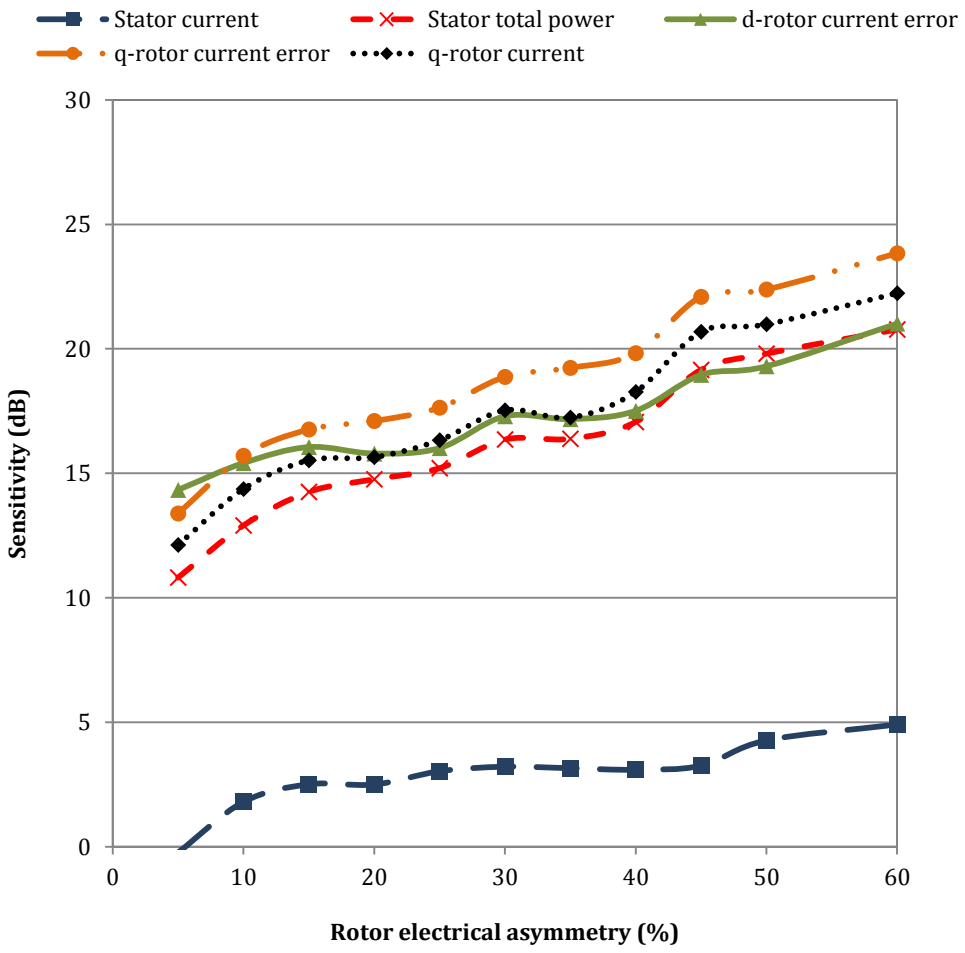

Fig. D.1: Enlarged Fig. 6.11b

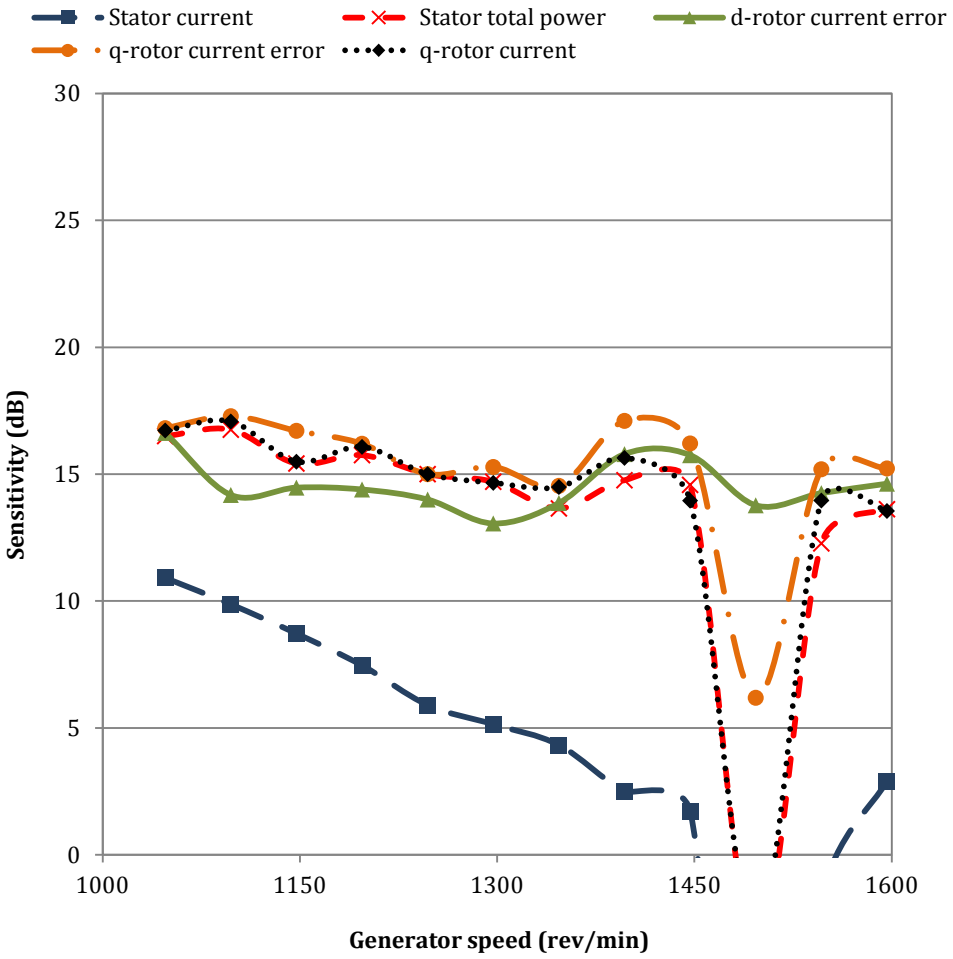

Fig. D.2: Enlarged Fig. 6.12b

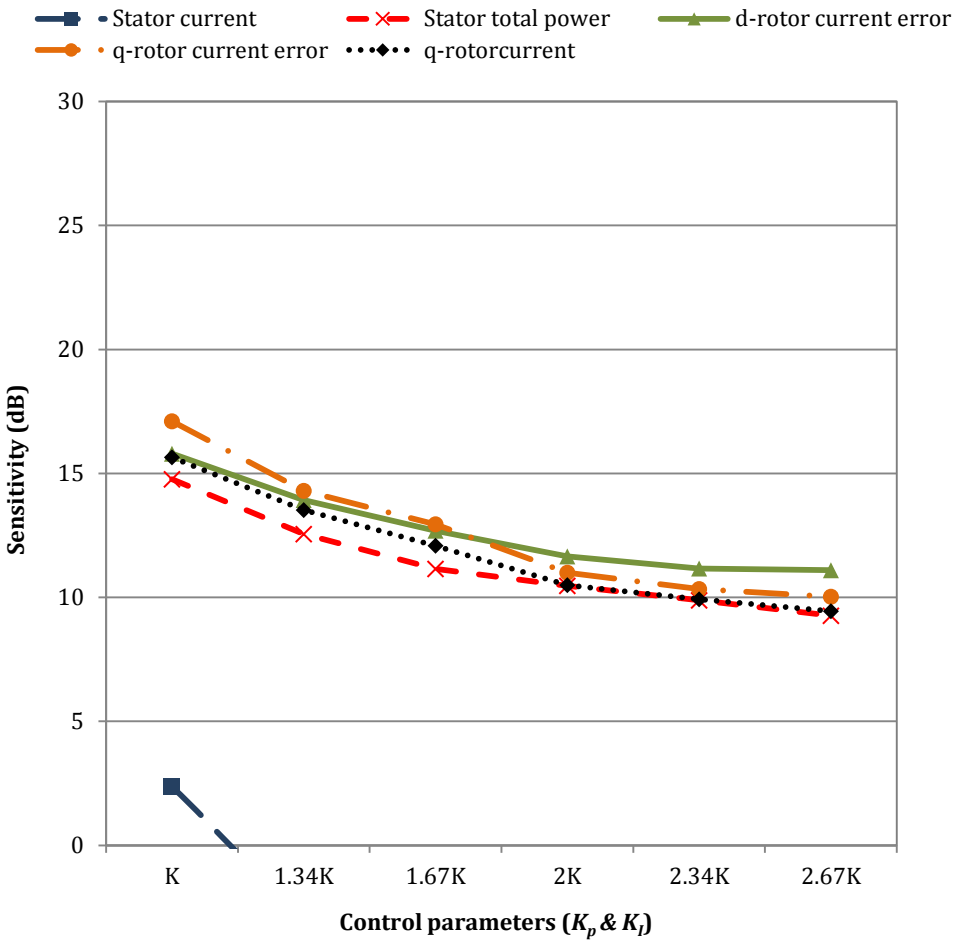

Fig. D.3: Enlarged Fig. 6.13b